Lehrstuhl für Computation in Engineering
Fakultät für Bauingenieur- und Vermessungswesen
Technische Universität München

Investigation of mechanical contact problems with high-order Finite Element Methods

David Christian Franke

Vollständiger Abdruck der von der Fakultät für Bauingenieur- und Vermessungswesen der Technischen Universität München zur Erlangung des akademischen Grades eines

Doktor-Ingenieurs

genehmigten Dissertation.

Vorsitzender:		Univ.-Prof. Dr.-Ing. K.-U. Bletzinger
Prüfer der Dissertation:		
	1.	Univ.-Prof. Dr.rer.nat. E. Rank
	2.	Univ.-Prof. Dr.-Ing. K. Schweizerhof Karlsruher Institut für Technologie (KIT)

Die Dissertation wurde am 22.06.2011 bei der Technischen Universität München eingereicht und durch die Fakultät für Bauingenieur- und Vermessungswesen am 02.12.2011 angenommen.

Abstract

The current study deals with the emerging field of mechanical contact problems. The behavior of two dimensional uni- and bilateral, frictionless and frictional contact problems is studied by using the *h*-, *p*-, *hp*-, and the *rp*-version of the Finite Element Method. The contact constraints are introduced by the penalty method. The main focus of the work is drawn to the level of accuracy which is to be derived with the different versions of the FEM. The accuracy is measured for the unilateral Hertzian contact problem in terms of the contact stress distribution in the contact interface and its neighborhood. Additionally, the convergence of the error in strain energy norm is studied as well. Both studies prove the capability of the *p*-version of the Finite Element Method and its adaptive extensions. A high polynomial degree in combination with an exact representation of the curved geometry leads together with the *rp*-method to a very high accuracy in the contact stresses. This is achieved by relocation of a Finite Element node to the end of the contact interface where the boundary condition changes from contact to no-contact, avoiding oscillations in the high-order polynomial shape functions at this point. The convergence rate of the strain energy reveals that a singularity exists in the solution domain. This singularity is located at the end of the contact interface where the boundary condition changes from contact to no-contact. The singularity at this point is equivalent to a singularity at the end of a distributed load. Only for the case that the load value and its first derivative is zero at the end of the loading area, the singularity vanishes. As this is generally not the case for contact problems, these singularities lead to convergence rates of algebraic type for the *h*-, *p*-, and the *rp*-version of the FEM. The *hp*-version instead is able to isolate this singularity, allowing for exponential rates of convergence.

Zusammenfassung

Die vorliegende Arbeit befasst sich mit dem Thema des unilateralen und bilateralen, reibfreien und reibungsbehafteten Kontakts. Dabei werden die *h*-, *p*-, *hp*- und *rp*-Version der Finite Elemente Methode untersucht. Die Kontaktrandbedingungen werden mit Hilfe des Penalty Verfahrens in die Finite-Element-Formulierung integriert. Im Fokus der Arbeit steht der Grad der Genauigkeit, der mit den verschiedenen Verfahren erzielt werden kann. Die erzielbare Genauigkeit wird hierbei am Beispiel des unilaterale Hertz'sche Kontaktproblems anhand der Spannungen im Kontaktbereich und den angrenzenden Bereichen angegeben. Weitere Studien untersuchen die Konvergenz des Fehlers in der Dehnungs-Energienorm. Sie bestätigen das hohe Potential der *p*-Version der FEM und ihrer adaptiven Erweiterungen. Die Untersuchung der Kontaktspannungen bei Anwendung der *rp*-Methode zeigt eine hohe Genauigkeit der Lösung. Der hohe Polynomgrad der Ansatzfunktionen bei Verwendung der exakten kreisförmigen Geometrie führt zu sehr exakten Ergebnissen, wenn das Kontaktende mit einem Finite Element Knoten zusammenfällt. Dies kann mit Hilfe des *rp*-Verfahrens erreicht werden, wodurch Oszillationen in den Ansatzfunktionen des Elements in der Umgebung dieses Punktes verhindert werden. Die Untersuchung der Konvergenzraten der Dehnungsenergienorm zeigt das Vorhandensein einer Singularität im Lösungsgebiet an. Diese liegt am Ende des Kontaktbereichs, an dem ein Wechsel der Randbedingungen von *in Kontakt stehend*, zu *kontaktfrei* vorhanden ist. Die Singularität ist von der gleichen Ordnung wie die Singularität, die am Ende einer verteilten Kraftrandbedingung auftritt. Sie verschwindet nur für den Spezialfall, dass nicht

nur der Wert der Last, sondern auch ihre Ableitung am Ende des Lastbereichs verschwindet. Da dies für allgemeine Kontaktprobleme nicht der Fall ist, führen die entstehenden Singularitäten zu einer algebraischen Konvergenzordnung in der Energienorm bei Anwendung der h-, p- und rp-Version der FEM. Bei Verwendung der hp-Methode sind darüber hinaus exponentielle Konvergenzraten möglich, wenn auf die Singularität am Kontaktende entsprechend verfeinert wird.

Vorwort

Die Arbeit entstand während meiner Assistentenzeit am Lehrstuhl für Computation in Engineering der Fakultät für Bauingenieur- und Vermessungswesen der TU München in den Jahren 2005 bis 2011. Sie wurde als Projekt mit dem Titel "Kontaktprobleme mit Finiten Elementen hoher Ordnung" durch die Deutsche Forschungsgemeinschaft gefördert.

Mein größter Dank richtet sich an meinen Doktorvater Professor Dr.rer.nat. Ernst Rank. Seine anhaltende Unterstützung, zusammen mit den persönlichen Freiheiten am Lehrstuhl und der Portion sanften Nachdrucks, resultieren in der vorliegenden Arbeit.

Für die Übernahme des Koreferats und sein Interesse an meiner Arbeit bedanke ich mich bei Herrn Professor Dr.-Ing. K. Schweizerhof. Durch seine Nähe zur Praxis im Bereich der Kontaktmechanik empfinde ich seine Forschungsarbeit als sehr wertvoll für den praktischen Ingenieur.

Bei Herrn Professor Dr.-Ing. Alexander Düster bedanke ich mich für seine stete Unterstützung nicht nur während seiner Zeit in München, sondern auch später seit seiner Zeit als Professor in Hamburg. Sein anhaltendes Interesse und die vielen konstruktiven Diskussionen waren stets sehr hilfreich und beeinflussten die Richtung und Ausarbeitung der Arbeit in erheblichem Masse.

Des Weiteren bedanke ich mich bei all meinen Kollegen, die mich in den vergangenen Jahren am Lehrstuhl begleitet haben. Es waren schöne und lehrreiche Jahre, die ich nicht missen will.

Meinen Eltern und meinem Bruder danke ich in jeder Hinsicht für ihre andauernde Unterstützung und ihren Rückhalt.

Manchem Bekannten, fachfremd oder nicht, huschte in der Vergangenheit ein Lächeln durchs Gesicht, wenn er erfuhr, dass ich 'Kontaktprobleme' habe. Auch wenn ich dieses Missverständnis leicht aufklären konnte, ist es doch ein Indiz dafür, dass es auch in anderen Lebensbereichen zu Kontaktproblemen kommen kann. Leider helfen in diesem verwandten Themenfeld meist auch die besten Bücher nichts, weshalb davon abgesehen wurde den Fortsetzungsantrag in diesem Bereich weiterzuführen. Studien der menschlichen Kontaktprobleme sind jedem Individuum selbst überlassen. Auch diese Studien sind zum Teil mit Fleiß erarbeitet, oder von etwas Glück und günstigen Entscheidungen beeinflusst. Die Parallelitäten sind also durchaus erkennbar.

Ich wünsche dem Leser viele neue Erkenntnisse beim Studieren der mechanischen Kontaktprobleme in der vorliegenden Arbeit, ermahne aber daran, die wahren Kontaktprobleme des Lebens nicht aus den Augen zu verlieren.

Contents

Chapter 1

Introduction

Contact mechanics has been a research field in engineering and science since more than 100 years. The variety of studied examples over this period reaches from analytical solutions of problems of simple geometry to complex three dimensional dynamic contact analyses with finite strains. Nowadays, complex and highly nonlinear problems are essentially analysed by numerical schemes such as the Finite Element Method.

1.1 Motivation

A detailed study of contact phenomena is important in various fields of engineering and beyond. Numerous examples in mechanical engineering arise in the automotive industry in fields as car crash analysis or sheet metal forming. Further examples address the abrasive wear of engine parts or car tires. In civil engineering, contact mechanics plays an important role in the behavior of roller bearings as often used for bridges, seismic dampers like friction pendulums for buildings and bridges, and analysis of the mantle friction of drilled or driven piles in soil mechanics. Another emerging field is the area of medical engineering. Important problems are for examples related to hip or knee implants like the wear between the individual implant parts, or the bond between the implant and the bone. Dentistry is another field that calls for contact mechanics analysis to optimize the position and shape of dental prosthesis, implants and inlays.

So far research in contact analysis is mainly driven by low-order Finite Element techniques involving a large number of isoparametric linear elements to discretize the computation domain. The small size of the elements is beneficial in order to capture a large number of small fragmented contact areas. On the other hand the description of arbitrarily curved geometries is only approximated linearly thus introducing a significant modeling error. Linear ansatz functions for the displacements are restricted to a constant pressure inside the Finite Elements, which is insufficient for the representation of contact pressure of e.g. wearing problems. The use of polynomial shape functions of higher order improves the results in various applications. These so called high-order Finite Elements are beneficial for the computation of large homogeneous structures. The p-FEM meshes are usually coarse and the elements tend to be large performing well also for aspect ratios of up to 1:1000. They are therefore advantageous for thin structures with relatively large and continuous contact areas. The application of the p-FE method for contact analysis is thus intended to be applied to for example metal sheet forming processes, where a thin metal sheet is coming in contact with the die, punching the desired shape into the metal sheet.

1.2 Objectives

The objectives of the current work addresses the performance of high-order Finite Elements applied to two dimensional, unilateral and bilateral, frictionless and frictional mechanical contact problems. The performance is evaluated in terms of the accuracy in the contact stresses and in the convergence of the error in energy norm. The quality of four different Finite Element Methods will be studied:

h-version of the Finite Element Method

p-version of the Finite Element Method

hp-version of the Finite Element Method

rp-version of the Finite Element Method.

In order to exploit the advantages of the *p*-version of the Finite Element Method, special attention will be drawn on handling the reduced regularity at the end of the contact interface. Therefore the two adaptive *hp*- and the *rp*-methods will be employed and studied in detail.

1.3 Structure

In the following, the structure of this work will be given for each chapter.

Chapter 2 provides a summary of the general concept of the high-order Finite Element Method. Starting with the kinematics, the balance principles, and the material law, the weak form of equilibrium will be derived in compact form. This is followed by an introduction into the mapping concept, the hierarchical shape function basis, and the blending function method.

Chapter 3 recalls the principles of contact mechanics. First the kinematics, for normal and tangential contact is given, before the weak form of contact is derived. The discretization of the additional contact constraints with the penalty method is presented, and the discretization of the contact interface is given. The linearization by a numerical Newton algorithm follows at the end of this chapter.

Chapter 4 deals with the extensions of the Finite Element Method implemented to handle the reduced regularity at the end of the contact interface. It describes the difficulties at these points by studying their stress intensity factor and discussing the analogy of contact problems and a Neumann boundary condition. Conclusions are drawn and the two adaptive *hp*- and *rp*-methods are introduced.

Chapter 5 shows the numerical models and results obtained for various examples. The examples cover the unilateral and bilateral frictionless Hertzian contact problem in 2D, the contact between an elastic ring and a rigid foundation, contact between a stiff axle and a (Donut) ring, and the bilateral frictional example of two contacting bars.

Chapter 6 is a summary of the presented project, drawing conclusions, and providing an outlook for future work.

Chapter 2

Finite Element Method

The Finite Element Method (FEM) is a well-known and well-understood numerical solution scheme for problems from engineering and the natural sciences [19]. The physical problem which idealizes the real problem can be described with a mathematical model, leading to a system of partial differential equations. The Finite Element Method is then a technique to solve the system of partial differential equations numerically. The general procedure is to decompose the given spacial domain into a finite number of elements, where the ansatz or shape functions and hence the unknowns live. The resulting, global system of equations which is composed (assembled) from all the individual elements is then solved for the unknowns. The accuracy of the Finite Element Method is limited by three error sources, the *model error*, the *discretization error*, and the *roundoff error*. All three errors have to be controlled in order to achieve reliable results [57].

The discretization error which depends on the level of discretization of the physical domain, can be controlled by global mesh refinement for the case when the h-version of the FEM is used. When the p-version of the FEM is used instead, the mesh is kept fixed and the shape functions' polynomial degree is raised in order to reduce the discretization error. Nevertheless a successive refinement of the discretization (by h- or p-refinement) may have a dramatic influence on the numerical effort of the solution procedure [57].

The model error originates from assumptions which are introduced to simplify the given physical properties. These can be assumptions like a simplified constitutive model, negligence of time dependent effects, or the use of dimensionally reduced models like for beams, plates, and shells. The roundoff error is nowadays negligible, if a stable algorithm in combination with the up to date computer precision is used.

The main challenge in the Finite Element development is to formulate methods for physical problems in such a way, that they represent the physical properties well and additionally show numerically good convergence characteristics.

2.1 Linear Elasticity

The behavior of solid objects with a given material distribution and no yielding is generally described by the linear theory of elasticity, assuming small deformations and small strains. When larger displacements are to be considered, hyperelastic material properties have to be used. Literature can be found for example in [10, 87].

The basic governing equations are derived by the principles of elastostatics. These are the *kinematic*, *equilibrium*, *constitutive model*, and *boundary conditions* which will be formulated on the infinitesimal volume with homogeneous material properties and small displacement gradients in the following sections.

2.1.1 Kinematics

The state of motion and the state of deformation of a body Ω at any time t is covered by kinematics. One differs between the *Eulerian* and the *Lagrangian* formulation. The *Eulerian* formulation (also called *spacial* formulation) traces changes happening at a specific point in space over time and is often applied in fluid mechanics. The *Lagrangian* formulation (also called *material* formulation) instead focuses on the individual particle and its individual motion [10]. It is mostly used in solid mechanics and will therefore be used here.
As shown in Figure 2.1 a particle in a body Ω can be uniquely defined by its position vector $\mathbf{X} \in \Omega_{\mathrm{ref}}$, with Ω_{ref} being the bodies' reference configuration. A reference position $\mathbf{X}$ in the three dimensional *Euclidean* space $\mathbb{E}^3$ is defined with respect to an orthonormal basis (Cartesian coordinate system) with origin O. The motion of a single particle P is sketched in Figure 2.1. At time t the location vector for the material point P has changed over time to a new position p that is specified in the bodies' current configuration Ω_{t}. The mapping ϕ_t then describes the motion of the particle between the reference position $\mathbf{X}$ and the new position $\mathbf{x}$

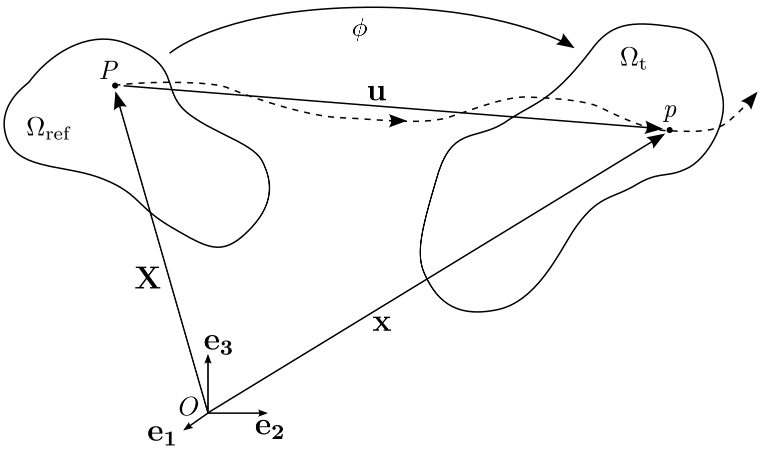

Figure 2.1: General motion of a deformable Body Ω.

$$\mathbf{x} = \phi_t(\mathbf{X}) \tag{2.1}$$

It should be noted, that the reference configuration does at no time has to be occupied by the body. It can be chosen arbitrarily. An example for this is the isoparametric concept within the Finite Element Method where an easy to handle reference configuration is chosen which is pure fictive [87]. The difference of the location vectors $\mathbf{X}$ in Ω_{ref} and $\mathbf{x}$ in Ω_{t} is expressed by the displacement vector $\mathbf{u}$.

$$\mathbf{u} = \mathbf{x} - \mathbf{X} \quad \textit{or} \tag{2.2}$$
$$\mathbf{x} = \mathbf{X} + \mathbf{u} \tag{2.3}$$

which is a combination of rigid body displacements, rotations, and deformations within the body.
Forces acting on a body entail deformations $\mathbf{u}$.

$$\mathbf{u} \;=\; [u_x,\ u_y,\ u_z]^T \tag{2.4}$$

The deformation process is described locally by the deformation gradient $\mathbf{F}$, mapping from the reference to the current configuration [87]. The tensor $\mathbf{F}$ enables to describe the relative spatial position of two neighboring particles after deformation, by their relative material position before deformation. This single material vector $d\mathbf{X}$ in Ω_{ref} is associated to the corresponding vector $d\mathbf{x}$ in Ω_t by the deformation gradient $\mathbf{F}$ as:

$$d\mathbf{x} = \mathbf{F}\ d\mathbf{X} \tag{2.5}$$

The deformation gradient itself can be split up into two terms [29]:

$$\mathbf{F} = \mathbf{I} + \mathbf{H} \tag{2.6}$$

where $\mathbf{I}$ is a unit matrix and $\mathbf{H}$ is the displacement gradient, containing the partial derivatives of the displacement coordinates in the reference configuration [59].

$$\mathbf{H} = \frac{\partial \mathbf{u}}{\partial \mathbf{X}} = \text{Grad}\ \mathbf{u} \tag{2.7}$$

Introducing the Green-Lagrange strain tensor $\mathbf{E}$ as the difference of the squared line element $d\mathbf{X}$ before and after deformation [29, 59]:

$$\begin{aligned} d\mathbf{x}\ d\mathbf{x} - d\mathbf{X}\ d\mathbf{X} &= \mathbf{F}d\mathbf{X}\ \mathbf{F}d\mathbf{X} - d\mathbf{X}\ d\mathbf{X} \\ &= d\mathbf{X}\ (\mathbf{F}^\mathbf{T}\mathbf{F})\ d\mathbf{X} - d\mathbf{X}\ d\mathbf{X} \\ &= d\mathbf{X}\ (\mathbf{F}^\mathbf{T}\mathbf{F} - \mathbf{I})\ d\mathbf{X} \\ &= d\mathbf{X}\ (\mathbf{H} + \mathbf{H}^\mathbf{T} + \mathbf{H}^\mathbf{T}\mathbf{H})\ d\mathbf{X} \end{aligned} \tag{2.8}$$

The strain tensor $\mathbf{E}$ is formed as:

$$\mathbf{E} \;=\; \frac{1}{2}(\mathbf{F}^\mathbf{T}\mathbf{F} - \mathbf{I}) \tag{2.9}$$

$$\;=\; \frac{1}{2}(\mathbf{H} + \mathbf{H}^\mathbf{T} + \mathbf{H}^\mathbf{T}\mathbf{H})\ . \tag{2.10}$$

The term $\mathbf{H}^\mathbf{T}\mathbf{H}$ shows the nonlinear character of the Green-Lagrange strain tensor [87]. When linear theory is used, this term is neglected by assuming small displacement gradients ($\|\mathbf{H}\| << 1$). This leads to the linear strain tensor $\boldsymbol{\varepsilon}$:

$$\boldsymbol{\varepsilon} = \frac{1}{2}(\mathbf{H} + \mathbf{H}^\mathbf{T})\ . \tag{2.11}$$

From a momentum equilibrium it can be seen that the shear strain $\gamma_{xy} = \gamma_{yx}$. The same applies to $\gamma_{xz} = \gamma_{zx}$ and $\gamma_{yz} = \gamma_{zy}$. Therefore the three dimensional symmetric strain tensor $\boldsymbol{\varepsilon}$ consists of only six independent strain components which are arranged in VOIGT notation as

$$\boldsymbol{\varepsilon} \;=\; [\varepsilon_{xx},\ \varepsilon_{yy},\ \varepsilon_{zz},\ \gamma_{xy},\ \gamma_{yz},\ \gamma_{xz}]^T\ . \tag{2.12}$$

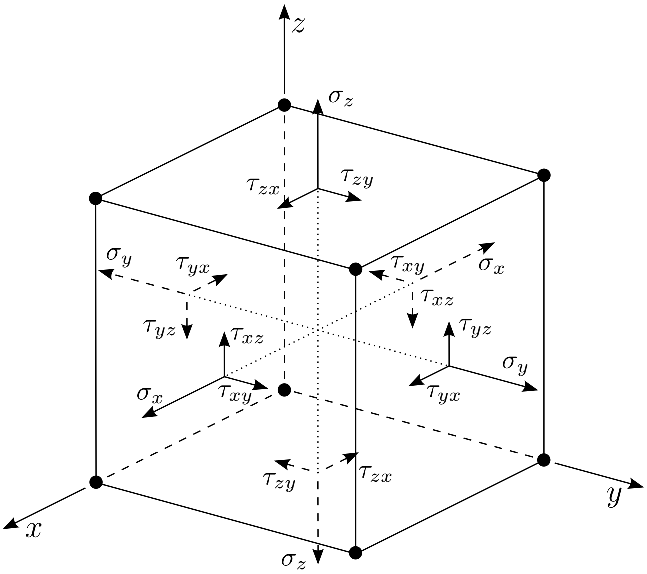

Figure 2.2: Sign convention of stresses on the differential element

Each of the independent strain components is then given by the following relation.

$$\begin{aligned} \varepsilon_{xx} &= \tfrac{\partial u_x}{\partial x}, & \varepsilon_{yy} &= \tfrac{\partial u_y}{\partial y}, & \varepsilon_{zz} &= \tfrac{\partial u_z}{\partial z} \\ \gamma_{xy} &= \tfrac{\partial u_x}{\partial y} + \tfrac{\partial u_y}{\partial x}, & \gamma_{yz} &= \tfrac{\partial u_y}{\partial z} + \tfrac{\partial u_z}{\partial y}, & \gamma_{xz} &= \tfrac{\partial u_x}{\partial z} + \tfrac{\partial u_z}{\partial x} \; . \end{aligned} \tag{2.13}$$

Introducing the matrix for the differential operator $\mathbf{D}$:

$$\mathbf{D} = \begin{bmatrix} \frac{\partial}{\partial x} & 0 & 0 \\ 0 & \frac{\partial}{\partial y} & 0 \\ 0 & 0 & \frac{\partial}{\partial z} \\ \frac{\partial}{\partial y} & \frac{\partial}{\partial x} & 0 \\ 0 & \frac{\partial}{\partial z} & \frac{\partial}{\partial y} \\ \frac{\partial}{\partial z} & 0 & \frac{\partial}{\partial x} \end{bmatrix} \tag{2.14}$$

the strains $\boldsymbol{\varepsilon}$ in matrix-vector notation is derived from the displacements $\mathbf{u}$ by:

$$\boldsymbol{\varepsilon} = \mathbf{D}\mathbf{u} \; . \tag{2.15}$$

2.1.2 Equilibrium

Every resting object is in a static equilibrium. In order to obtain solid and resting structures, a key objective is to find the equilibrated state of the system of interest. As Newton already described in his third Axiom: *actio = reactio*, forces acting on a body have to be in an equilibrated state. Thus, the internal forces have to be equal to the external forces in size and direction. On a differential element plotted in Figure 2.2 we can formulate the equilibrium conditions as differential equations of the form:

$$\begin{aligned}
&\frac{\partial \sigma_{xx}}{\partial x} + \frac{\partial \sigma_{xy}}{\partial y} + \frac{\partial \sigma_{xz}}{\partial z} + f_x = 0 \\
&\frac{\partial \sigma_{yx}}{\partial x} + \frac{\partial \sigma_{yy}}{\partial y} + \frac{\partial \sigma_{yz}}{\partial z} + f_y = 0 \\
&\frac{\partial \sigma_{zx}}{\partial x} + \frac{\partial \sigma_{zy}}{\partial y} + \frac{\partial \sigma_{zz}}{\partial z} + f_z = 0
\end{aligned} \tag{2.16}$$

where $\mathbf{f} = [f_x,\ f_y,\ f_z]^T$ represent the body force per unit volume. The stress tensor of second order takes the following form.

$$\boldsymbol{\sigma} \ = \ \begin{bmatrix} \sigma_{xx} & \sigma_{xy} & \sigma_{xz} \\ \sigma_{yx} & \sigma_{yy} & \sigma_{yz} \\ \sigma_{zx} & \sigma_{zy} & \sigma_{zz} \end{bmatrix} \tag{2.17}$$

As for the strain tensor, under our assumptions only six stress components are independent due to symmetry reasons. Using the VOIGT notation, $\boldsymbol{\sigma}$ therefore reduces to:

$$\boldsymbol{\sigma} = [\sigma_{xx},\ \sigma_{yy},\ \sigma_{zz},\ \sigma_{xy},\ \sigma_{yz},\ \sigma_{xz}]^T \tag{2.18}$$

Together with the differential operator $\mathbf{D}$ and $\boldsymbol{\sigma}$, Equation 2.16 reduces to:

$$\mathbf{D}^T\boldsymbol{\sigma} + \mathbf{f} = \mathbf{0} \tag{2.19}$$

2.1.3 Constitutive Model

Constitutive models are needed to describe the relation between stresses and strains, considering the material properties. For the general case of a linear elastic and isotropic material property, which is being focused on here, the stresses are directly related to the corresponding strains by the material matrix $\mathbf{C}$. The well known HOOKE's law therefore is:

$$\boldsymbol{\sigma} = \mathbf{C}\boldsymbol{\varepsilon}\ . \tag{2.20}$$

Herein the material matrix $\mathbf{C}$ is only depending on the YOUNG's modulus E and the POISSON ratio ν.

$$\mathbf{C} \ = \ \frac{E}{(1+\nu)(1-2\nu)} \begin{bmatrix} (1-\nu) & \nu & \nu & 0 & 0 & 0 \\ \nu & (1-\nu) & \nu & 0 & 0 & 0 \\ \nu & \nu & (1-\nu) & 0 & 0 & 0 \\ 0 & 0 & 0 & \frac{(1-2\nu)}{2} & 0 & 0 \\ 0 & 0 & 0 & 0 & \frac{(1-2\nu)}{2} & 0 \\ 0 & 0 & 0 & 0 & 0 & \frac{(1-2\nu)}{2} \end{bmatrix} \tag{2.21}$$

2.1.4 Boundary Conditions

NEUMANN boundary conditions Γ_T (prescribed stresses) and DIRICHLET (or geometric) boundary conditions Γ_D (prescribed displacements) have to be defined on the boundary $\partial\Omega$ of a body Ω. The boundary conditions are set by using the normal and tangential vector on the bounding edge or surface. The unit normal vector is defined positive, when pointing outwards. A load vector $\mathbf{t}$ on the boundary is therefore related to the stress tensor σ by the following equation:

$$\mathbf{t} = \boldsymbol{\sigma}\mathbf{n} \tag{2.22}$$

2.1.5 Principle of Virtual Work

The principle of virtual work is one of the major basics of structural mechanics. Starting from Equation 2.19 when seeking for the unknown displacement field **u** one introduces virtual deformations, called test functions **v**. Multiplication of the test functions with the differential Equation 2.19 and integrating over the relevant domain Ω leads to the following expression.

$$\int_{\Omega} \mathbf{D}^T \boldsymbol{\sigma} \mathbf{v} \; d\Omega + \int_{\Omega} \mathbf{f}\mathbf{v} \; d\Omega = \mathbf{0} \qquad \text{for all } \mathbf{v} \tag{2.23}$$

Herein, equilibrium is only fulfilled in an integral sense. Integration by parts and applying the Gauss theorem on Equation 2.23 leads together with the constitutive relations to the weak form of equilibrium where the internal work $\boldsymbol{\varepsilon}(\mathbf{v}) \; \boldsymbol{\sigma}(\mathbf{u})$ is related to body Ω and Γ_t represents the boundary of the domain.

$$\int_{\Omega} \boldsymbol{\varepsilon}(\mathbf{v}) \; \boldsymbol{\sigma}(\mathbf{u}) \; d\Omega - \int_{\Omega} \mathbf{f}\mathbf{v} \; d\Omega - \int_{\Gamma_t} \mathbf{t}\mathbf{v} \; d\Gamma_t = 0 \tag{2.24}$$

In matrix notation Equation 2.24 transforms to:

$$\int_{\Omega} (\mathbf{D}\mathbf{v})^T \;\; \mathbf{C} \;\; (\mathbf{D}\mathbf{u}) \;\; d\Omega = \int_{\Omega} \mathbf{f}\mathbf{v} \; d\Omega + \int_{\Gamma_t} \mathbf{t}\mathbf{v} \; d\Gamma_t \; . \tag{2.25}$$

In order to solve this equation, the objective is now to find the function $\mathbf{u}_{ex}$ with finite strain energy, satisfying the boundary conditions such that

$$\mathcal{B}(\mathbf{u_{ex}}, \mathbf{v}) = \mathcal{F}(\mathbf{v}) \tag{2.26}$$

holds for all functions **v**, with **v** being an arbitrary function with finite strain energy. The function $\mathbf{u_{ex}}$ is the weak solution of the elasticity problem and minimizes the potential energy $\mathbf{\Pi}$ with respect to the admissible displacement function [57].

$$\mathbf{\Pi}(\mathbf{u_{ex}}) = \min_{\mathbf{u} \in \Omega} \mathbf{\Pi}(\mathbf{u}) \tag{2.27}$$

Following [59] the left hand side of Equation 2.26 is called the bilinear form of the internal work

$$\mathcal{B}(\mathbf{u}, \mathbf{v}) = \int_{\Omega} \boldsymbol{\varepsilon}(\mathbf{v}) \; \boldsymbol{\sigma}(\mathbf{u}) \; d\Omega \tag{2.28}$$

and the right hand side of Equation 2.26 expresses the external work.

$$\mathcal{F}(\mathbf{v}) = \int_{\Omega} \mathbf{v}\mathbf{f} \; d\Omega + \int_{\Gamma_t} \mathbf{v}\mathbf{t} \; d\Gamma_t \tag{2.29}$$

The strain energy is derived from the internal work by

$$\mathcal{U}(\mathbf{u}) = \frac{1}{2} \; \mathcal{B}(\mathbf{u}, \mathbf{u}) \tag{2.30}$$

with its corresponding energy norm

$$\|\mathbf{u}\|_{E(\Omega)} \;=\; \sqrt{\mathcal{U}(\mathbf{u})} = \sqrt{\frac{1}{2}\,\mathcal{B}(\mathbf{u},\mathbf{u})}\;. \tag{2.31}$$

The systems' total potential $\mathbf{\Pi}(\mathbf{u_{ex}})$ energy used in Equation 2.27 is then expressed by:

$$\mathbf{\Pi}(\mathbf{u_{ex}}) = \mathcal{U}(\mathbf{u_{ex}}) - \mathcal{F}(\mathbf{u_{ex}}) = \frac{1}{2}\,\mathcal{B}(\mathbf{u_{ex}},\mathbf{u_{ex}}) - \mathcal{F}(\mathbf{u_{ex}})\;. \tag{2.32}$$

2.2 High-Order FEM-Approximation

In most cases it is not possible to find an exact solution for Equation 2.26. Generally u_{ex} can only be approximated. In order to achieve this, the Finite Element Method can be applied which introduces subdomains Ω_e of the total domain Ω. A set of basis functions is then defined on Ω in such a way that each basis function is non zero in the region of each Ω_e or its neighboring region. These regions Ω_e are called elements. The basis functions are constructed from polynomial functions which are defined on standard elements. Mapping functions are then used to map the standard elements onto the actual geometry. The displacement functions are introduced as follows.

$$\mathbf{u}_{FE} \;=\; \begin{bmatrix} u_x \\ u_y \\ u_z \end{bmatrix} \;=\; \mathbf{Na} \;=\; \begin{bmatrix} \sum_{i=1}^{n} a_i\; N_i(x,y,z) \\ \sum_{i=1}^{n} a_{n+i}\; N_i(x,y,z) \\ \sum_{i=1}^{n} a_{2n+i}\; N_i(x,y,z) \end{bmatrix} \tag{2.33}$$

where n is the number of basis functions used to approximate the exact solution $\mathbf{u}_{ex}$ The matrix of the basis functions $\mathbf{N}$ is:

$$\mathbf{N} \;=\; \begin{bmatrix} N_1 & N_2 & \cdots & N_n & 0 & 0 & \cdots & 0 & 0 & 0 & \cdots & 0 \\ 0 & 0 & \cdots & 0 & N_1 & N_2 & \cdots & N_n & 0 & 0 & \cdots & 0 \\ 0 & 0 & \cdots & 0 & 0 & 0 & \cdots & 0 & N_1 & N_2 & \cdots & N_n \end{bmatrix} \tag{2.34}$$

and the degrees of freedom $\mathbf{a}$ are:

$$\mathbf{a} \;=\; \left[\; a_1 \quad a_2 \quad \cdots \quad a_n \quad a_{n+1} \quad a_{n+2} \quad \cdots \quad a_{3n} \;\right]^T \quad . \tag{2.35}$$

Splitting Equation 2.34 into different sets,

$$\mathbf{N}_i \;=\; \begin{cases} \begin{bmatrix} N_i(x,y,z) \\ 0 \\ 0 \end{bmatrix} & ; \qquad i = 1,2,\ldots,n \\[2ex] \begin{bmatrix} 0 \\ N_i(x,y,z) \\ 0 \end{bmatrix} & ; \qquad i = n+1, n+2, \ldots, 2n \\[2ex] \begin{bmatrix} 0 \\ 0 \\ N_i(x,y,z) \end{bmatrix} & ; \qquad i = 2n+1, 2n+2, \ldots, 3n \end{cases} \tag{2.36}$$

it is possible to formulate the principle of virtual work (Equation 2.26) in matrix notation for all virtual basis functions $\mathbf{N}_j$.

$$\mathcal{B}\left(\sum_{i=1}^{3n} a_i \mathbf{N}_i, \mathbf{N}_j\right) = \mathcal{F}(\mathbf{N}_j) \tag{2.37}$$

Here, the expression $\mathbf{u} = \mathbf{Na}$ has to satisfy the geometric boundary conditions. The left side of Equation 2.37 can be rewritten to:

$$\begin{aligned}
\mathcal{B}\left(\sum_{i=1}^{3n} a_i \mathbf{N}_i, \mathbf{N}_j\right) &= \sum_{i=1}^{3n} a_i \; \mathcal{B}(\mathbf{N}_i, \mathbf{N}_j) && (2.38)\\
&= \sum_{i=1}^{3n} a_i \iiint\limits_{\Omega} (\mathbf{DN}_i)^T \; \mathbf{CDN}_j \; dx \; dy \; dz && (2.39)\\
&= \sum_{i=1}^{3n} a_i \sum_{e=1}^{r} \iiint\limits_{\Omega_e} (\mathbf{DN}_i^e)^T \; \mathbf{CDN}_j^e \; dx \; dy \; dz && (2.40)
\end{aligned}$$

where i and j are the degrees of freedom of the Finite Element discretization. The triple integral over the domain Ω is actually the assembly of the triple integral over the domain Ω_e of each individual Finite Element. The integral term in Equation 2.39 forms the global stiffness matrix as

$$\mathbf{K} = (k_{ij})_{i,j=1,\ldots,3n} = \left(\iiint\limits_{\Omega} (\mathbf{DN}_i)^T \; \mathbf{CDN}_j \; dx \; dy \; dz\right)_{i,j=1,\ldots,3n} \tag{2.41}$$

and the element stiffness matrix is derived by

$$\mathbf{K}^e = \left(k_{ij}^e\right)_{i,j\in I_e} = \left(\iiint\limits_{\Omega_e} (\mathbf{DN}_i^e)^T \; \mathbf{CDN}_j^e \; dx \; dy \; dz\right)_{i,j\in I_e} \tag{2.42}$$

where I_e is the set of all functions which are nonzero within the element e and $\mathbf{N}^e$ is the matrix of the basis functions within the element. Applying the differential operator matrix $\mathbf{D}$ (see Equation 2.14) to the basis functions $\mathbf{N}$ (Equation 2.34) leads to the strain-displacement matrix which is also known as the strain interpolation matrix $\mathbf{B}$.

$$\mathbf{B} = \mathbf{DN} \tag{2.43}$$

The element stiffness matrix in Equation 2.42 then simplifies to

$$\mathbf{K}^e = \iiint\limits_{\Omega_e} \mathbf{B}^{e\,T} \; \mathbf{C} \; \mathbf{B}^e \; dx \; dy \; dz \tag{2.44}$$

Having the expression for the stiffness matrix, the equation system to be solved can be derived from Equation 2.37

$$\mathbf{KU} = \mathbf{F} \tag{2.45}$$

where **U** is vector approximating the displacements. The load vector **F** can be derived analogously to the element stiffness matrices [59]:

$$\mathbf{F}^e(\mathbf{N}_j) = \mathbf{F}^e_{\Omega}(\mathbf{N}_j) + \mathbf{F}^e_{\Gamma_t}(\mathbf{N}_j) \tag{2.46}$$

with

$$\mathbf{F}^e_{\Omega}(\mathbf{N}_j) = \iiint\limits_{\Omega^e} \mathbf{N}_j^T \mathbf{f}\ dx\ dy\ dz \tag{2.47}$$

$$\mathbf{F}^e_{\Gamma_t}(\mathbf{N}_j) = \iint\limits_{\Gamma_t} \mathbf{N}_j^T \mathbf{t}\ d\Gamma_t \quad . \tag{2.48}$$

2.2.1 Mapping Functions

The basis functions used in Equation 2.34 which will be further discussed in Section 2.2.2 are defined on a standard element. In order to apply these basis functions to more generally shaped elements with the same number of degrees of freedom, mapping functions $\mathbf{Q}^e$ are applied to transform the standard element to the real element, usually given in cartesian coordinates $\mathbf{x}$. Two different coordinate systems are used to distinguish between the two settings. For quadrilateral elements, the standard elements' coordinate system is specified in the local coordinates $\boldsymbol{\xi}$, within the region $\Omega_{st} = [(-1,1) \times (-1,1) \times (-1,1)]$.

$$\mathbf{x} = \mathbf{Q}^e(\xi, \eta, \zeta) \tag{2.49}$$

In order to obtain the elements' stiffness matrix, the strain-displacement relation (**B** matrix) has to be derived by differentiating the basis functions (Equation 2.43) with respect to the global coordinate system. Therefore the chain rule has to be applied after the coordinate transformation has been performed. Generally the *Jacobian matrix* **J** is being used to perform the coordinate transformation.

$$\mathbf{J} = \begin{bmatrix} \frac{\partial x}{\partial \xi} & \frac{\partial y}{\partial \xi} & \frac{\partial z}{\partial \xi} \\ \frac{\partial x}{\partial \eta} & \frac{\partial y}{\partial \eta} & \frac{\partial z}{\partial \eta} \\ \frac{\partial x}{\partial \zeta} & \frac{\partial y}{\partial \zeta} & \frac{\partial z}{\partial \zeta} \end{bmatrix} \tag{2.50}$$

The base function transformations are then given as follows:

$$\begin{bmatrix} \frac{\partial N_i^{st}}{\partial \xi} \\ \frac{\partial N_i^{st}}{\partial \eta} \\ \frac{\partial N_i^{st}}{\partial \zeta} \end{bmatrix} = \mathbf{J} \begin{bmatrix} \frac{\partial N_i}{\partial x} \\ \frac{\partial N_i}{\partial y} \\ \frac{\partial N_i}{\partial z} \end{bmatrix} \tag{2.51}$$

and its inverse as:

$$\begin{bmatrix} \frac{\partial N_i}{\partial x} \\ \frac{\partial N_i}{\partial y} \\ \frac{\partial N_i}{\partial z} \end{bmatrix} = \mathbf{J^{-1}} \begin{bmatrix} \frac{\partial N_i^{st}}{\partial \xi} \\ \frac{\partial N_i^{st}}{\partial \eta} \\ \frac{\partial N_i^{st}}{\partial \zeta} \end{bmatrix} \tag{2.52}$$

It is obvious that the Jacobian matrix must not be singular in order to have an existing inverse. It is therefore important to construct the Finite Element mesh with the necessary diligence in order to avoid overlapping elements. After transformation, the expression for the element stiffness matrix given in Equation 2.44 transforms to:

$$\mathbf{K}^e = \int_{-1}^{1}\int_{-1}^{1}\int_{-1}^{1} \mathbf{B}^{eT} \; \mathbf{C} \, \mathbf{B}^e \; \det \mathbf{J} \; d\xi \; d\eta \; d\zeta \tag{2.53}$$

by making use of

$$dx \; dy \; dz = \det \mathbf{J} \; d\xi \; d\eta \; d\zeta \tag{2.54}$$

Applying this to the load vector components given in Equation 2.46, they transform to:

$$\mathbf{F}^e_{\Omega}(\mathbf{N}_j) \;\; = \;\; \int_{-1}^{1}\int_{-1}^{1}\int_{-1}^{1} \mathbf{N}_j^T \mathbf{f}_{\Omega} \;\; \det \mathbf{J} \; d\xi \; d\eta \; d\zeta \tag{2.55}$$

$$\mathbf{F}^e_{\Gamma_t}(\mathbf{N}_j) \;\; = \;\; \int_{-1}^{1}\int_{-1}^{1} \mathbf{N}_j^T \mathbf{t} \;\; \det \mathbf{J} \; d\boldsymbol{\xi} \tag{2.56}$$

2.2.2 General Shape Functions

The shape functions **N** presented in Section 2.2.1 are used as ansatz functions for the Finite Elements. Ansatz functions were already introduced before 1940, but were until then only used to define an ansatz in a global form over the whole domain [11]. The decomposition of the domain into a finite number of elements and ensuring the ansatz on them was the beginning of the FEM. Polynomial function N_i^e defined on the elements Ω_e are assembled to form piecewise polynomials defined on the whole domain Ω. In general the local shape functions N_i^e are constructed in such a way that C^0 continuity of the global shape function N_i over element boundaries is guaranteed. This means, that the displacement functions at element boundaries are continuous but in general not differentiable. Continuity is not asked for in the discontinuous Galerkin method [96].

Depending on the chosen Finite Element Method, different types of basis functions are needed. One generally distinguishes between the h- and the p-version of the FEM. Both versions are well established and verified, but have significant differences.

> The h-version of the Finite Element Method obtains convergence by increasing the number of elements and using a fixed polynomial degree of mostly one or two. It often applies an isoparametric element concept by using the same polynomial shape functions for the elements' geometric representation and its displacements. This concept is widely used and the h-version is applicable to a large variety of linear and non-linear problems. Due to the fact that the shape functions' polynomial degree is usually uniform in space and equal to either one, two, or three, arbitrarily curved geometries can only be approximated by these functions. In order to describe a given (especially curved) geometry exactly with these low order polynomial functions and sufficient accuracy, the domain has to be resolved with many small elements to limit the geometric discretization error. The

smaller the elements are, the better does the approximation matches the real physics. It is therefore possible to control the discretization error and derive a converging system. Elements of low order should be typically restricted to an aspect ratio of around one (smaller than two) and are prone to show locking effects. These locking effects lead to an underestimation of the displacements, due to an overestimation of the structural stiffness. More informations can be found in [6], [45], and [95]. The possible convergence rates are of algebraic type and therefore for many problem types slower than the p-versions' convergence rates [83].

The p-version achieves convergence by keeping the number of elements fixed and increases the shape functions' polynomial degree instead. The elements are generally large and the elements' aspect ratio can be very large without significantly reducing the accuracy. Different polynomial degrees can be chosen in the different local directions of the element. As the mesh is usually coarse, it is crucial to guarantee a good geometric representation, especially of the objects boundary. It can be achieved by making use of the blending function method described in Section 2.2.4. For smooth problems, exponential convergence rates can be obtained for small strain elastic problems [81] and also for finite strain hyperelastic applications [20], [41], [91].

The type of basis functions used for the h- and the p-version is crucial for their respective convergence characteristics. For the p-version, when high order polynomials are used, the matrices' condition number is very much depending on the chosen polynomial basis. A general introduction into Finite Element ansatz spaces as well as basic properties of Lagrange and Legendre polynomials is given in the following Section 2.2.3.

2.2.3 Hierarchic Shape Functions used for High-Order Finite Elements

In the following we will focus on the p-version of the Finite Element Method and its extensions, following closely [81] and [19]. Different sets of basis functions do generally span the same Finite Element space. Nevertheless the choice of the set of basis functions can have influences on the performance of the numeric simulation. The most widely-used space for low order Finite Elements is defined by Lagrange polynomials. For high-order ansatz spaces either Legendre polynomials or Non-Uniform Rational B-Splines (NURBS) can be used. The latter currently draw large attention due to their use in the isogeometric analysis concept [12]. Szabó and Babuška [81] encouraged the use of Legendre polynomials for constructing high-order ansatz spaces. They are structured in such a way that the shape functions of low order are included in the set of higher-order shape functions. As usually the derivatives of the shape functions are used in the FEM approach, another interesting and convenient property of the integrated Legendre polynomials is beneficial. In the one dimensional case, they form an orthogonal basis with respect to the bilinear form and therefore have a very positive influence on the condition number of the stiffness matrix, even in higher dimensions.

2.2.3.1 One Dimensional Hierarchic Shape Functions

In the one dimensional space for the two node standard element $\Omega_{st} = [-1, 1]$, the first two linear basis functions $N_1(\xi)$ and $N_2(\xi)$ are given in Equation 2.57 and 2.58. They form the basis of both, the standard Lagrange as well as the hierarchic Legendre basis and are common to be used in the regular h-version of the Finite Element Method. These first two modes are *nodal based* because either of the two nodes has a value of one and the other one a value of zero.

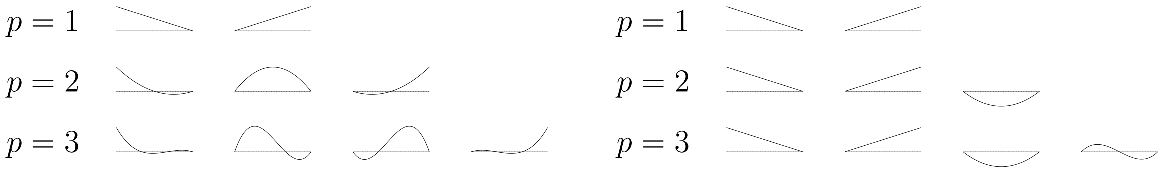

Figure 2.3: Set of one-dimensional standard basis functions for p = 1, 2, 3 on the left and hierarchical basis functions on the right

The *nodal based* higher-order Lagrange polynomials shown in Figure 2.3 on the left have equidistant nodes in the interval of [-1,1]. As a consequence always one of these shape functions has at one node the value of one and at all other nodes a value of zero. The integrated Legendre polynomials, plotted for $p = 1$, 2, and 3 in Figure 2.3 on the right have a hierarchic basis and are in contrast to the Lagrange basis, *modal based.* The general Legendre basis is derived by:

$$N_1(\xi) = 1/2(1-\xi) \tag{2.57}$$

$$N_2(\xi) = 1/2(1+\xi) \tag{2.58}$$

$$N_i(\xi) = \phi_{i-1}(\xi), \quad i = 3,4,\ldots,p+1 \tag{2.59}$$

of which the first two linear basis functions $N_1(\xi)$ and $N_2(\xi)$ (equations 2.57 and 2.58) are nodal based. The additional higher-order polynomial functions $N_i(\xi)$ for $3 \leq i \leq p+1$ enrich the ansatz space with the corresponding polynomial function without referring to actual nodes (for $p > 1$). These higher modes vanish on the element boundaries (see Equation 2.60) and only influence the interior domain. This motivates their name as *internal* or *bubble modes.*

$$N_i(-1) = N_i(1) = 0, \quad i = 3,4,\ldots \tag{2.60}$$

The Legendre polynomials $\{L_n(x)\}_{n=0}^{\infty}$ are solutions of the Legendre differential equation

$$((1-x^2)y')' + n(n+1)y = 0, \quad x \in (-1,1), \quad n = 0,1,2,\ldots \tag{2.61}$$

and are used to derive the integrated Legendre polynomials $\phi_j(\xi)$ applied in Equation 2.59:

$$\phi_j(\xi) = \sqrt{\frac{2j-1}{2}} \int_{-1}^{\xi} L_{j-1}(x)\,dx = \frac{1}{\sqrt{4j-2}}\left(L_j(\xi) - L_{j-2}(\xi)\right), \quad j = 2,3,\ldots \tag{2.62}$$

which form the basis functions for the p-version of the Finite Element Method. The Legendre polynomials $\{L_n(x)\}_{n=0}^{\infty}$ can be obtained by applying the Rodriguez formula

$$L_n(x) = \frac{1}{2^n\,n!}\frac{d^n}{d\,x^n}\left(x^2-1\right)^n, \quad x \in (-1,1), \quad n = 0,1,2,\ldots \tag{2.63}$$

or Bonnet's recursion formula [81].

$$L_n(x) = \frac{1}{n}\left[(2n-1)xL_{n-1}(x) - (n-1)L_{n-2}(x)\right], \quad x \in (-1,1),\ n = 2,3,4,\ldots \tag{2.64}$$

with the first two Legendre polynomials being $L_0(x) = 1$ and $L_1(x) = x$.
The Legendre polynomials are orthogonal in the interval of $I = (-1, 1)$ which is expressed by the following term:

$$\int_{-1}^{1} L_n(x) L_m(x)\, dx = \begin{cases} \dfrac{2}{2n+1} & \text{if} \quad n = m \\ 0 & \text{else} \end{cases} \tag{2.65}$$

It leads to the fact (see [19], [66]) that the condition number of the resulting stiffness matrix is improved, compared to the Lagrangian basis [93] when higher polynomial spaces are used. The Lagrange basis, which is nodal based for all polynomial degrees, fulfills the partition of unity.

$$\sum_{1}^{p+1} N_i^p(\xi) = 1 \tag{2.66}$$

This does generally not hold for the Legendre basis and polynomial degrees of $p > 1$. Here already the first two hierarchic base functions $N_1(\xi)$ and $N_2(\xi)$ fulfill the partition of unity. Additional shape functions for $p > 1$ therefore exceed this unity property in the hierarchic concept.

2.2.3.2 Two Dimensional Hierarchic Shape Functions

Figure 2.4 depicts the standard quadrilateral Finite Element on which the implementation of the p-version in two dimensions is based. The quadrilateral element formulation is using the ansatz functions introduced by Szabó and Babuška [81].

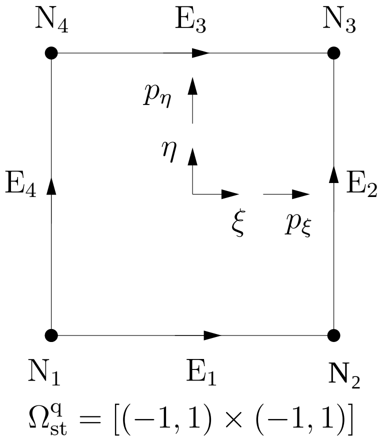

Figure 2.4: Standard quadrilateral element: definition of nodes, edges and polynomial degree

The shape functions in two-dimensions can be classified into three groups [40]:

1. **Nodal modes:** The nodal modes

$$N_{1,1}^{\mathrm{N}_i}(\xi, \eta) \quad = \quad \frac{1}{4}\,(1 + \xi_i\, \xi)(1 + \eta_i\, \eta)\,, \quad i = 1, ..., 4 \tag{2.67}$$

are the standard bilinear shape functions, well known from the isoparametric four-noded quadrilateral element. The local coordinates $(\pm 1, \pm 1)$ of the ith node are named (ξ_i, η_i). The mode for node 1 is shown in Figure 2.5.

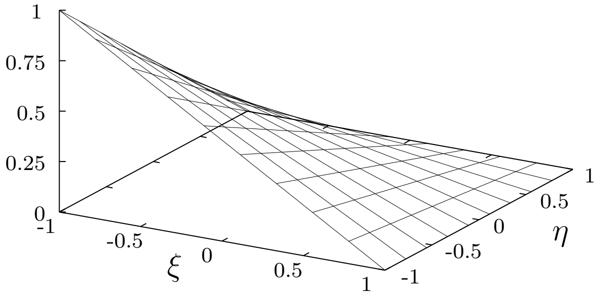

Figure 2.5: Standard bilinear shape function for node 1: $N_{1,1}^{\mathrm{N}_1}(\xi,\eta) = \frac{1}{4}(1-\xi)(1-\eta)$

2. **Edge modes:** The edge modes are defined separately for each individual edge. They vanish at all other edges. For $p \geq 2$ there exist $2(p_\xi - 1) + 2(p_\eta - 1)$ edge modes. The corresponding $2(p_\xi - 1)$ modes for edge E_1 and E_3 in ξ-direction read:

$$N_{i,1}^{\mathrm{E}_1}(\xi,\eta) = \frac{1}{2}\,\phi_i(\xi)(1-\eta), \quad i = 2, \dots p_\xi, \tag{2.68}$$

$$N_{i,1}^{\mathrm{E}_3}(\xi,\eta) = \frac{1}{2}\,\phi_i(\xi)(1+\eta), \quad i = 2, \dots p_\xi\ . \tag{2.69}$$

The $2(p_\xi - 1)$ modes for edge E_2 and E_4 in η-direction are:

$$N_{1,i}^{\mathrm{E}_2}(\xi,\eta) = \frac{1}{2}\,(1+\xi)\phi_i(\eta), \quad i = 2, \dots p_\eta, \tag{2.70}$$

$$N_{1,i}^{\mathrm{E}_4}(\xi,\eta) = \frac{1}{2}\,(1-\xi)\phi_i(\eta), \quad i = 2, \dots p_\eta\ . \tag{2.71}$$

In Figure 2.6 the mode for edge 1 with $i = 2$ is plotted.

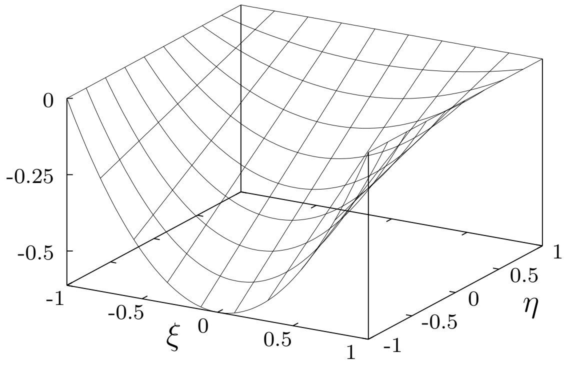

Figure 2.6: Quadratic shape function forming the edge mode of edge 1 ($i = 2$): $N_{2,1}^{\mathrm{E}_1}(\xi,\eta) = \frac{1}{2}(1-\eta)\phi_2(\xi)$

3. **Internal modes (bubble modes):** The number of internal modes for the tensor product space is $(p-1)(q+1)$, with $(p, q \geq 2)$. For the trunk space the internal modes appear the first time for higher polynomial orders of $p \geq 4$ [81]. All internal modes

$$N_{i,j}^{\text{int}}(\xi,\eta) \quad = \quad \phi_i(\xi)\phi_j(\eta) \tag{2.72}$$

   are purely local and vanish at the edges of the quadrilateral element. Figure 2.7 depicts the internal mode for $i = j = 2$.

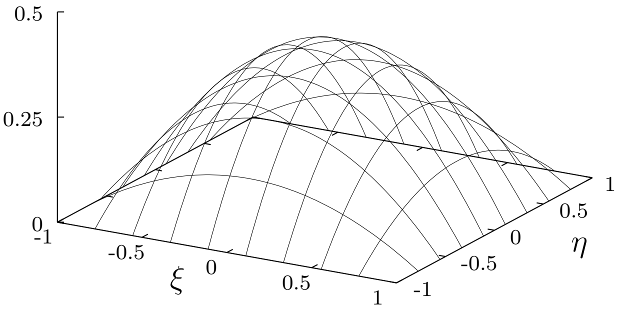

Figure 2.7: Internal mode $(i = j = 2)$: $N_{2,2}^{\text{int}}(\xi,\eta) = \phi_2(\xi)\phi_2(\eta)$

The index of the shape function i, j denote the polynomial degree of p_ξ and p_η in the local direction ξ, η of the standard element $\Omega_{\text{st}}^{\text{q}}$.

2.2.4 The Blending Function Method

As already mentioned in Section 2.2.2, the h- and the p-version of the FEM differ with respect to the geometric discretization. The isoparametric element concept used for the h-version couples the ansatz for the geometry with the ansatz for the displacement field [87, 94]. In order to get a converged solution, the element size is gradually reduced. With this the geometric discretization error is reduced as well, as the smaller elements give a better approximation of the actual geometry. When the p-version is used, one needs to be able to represent the bounding geometry independent of the chosen polynomial ansatz space. Thus coarse meshes with large elements can be chosen to discretize the domain. One method to describe the geometry of even complex structures is the blending function method introduced by Gordon and Hall [34, 35]. In comparison with the isoparametric concept it leads to an improved quality of the solution [44].

2.2.4.1 Two Dimensional Blending

Figure 2.8 shows the transformation $\mathbf{Q}^e(\boldsymbol{\xi}) = [Q_x^e(\boldsymbol{\xi}), Q_y^e(\boldsymbol{\xi})]^T$ of a quadrilateral standard element $\Omega_{\text{st}}^{\text{q}} = [(-1,1) \times (-1,1)]$ with local coordinates $\boldsymbol{\xi} = [\xi,\eta]^T$ to a general quadrilateral element with global coordinates $\mathbf{x} = [x,y]^T$. Its four nodes $\mathbf{X}_i = [X_i, Y_i]^T$ with $i = 1, ..., 4$ and edges $\mathbf{E}_i = [E_{ix}, E_{iy}]^T$ with $i = 1, ..., 4$ define the element geometry in $\mathbb{R}^2$.

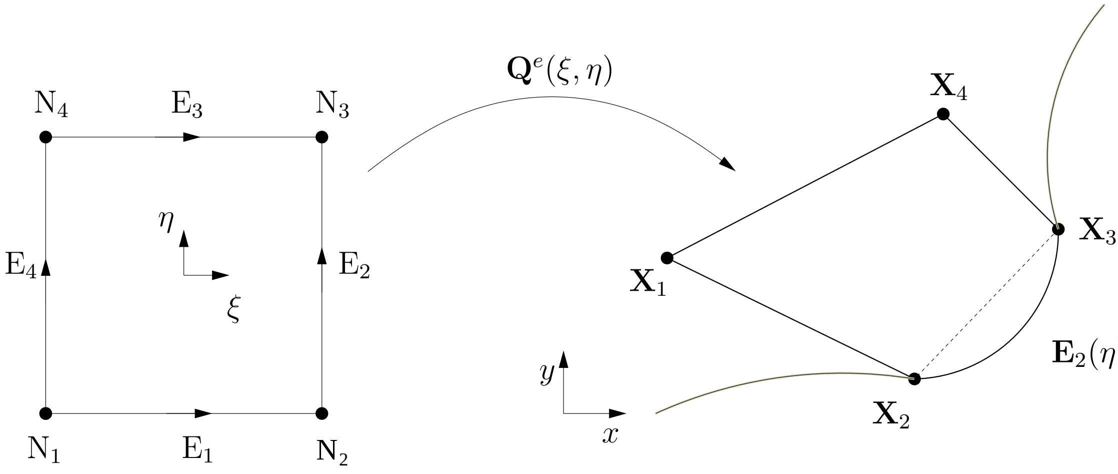

Figure 2.8: Concept of blending function method for quadrilateral element

The edges' geometry is defined by the parametric curve description:

$$\mathbf{E}_i = \begin{bmatrix} E_{ix}(\xi) \\ E_{ix}(\xi) \end{bmatrix} \quad i = 1,3 \qquad \mathbf{E}_j = \begin{bmatrix} E_{jx}(\eta) \\ E_{jx}(\eta) \end{bmatrix} \quad j = 2,4 \qquad \{\xi,\eta\} \in [-1,1] \tag{2.73}$$

Equation 2.74 gives the general blending from the local parameter space $\boldsymbol{\xi} = [\xi,\eta]^T$ into the global, cartesian space $\mathbf{x} = [x,y]^T$.

$$\mathbf{x} \;=\; \mathbf{Q}^e(\xi,\eta) \;=\; \sum_{i=1}^{4} N_{1,1}^{\mathrm{N}_i}(\xi,\,\eta)\,\mathbf{X}_i + \sum_{i=1}^{4} \mathbf{e}_i(\xi,\,\eta) \tag{2.74}$$

The first term in Equation 2.74 correlates with the standard bilinear mapping of an isoparametric quadrilateral with linear shape functions $N_{1,1}^{\mathrm{N}_i}(\xi,\,\eta)$. The second term accounts for the curved geometry of the edge and will be further discussed in Equation 2.75 on local edge number two E$_2(\eta)$, going through the points $\mathbf{X}_2$ and $\mathbf{X}_3$. It generally augments the bilinear mapping of the first term by the difference between the curve $\mathbf{E}_2(\eta)$ and the straight line connecting N$_2$ and N$_3$ (see the part in the square bracket in Equation 2.75).

$$\mathbf{e}_2(\xi,\,\eta) \;=\; \left[\mathbf{E}_2(\eta) \;-\; \left(\frac{1-\eta}{2}\,\mathbf{X}_2 + \frac{1+\eta}{2}\,\mathbf{X}_3\right)\right]\;\frac{1+\xi}{2} \tag{2.75}$$

The blending term $[(1+\xi)/2]$ assures that the geometric blending of edge E$_2$ fades out linearly to the opposing edge E$_4$, where $(1+\xi)/2 = 0$. For the case of a quadrilateral with curved edges on each side, Equation 2.74 turns to:

$$\begin{aligned} \mathbf{x} \;=\; & \frac{1}{2}\left[\,(1-\eta)\mathbf{E}_1(\xi) \,+ (1+\xi)\mathbf{E}_2(\eta) \,+ (1+\eta)\mathbf{E}_3(\xi) \,+ (1-\xi)\mathbf{E}_4(\eta)\,\right] \\ & -\,[\;N_{1,1}^{\mathrm{N}_1}(\xi,\,\eta)\,\mathbf{X}_1 + \,N_{1,1}^{\mathrm{N}_2}(\xi,\,\eta)\,\mathbf{X}_2 + \,N_{1,1}^{\mathrm{N}_3}(\xi,\,\eta)\,\mathbf{X}_3 + \,N_{1,1}^{\mathrm{N}_4}(\xi,\,\eta)\,\mathbf{X}_4\;] \end{aligned} \tag{2.76}$$

Chapter 3

Contact Mechanics

The following section gives an introduction into the topic of contact mechanics. Its main focus is to show the basic equations and definitions related to this topic. For a profound review of the theory of contact mechanics the monographs of Wriggers [88], Laursen [54], and Wriggers & Zavarise [89] are referred to. The introduction in this sections follows closely [24, 37, 54, 89, 88, 90].

The mathematical description of contact problems leads even for the special case of small deformations to a nonlinear problem. The nonlinearity derives from the fact, that the system's boundary conditions change during the simulation due to the contact deformation. Only a few analytical solutions exist for the solution of the evolving nonlinear relations for simple geometries. Due to the problem's intrinsic geometric nonlinearity, its solution is time consuming when numerical methods are applied.

Any continuum problem with hyperelastic material can be treated as a minimization problem [89], meaning that the system's total potential energy assumes a minimum at the solution point.

$$\mathbf{\Pi}(\mathbf{u}) \rightarrow MIN \tag{3.1}$$

In the case of static contact problems, the minimization is restricted by the set of all possible contact constraints $\mathbf{G}_c(\mathbf{u})$, thus leading to an inequality constrained minimization problem.

$$\begin{aligned} &\text{minimize} && \mathbf{\Pi}(\mathbf{u}) && (3.2)\\ &\text{subject to} && \mathbf{G}_c(\mathbf{u}) \geq \mathbf{0} && (3.3) \end{aligned}$$

In order to solve the contact problems, special attention has to be drawn to the contact detection. For complex structures with a priori unknown contact regions, the contact search has to be performed in every time step, load step and iteration of the numerical simulation. Therefore the contact search often dominates the computation which is usually split into a global and a local algorithmic task.

Due to the problem's nonlinear nature, iterative algorithms have to be used. A direct solution of the Finite Element discretization

$$\mathbf{R}(\mathbf{u}) - \mathbf{P} = \mathbf{0} \tag{3.4}$$

with $\mathbf{R}(\mathbf{u})$ being the stress divergence term and $\mathbf{P}$ being the applied load, is generally not possible when the contact inequality constraint is considered. The convergence rates, or more generally the convergence behavior of the chosen iterative algorithm is therefore of crucial relevance [89].

3.1 Contact Kinematics

Given a domain Ω^γ where γ denotes the individual body with boundary Γ^γ, we can divide the boundary into parts with Dirichlet Γ^γ_D, Neumann Γ^γ_N and contact boundary condition Γ^γ_c where objects Ω^γ are in contact. In the contact interface, the boundaries of in general two objects (excluding self contact) share the same space which is referred to as the *contact boundary* of for example Γ^1_c and Γ^2_c. The following constraints have to be satisfied [37]:

$$\Gamma^\gamma_D \cup \Gamma^\gamma_N \cup \Gamma^\gamma_c = \partial\Omega^\gamma \quad \textit{and} \quad \Gamma^\gamma_D \cap \Gamma^\gamma_N = \Gamma^\gamma_N \cap \Gamma^\gamma_c = \Gamma^\gamma_D \cap \Gamma^\gamma_c = 0 \qquad \forall\gamma \in \mathbb{N} \tag{3.5}$$

The contact boundary condition can be split into a normal and a tangential part which will be discussed later.
A point with initial position $\mathbf{X}^\gamma$ on object Ω^γ is being deformed by $\mathbf{u}^\gamma$ to the current position $\mathbf{x}^\gamma$ where γ denotes the respective body (see Equation 2.2 for comparison).

$$\mathbf{x}^\gamma = \mathbf{X}^\gamma + \mathbf{u}^\gamma \tag{3.6}$$

Figure 3.1 shows two deformable bodies which come into contact.

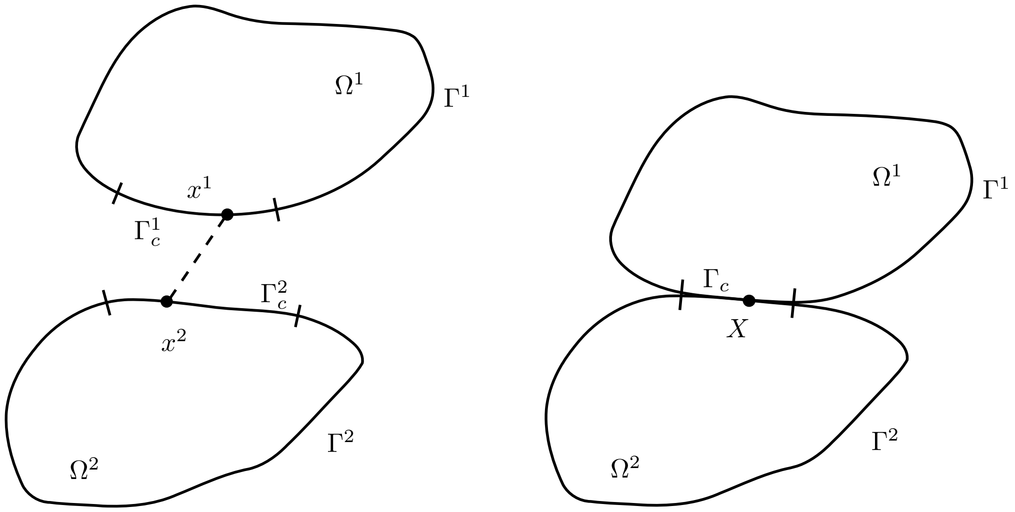

Figure 3.1: Geometrical setup of two contacting bodies.

3.2 Normal Contact

Two conditions have to be fulfilled simultaneously in order to satisfy the contact constraints in normal direction. One is the *non-penetration* condition and the other one is the *compressive stress* condition. The first condition prevents that two objects occupy the same space and the second assures that only compressive stresses are present in the contact interface. Adhesion and therefore tensile forces are nor allowed in this formulation.
The normal distance between two points $\mathbf{x}^2$ and $\mathbf{x}^1$ living on Γ^1_c and Γ^2_c can be defined via the gap function g_N as

$$g_N = (\mathbf{x}^2 - \mathbf{x}^1) \cdot \mathbf{n}^1 \tag{3.7}$$

with $\mathbf{n}^1$ being the outward normal on $\mathbf{x}^1$ of Γ_c^1 [24, 90].
The physical requirements (geometric constraint) of impenetrability of the contacting objects is enforced by the normal contact constraint as stated above. For this we can define the non-penetration condition as:

$$g_N \geq 0 \tag{3.8}$$

This inequality condition is then resolved by splitting it into the penetration function $\bar{g}_N$ for the case of contact and a case when no contact is present.

$$\bar{g}_N = \begin{cases} (\mathbf{x}^2 - \mathbf{x}^1) \cdot \mathbf{n}^1 & \text{if} \quad (\mathbf{x}^2 - \mathbf{x}^1) \cdot \mathbf{n}^1 < 0 \\ 0 & \text{otherwise} \end{cases} \tag{3.9}$$

The normal contact pressure (normal component of the contact traction) and the gap function are connected through the second and third Kuhn–Tucker condition:

$$p_N \leq 0 \tag{3.10}$$

$$g_N \, p_N = 0 \tag{3.11}$$

where p_N is the contact pressure in the contact interface [90]. Equation 3.10 implies that only compressive contact stresses can occur in the contact interface, while tensile stresses are prohibited. Equation 3.11 states that either the gap g_N, or the compressive stress p_N is always zero (complementarity condition). In the case of a positive gap, the contacting objects are separated and no active contact constraints, respective contact stresses, are present. For the case of a closed gap ($\bar{g}_N = 0$), positive contact stresses develop in the contact interface. A visual representation of the Kuhn-Tucker conditions is plotted in Figure 3.2. The bold line represents the admissible combination of g_N and p_N. From Figure 3.2 it is clear, that in the case of contact ($g_N = 0$), the function of the Kuhn-Tucker condition is ambiguous, discontinuous, and therefore not differentiable.

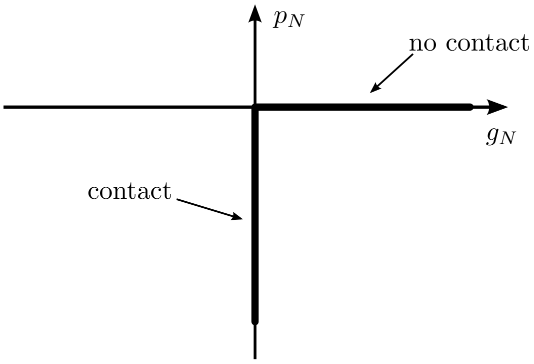

Figure 3.2: Visualization of Kuhn-Tucker condition for normal contact.

Another effect that is related with the normal contact behavior is the effect of adhesion. It takes into consideration that tensile forces between the objects can develop in the contact interface due to e.g. van der Waals attraction between interacting bodies. This field of study has not yet gained much attention in the past, but studies have lately been performed for example by Sauer [67].

3.3 Tangential Contact

The relative tangential movement of two objects which are unconstrained in tangential direction is restricted, when frictional contact effects are taken into account. Therefore, in addition to the contact description in normal direction, contact conditions for the tangential direction have to be considered as well. Normal and tangential contact constraints are required to fully describe the interaction between non-connected objects. In the following the basic contact parameters for the frictional contact will be introduced by using the Coulomb friction model. The Coulomb friction model is the classical and relatively simple model to incorporate the effect of sliding into the computation. Nevertheless, more complex models could be used instead (see Hartmann [37]).

The friction coefficient μ is a coefficient that is used to describe the capability of an individual material to carry loads in tangential direction in the contact interface. This is a physical property which is different for each material as it depends on the material's surface roughness on the microlevel and its Young's modulus. It is usually derived from experiments. With the friction coefficient μ, an interrelation between the normal and tangential traction p_T can be formulated.

$$\|p_T\| \leq \mu \cdot \ p_N \tag{3.12}$$

The tangential traction is therefore bounded by a fraction of the normal traction. Within the tangential traction a difference has to be made between the *sticking* and the *slipping* state.

$$\begin{aligned} \|p_T\| &< \mu \cdot \ p_N \quad \text{in case of stick} & (3.13)\\ \|p_T\| &= \mu \cdot \ p_N \quad \text{in case of slip} & (3.14) \end{aligned}$$

For the tangential force smaller than $\mu \cdot \ p_N$, no relative tangential motion exists between the contacting partners and the system is in a sticking state. For the tangential force exceeding $\mu \cdot \ p_N$, the value is set to $\mu \cdot \ p_N$ thus allowing the objects to slide.

The relative tangential motion of two contacting objects for the case of stick can be formulated in terms of a tangential gap function. In the case of *stick*, the relative tangential movement between the colliding objects is zero in the contact interface. Equation 3.15 gives the tangential gap g_T in the case of stick, with $\mathbf{n}_t^1$ being the tangent vector on Γ_c^1

$$g_T = (\mathbf{x}^2 - \mathbf{x}^1) \cdot \mathbf{n}_t^1 = 0 \tag{3.15}$$

Slip occurs when points on Γ_c^1 slide in tangential direction on Γ_c^2. For this case the load is bounded by the value of $\mu \cdot \ p_N$, and the tangential gap is smaller or larger than zero.

$$\|g_T\| = \left\|(\mathbf{x}^2 - \mathbf{x}^1) \cdot \mathbf{n}_t^1\right\| \neq 0 \tag{3.16}$$

As pictured in Figure 3.3, the Kuhn-Tucker condition for tangential contact shows that the tangential gap g_T is zero in the case of stick. When the tangential contact force is exceeding the critical value of $\mu \cdot \ p_N$, the contact boundaries start to slide on each other. Here it should be noted that the frictional term is path dependent and therefore strongly depends on the direction of the applied load.

The effect of thermo-mechanical contact and wear are not considered in this study. It should be noted that they are a matter of and therefore related to frictional contact mechanics (see [88]).

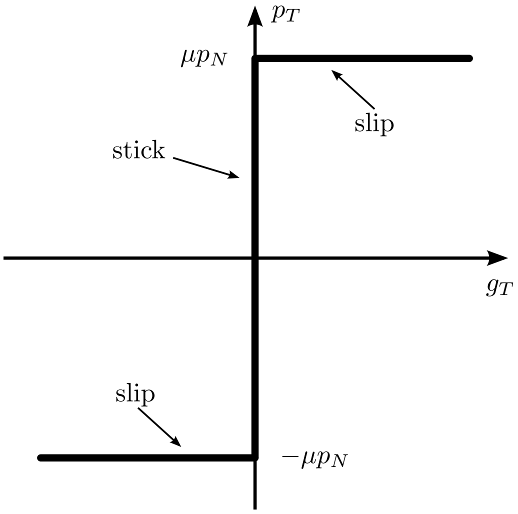

Figure 3.3: Visualization of Kuhn-Tucker condition for tangential contact.

3.4 Weak Form of Contact

The weak form of contact is derived from Equation 2.32 which was introduced earlier in Section 2.1.5. It can be modified in such a way that it accounts for the behavior of two independent objects $\Omega^\gamma,\ \gamma = 1, 2$ without contact as shown in Equation 3.17.

$$\sum_{\gamma=1}^{2} \left\{ \frac{1}{2} \int_{\Omega^\gamma} \boldsymbol{\varepsilon}^\gamma(\mathbf{v})\ \boldsymbol{\sigma}^\gamma(\mathbf{u})\ d\Omega - \int_{\Omega^\gamma} \mathbf{f}^\gamma \mathbf{v}^\gamma\ d\Omega - \int_{\Gamma^\gamma} \mathbf{t}^\gamma \mathbf{v}^\gamma\ d\Gamma \right\} = 0 \tag{3.17}$$

The two objects are treated separately and do not interact. Enhancing Equation (3.17) with an additional term Π_c, leads to a formulation of the total energy which accounts for contact phenomena[1].

$$\sum_{\gamma=1}^{2} \left\{ \frac{1}{2} \int_{\Omega^\gamma} \boldsymbol{\varepsilon}^\gamma(\mathbf{v})\ \boldsymbol{\sigma}^\gamma(\mathbf{u})\ d\Omega - \int_{\Omega^\gamma} \mathbf{f}^\gamma \mathbf{v}^\gamma\ d\Omega - \int_{\Gamma^\gamma} \mathbf{t}^\gamma \mathbf{v}^\gamma\ d\Gamma \right\} + \Pi_c = 0 \tag{3.18}$$

3.5 Contact Constraints

There are several different methods available to enforce the contact constraints. Formulations for Π_c given in Equation (3.18), are for example the penalty method, the barrier method, the augmented Lagrangian method, the Lagrange multiplier method, or the mortar method. The two three of these methods, satisfy the Kuhn-Tucker conditions exactly whereas the first three methods (penalty, barrier, and augmented Lagrangian method) do only fulfill the Kuhn-Tucker conditions approximatively. They either violate the non-penetration condition $g_N \geq 0$ (penalty and augmented Lagrangian method), or the complementarity condition $g_N p_N = 0$ (penalty, barrier, and augmented Lagrangian method). A detailed description of the aforementioned

---

[1] Note that in the case of frictional sliding contact the solution becomes dissipative and therefore path-dependent. Hence the presented formulation is only valid for non frictional contact [88, 89].

methods can be found in [54] and [88]. In this work, the penalty method is chosen in order to incorporate the contact constraints into the Finite Element formulation. A brief summary of the penalty method is given in the next paragraph.
The name of the penalty method stems from the fact, that it penalizes a violation of the non-penetration condition (Equation 3.8). When a penetration of one body into another one is detected, it will be penalized by adding a large stiffness and a corresponding force to the elements in contact. From a mechanical point of view, the penalty method puts, in case of penetration, a spring with large stiffness ϵ in between the contacting nodes/edges. Applying the penalty method, the contact term Π_c in Equation (3.18) can be modeled by

$$\Pi_c^P = \frac{1}{2} \int\limits_{\Gamma_c} (\epsilon_N (\bar{g_N})^2 + \epsilon_T \; \mathbf{g_T} \cdot \mathbf{g_T}) \; d\Gamma \;, \quad \epsilon_N, \epsilon_T > 0. \tag{3.19}$$

The contact boundary of the body is represented by Γ_c, ϵ_N and ϵ_T are the penalty parameters in the normal and tangential direction respectively [88]. The normal gap between the objects is given by g_N, which is greater than (no contact), or equal to zero. In case of penetration, the active normal gap values are denoted by $\bar{g_N}$. In the case of friction, $\mathbf{g_T}$ denotes the movement in tangential direction.
The variation of Equation (3.19) yields Equation (3.20) which is valid for the case of stick[2].

$$\delta\Pi_c^{P \; stick} = \int\limits_{\Gamma_c} (\epsilon_N \bar{g_N} \delta\bar{g_N} + \epsilon_T \; \mathbf{g_T} \cdot \delta\mathbf{g_T}) \; d\Gamma \;, \quad \epsilon_N, \epsilon_T > 0 \tag{3.20}$$

In the case of slip, the virtual work includes the tangential stress given by the constitutive law of frictional sliding (like the Coulomb friction model, Section 3.3) [88, 24].

$$\delta\Pi_c^{P \; slip} = \int\limits_{\Gamma_c} (\epsilon_N \bar{g_N} \delta\bar{g_N} + \mathbf{t_T} \cdot \delta\mathbf{g_T}) \; d\Gamma \;, \quad \epsilon_N > 0 \tag{3.21}$$

Considering only normal contact, Equation (3.19) reduces to:

$$\Pi_c^P = \frac{1}{2} \int\limits_{\Gamma_c} \epsilon_N (\bar{g_N})^2 d\Gamma \tag{3.22}$$

which clearly illustrates the mechanical idea behind the penalty method method. Taking the penalty parameter ϵ_N as the spring stiffness, and $\bar{g_N}$ as the penetration of the two bodies, it is obvious that Π_c^P corresponds to the strain energy of a linear elastic spring distributed over the contact boundary Γ_c, connecting the two bodies. From this it is evident that the non-penetration condition of Equation 3.8 is not fulfilled exactly in general. Only for the case of an infinite value of the penalty parameter, the penetration converges to zero and satisfies the non-penetration condition, see [50] and [56]. However, large numbers of ϵ_N and ϵ_T lead to an ill-conditioned numerical problem [88]. The behavior for increasing values of the penalty parameter is tested on a simple unilateral example setup shown in Figure 3.4(a), where the two

---

[2] Be aware that by using the penalty method to incorporate the contact constraints, a relative (tangential) motion between the sticking contact partners is possible.

domains Ω_1 and Ω_2 are initially not in contact, having an infinitesimal gap. The convergence of the penetration, strain, and strain energy is shown in Figure 3.4(b) and plotted in a double logarithmic scale. Herein the error in the strains is computed by $\sqrt{|\varepsilon_{ref} - \varepsilon_{FE}| / \varepsilon_{ref}}$ and the error in the strain energy is computed by $\sqrt{|\mathcal{U}_{ref} - \mathcal{U}_{FE}|/\mathcal{U}_{ref}}$ (here not given in percent). The penetration is an error by itself, as the penetration should be zero. The linear behavior between the penalty parameter and the plotted variables is visible. To compromise the aforementioned ill-conditioning and numerical accuracy, a penalty value of $\epsilon = 1000 * E$, with E being the Young's modulus, is used in the current (static, steady state) study as the standard value.

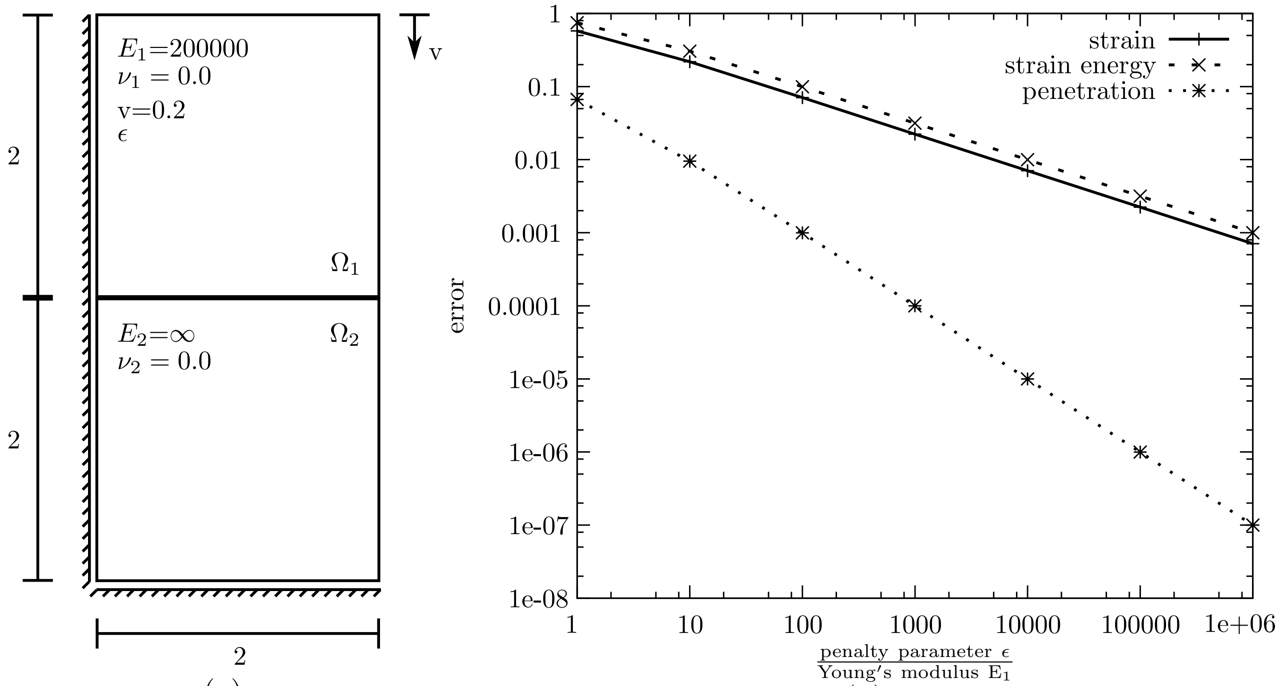

(a)

(b)

Figure 3.4: Convergence behavior for increasing values of the penalty parameter for a simple example setup.

For a numerical implementation of Equation (3.22), the integral along the contact boundary is evaluated e.g. by a Gaussian integration rule. The variation of Equation 3.22 leads to:

$$\delta\Pi_c^P = \int_{\Gamma_c} \epsilon_N \bar{g_N} \; \delta\bar{g_N} \; d\Gamma \;, \quad \epsilon_N > 0 \tag{3.23}$$

An advantage of the penalty method is that it is purely geometrically based and therefore does not introduce additional degrees of freedom to the resulting equation system. The normal contact stress is then given by:

$$p_N = \begin{cases} \epsilon_N \; g_N & \text{if} \quad g_N \leq 0 \quad \text{contact} \\ 0 & \text{if} \quad g_N > 0 \quad \text{no contact} \end{cases} \tag{3.24}$$

Figure 3.5 plots the Kuhn–Tucker condition regularized by the penalty method. The convergence of the penalty method for $\epsilon_N \rightarrow \infty$ towards the exact fulfillment of the Kuhn-Tucker

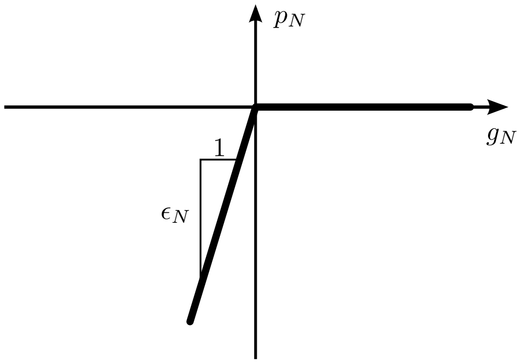

Figure 3.5: Kuhn-Tucker condition for normal contact regularized by the penalty method.

condition is clearly visible in this picture. The tangential component of the contact constraint can be regularized in a similar way.

Once the penetration $\bar{g_N}$ at a given Gauss point of an edge is computed, its value will be multiplied with the penalty parameter ϵ_N and the resulting traction is then considered during the integration of the load vector. The overall set of nonlinear equations arising from the discretization is solved by means of the Newton Raphson method. The approximated tangent stiffness matrix is computed numerically by differentiation of the residual force vector with respect to the degrees of freedom [87], thus applying the discrete Newton Raphson scheme (see Section 3.7).

3.6 Contact Interface Discretization

One of the most important and difficult tasks of describing contact problems numerically, is to capture the spacial interaction of the objects involved. The deformation of the contacting objects lead to contact stresses in the contact interface. These contact stresses have to be equal in a pointwise sense on the contacting boundaries, forming an equilibrium in the interface. The fact that the Finite Element meshes of the objects are in general non-matching in the contact interface, limits the choice of the method used for the contact discretization.

A well known and popular method to discretize the contact is the *node-to-segment* (NTS) method in which the classical master-slave concept is used. Its main idea is that any node on the slave side is not allowed to penetrate any master segment. The gap function is evaluated only at these slave nodes thus satisfying the contact constraints like the non-penetration condition only pointwise. Figure 3.6 shows the master and slave side with the corresponding nodes. The non-penetration condition is enforced on node x_1^2. In the rest of the domain, gaps and penetration along the elements can occur. This becomes evident when looking at the nodes x_1^2, x_2^2, x_3^2, x_1^1, and x_2^1 in Figure 3.7. For the case when the nodes x_1^2, x_2^2, and x_3^2, which are nodes on the slave side, fulfill the non-penetration condition by not penetrating into the master surface, nodes x_1^1 and x_2^1 will in the general case by no chance (for curved geometries) satisfy the non-penetration condition at the same time. Therefore the master nodes are not used to enforce the contact conditions, like the non-penetration condition. This also motivates why generally a finer mesh is chosen for the slave, than for the master side, in oder to get a better approximation in the contact interface. A better resolution (finer mesh) of the master surface would, in the case of single sided contact, not improve the quality of the

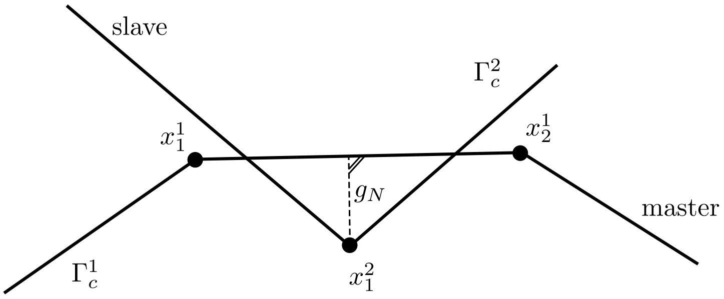

Figure 3.6: Node-to-segment contact discretization.

results significantly but increase the computational effort. Following the master-slave concept, the contact conditions are transferred from the slave to the master surface.

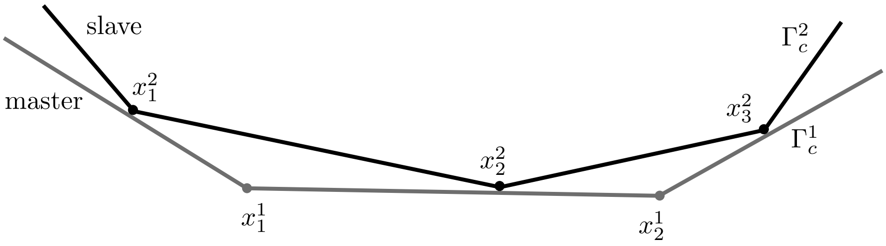

Figure 3.7: Node-to-segment contact discretization. Non-penetration condition is only fulfilled point-wise for the nodes on the slave surface.

In the case when isoparametric Finite Elements with a polynomial order of one are used to discretize the objects in contact, no smooth geometric description of the contacting boundaries exists. The geometry will only be described approximatively, leading to kinks in the geometric discretization along the boundaries. For this case, if a slave node slides from one contacting master element to its neighboring master element, the non-smooth geometric representation can lead to non-physical peaks in the corresponding contact forces. Several smoothing algorithms to overcome these peaks and jumps have been developed and can be found in [63, 65, 78]. The *segment-to-segment* (STS) approach was developed by Simo, Wriggers, and Taylor [74] to overcome the problems described for the NTS method. It discretizes the contact interface with contact segments on which the gap functions and Lagrange multipliers are interpolated (see Figure 3.8). It allows to use different interpolation schemes for the gap function and the Lagrange parameter. An intermediate contact line will then be defined inside of the contact segments which is C^1-continuous. This contact line does not has to lie in the middle of the segments, but can be placed anywhere inside the segment. Even one of the contacting surfaces can be chosen as the intermediate contact line. However this does not mean, that the interpolation of one of the contact boundaries is equivalent to the intermediate contact line since it is still C^1 continuous [88]. As the segment-to-segment approach only fulfills the non-penetration condition in an average (integral) way, gaps and penetrations can occur in the contact interface as sketched in Figure 3.9). Similar formulations were introduced by [64] and [92].

The *mortar method* is currently favored by many researchers in the field of contact mechanics. It is based on a segment-to-segment approach. Its main idea is the weak (integral) enforcement of the contact constraints in the contact interface. To enforce these constraints, the penalty and

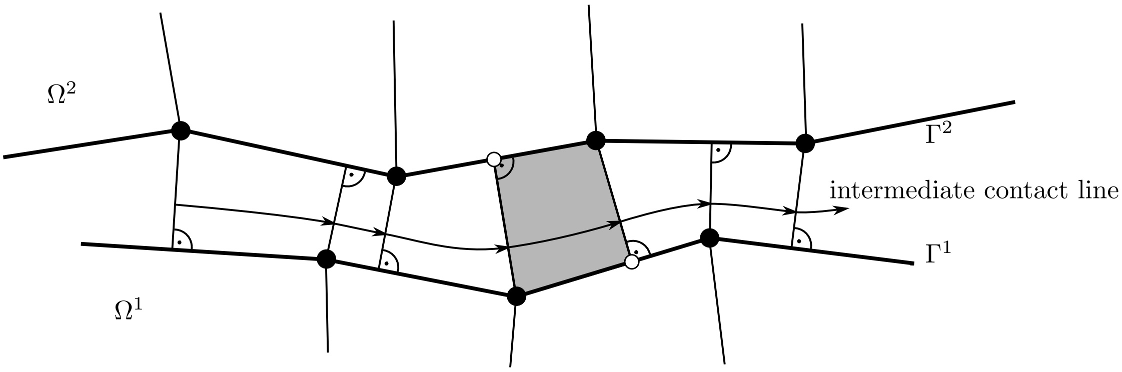

Figure 3.8: Segment-to-segment contact discretization with geometrical interpretation of the intermediate contact line.

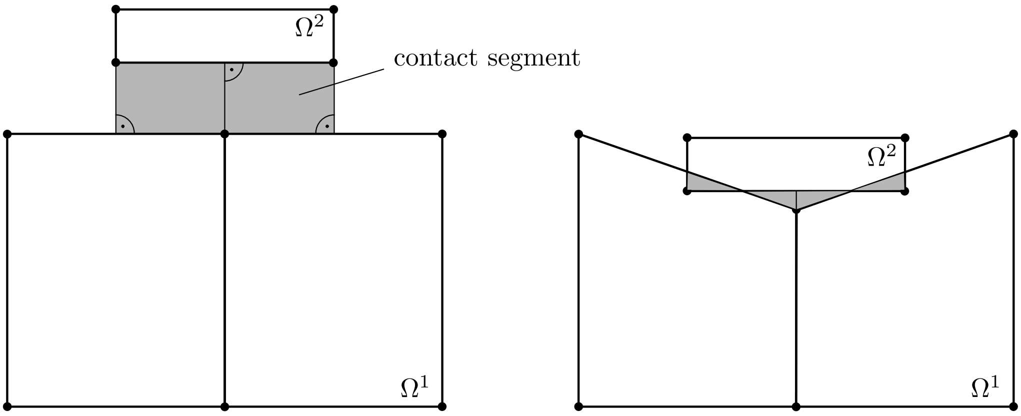

Figure 3.9: Segment-to-segment approach: The gray segments illustrate the contact segments. In the case of contact (right figure), the non-penetration condition is only fulfilled in an integral sense. The right figure is therefore giving a geometrical interpretation of the average gap [88].

the Lagrange multiplier method can be applied, even though the Lagrangian method is being mostly used. The method was introduced by Bernardi, Debit, and Maday in [7] and further developed in [8] and [9]. Detailed mathematical investigations showed that the continuity condition's integral enforcement did lead to better results than their exact fulfillment on discrete nodes. By enforcing the contact constraints not pointwise but in an integral sense, as done in the STS and mortar method, jumps in the contact forces will be smoothed. This is why the mortar method is well adopted in the low order Finite Element community where the bodies' geometric description is usually approximated by linear or quadratic polynomials. Further details on the mortar method are for example given in [31, 54, 86, 88].

Lately, studies are carried out which apply the isogeometric analysis concept introduced by Hughes [46] to contact mechanics, see [14], [55] and [84]. The use of isogeometric ansatz spaces enables a smooth geometric representation of the contact boundary combined with the ability to control the continuity on individual points. De Lorenzis [14] and Temizer [84] combine the isogeometric concept with the mortar method to introduce the contact constraints.

All of the aforementioned methods make use of the master-slave, respective mortar side and non-mortar side, concept. The constraints are usually only enforced at the slave nodes or surfaces and then transferred onto the master boundary. Especially for the NTS method, the nodes on the master side generally do not satisfy the Kuhn-Tucker condition given in equations 3.8-3.11. The reason for this is the *poor* geometric description mostly used in combination with low order Finite Element Methods. It is simply not possible to enforce the Kuhn-Tucker conditions on the master and slave side at the same time when curved shapes are considered (see Figure 3.7).

Representing the geometry exactly by making use of the blending function method as described in Section 2.2.4, enables to enforce the contact constraints on both contacting boundaries simultaneously when higher order basis functions are used to describe the objects' displacements. But in order to obtain good results it is insufficient to simply check for penetration of the elements at the corner nodes. Since p-version meshes are usually very coarse, the test for penetration is rather performed along the contact interface on the level of quadrature points, namely Gauss-Legendre points. An important property of the Gauss-Legendre points is that the points live on the interval of $-1 < x_i < +1$, with x_i being the Gaussian node's position. From this it is clear that the corner nodes of the elements do not enter the quadrature and the normal direction on each Gauss point is uniquely defined. In contrast to this, the interval of the Gauss-Lobatto points $-1 \leq x_i \leq +1$, includes the boundaries of the interval -1 and $+1$, which leads due to the FEM's C^0 continuity on the nodes to ambiguous normal directions on Finite Element nodes (see Figure 3.10). Thus the use of Gauss-Legendre nodes is recommended for the evaluation of the gap function. It can generally be stated, that a high-order of quadrature points on both contact boundaries is superior to a low number, especially when curved geometries are considered. It is theoretically possible to use various solution algorithms for contact in combination with this approach like the penalty, Lagrange, augmented Lagrange or other methods, although only the penalty method is studied in this work. Due to the fact that the contact detection is performed sequentially on each contact boundary, non matching meshes can be used in the contact interface. Nevertheless special treatment of the end points of the contact interface is necessary in order to improve the results. Further discussion of this issue will be given in Chapter 4. In the following paragraph the local contact search algorithm will be explained for the bilateral case as suggested by Gabriel [28].

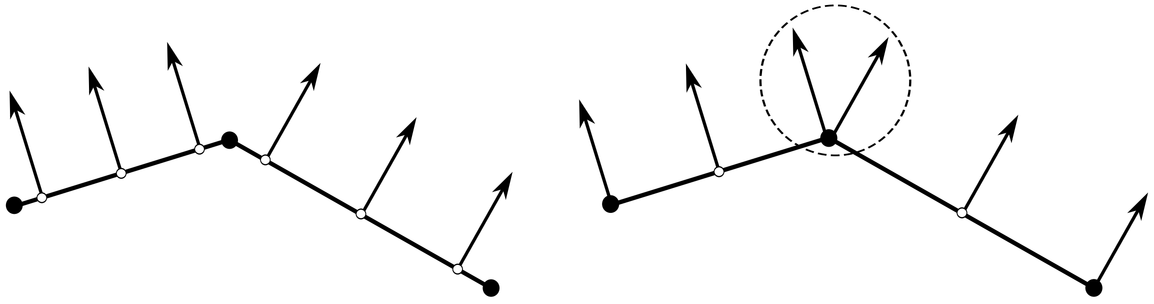

Gauss-Legendre nodes Gauss-Lobatto nodes

Figure 3.10: Ambiguity of normal on Gauss-Lobatto nodes and unique normal on Gauss-Legendre nodes.

Local Contact Search for High-Order Finite Element Methods

Disregarding the discretization method described in the previous section, the contact has to be detected by evaluating the gap function for individual points. Focusing on the high order scheme with continuous and smooth boundary descriptions, the corresponding contact search can be performed on the Gauss-Legendre points as stated before. For this case, the contact boundary of two contacting objects is displayed in Figure 3.11, where Γ_c^1 and Γ_c^2 denote the deformed boundaries of objects Ω^1 and Ω^2, respectively. Points $\mathbf{x}^1$ and $\mathbf{x}^2$ in their deformed configuration are located on the deformed boundaries as shown in Equation 3.6. Taking the point $\mathbf{x}^1$ as a generic point on Γ_c^1, it is evident that there are two different points ($\mathbf{x}^2$ and $\overline{\mathbf{x}^2}$) on Γ_c^2 whose potential contact partner is $\mathbf{x}^1$. The projection of $\mathbf{x}^1$ on Γ_c^2 yields $\mathbf{x}^2$ and the projection of $\overline{\mathbf{x}^2}$ on Γ_c^1 yields $\mathbf{x}^1$. Thus the definition of an algorithmic contact pair for $\mathbf{x}^1$ is not unique, leading to two different possible contact pairs for $\mathbf{x}^1 : \{\mathbf{x}^1, \mathbf{x}^2\}$ and $\left\{\mathbf{x}^1, \overline{\mathbf{x}^2}\right\}$. The corresponding oriented distances $\mathbf{d}^{12}$ and $\mathbf{d}^{21}$ are:

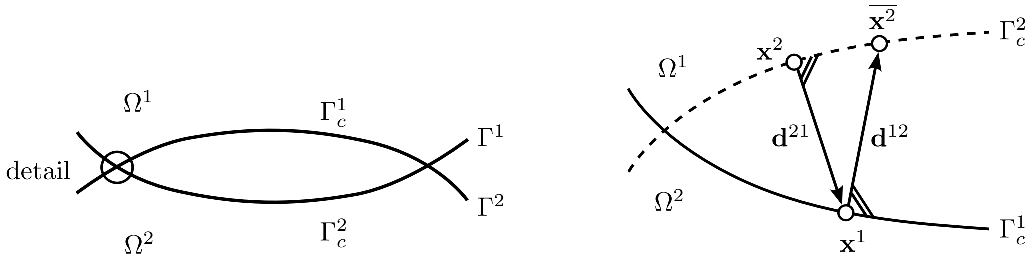

Figure 3.11: Ambiguous normal directions and gaps depending on the generic point.

$$\begin{aligned} \mathbf{d}^{12} &= \overline{\mathbf{x}^2} - \mathbf{x}^1 && (3.25) \\ & && (3.26) \\ \mathbf{d}^{21} &= \mathbf{x}^1 - \mathbf{x}^2 && (3.27) \end{aligned}$$

It follows that $\mathbf{d}^{12} \perp \Gamma_c^1$ and $\mathbf{d}^{21} \perp \Gamma_c^2$, but $\mathbf{d}^{12} \neq \mathbf{d}^{21}$ for the general case. If $\mathbf{d}^{12}$ and $\mathbf{d}^{21}$ are not equal, the corresponding pressures will also differ for point $\mathbf{x}^1$, depending on whether $\mathbf{x}^1$ is projected onto Γ_c^2 or $\overline{\mathbf{x}^2}$ is projected onto Γ_c^1. Therefore Newton's action-reaction principle is not satisfied a priori. Yet, in the case of convergence of the overall solution, Γ_c^1 and Γ_c^2 and hence $\mathbf{d}^{12}$ and $\mathbf{d}^{21}$ will become parallel to each other (as plotted in Figure 3.12), resulting in

$\mathbf{x}^2 = \overline{\mathbf{x}^2}$ and $\mathbf{d}^{12} = \mathbf{d}^{21}$. In order to satisfy Newton's action-reaction principle, it is necessary, in contrast to the classical master-slave concept [88], to evaluate the gap function for each Gaussian node on each contacting edge separately, so that no contact boundary is given preference. This leads to a symmetric treatment.

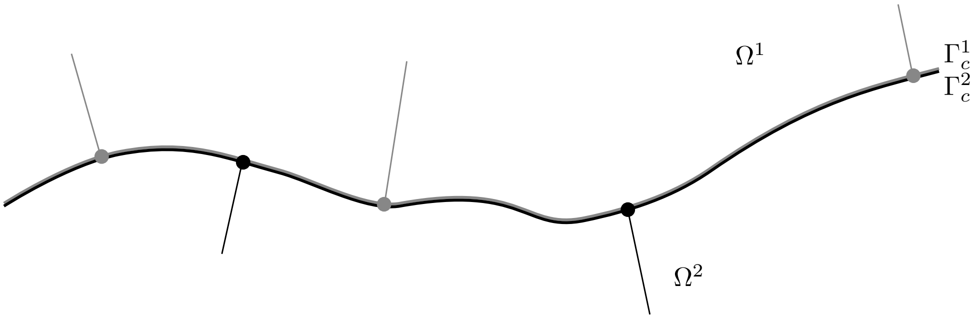

Figure 3.12: Discretization using the blending function method in combination with high order basis functions.

From a theoretical point of view the local contact search itself is relatively easy. The normal vector on arbitrary (Gaussian) points can be derived from the tangent $\mathbf{t}^{\gamma}_{GP}$ of this point on the deformed boundary. The normal vector $\mathbf{n}^{\gamma}_{GP}$ hast to fulfill the following condition:

$$\mathbf{t}^{\gamma}_{GP} \perp \mathbf{n}^{\gamma}_{GP} \quad \rightarrow \quad \mathbf{t}^{\gamma}_{GP} \cdot \mathbf{n}^{\gamma}_{GP} = \mathbf{0} \tag{3.28}$$

To detect contact, the intersection of the normal (ray) and a deformed element boundary of the other domain has to be checked. For isoparametric linear element descriptions this is easily derived in a closed form analytically. For arbitrary representations of the boundary like for a combination of the initially exact geometry representation (blending function method) and a deformation derived from high order polynomials, the intersection test is numerically more demanding. In the present work it is performed by a numeric algorithm that iteratively finds the intersection point between a ray and an arbitrary curve. A good overview of algorithms in two and three dimensions can be found in [68].

Usually the Gauss order changes with the chosen polynomial degree p. In order to have an exact integration of the load vector and stiffness matrix, a Gauss order of $p + 1$ has to be chosen. This scheme is also applied in the present study, but a very precise integration scheme with a Gaussian order as high as fifty is chosen along each edge for the contact detection. At a first glance it would seem reasonable to use different Gaussian orders for different polynomial degrees. Yet, with varying numbers of Gauss points their individual local positions along the edge vary as well. Whereas this might not be important for elements lying completely in the contact region, it can be of crucial relevance for elements which are only partly in contact. For these elements it is even possible to obtain better results with a lower Gauss order, just because the position of the Gauss points is fortunate. By choosing a constant value of fifty along the boundaries for the contact detection, an influence of the individual Gauss point position for changing polynomial orders $(p + 1)$ can be excluded.

3.7 Linearization of Contact Contributions

The linearization of the contact contributions is usually performed analytically for polynomial degrees of low order. Higher order linearizations of the contact terms are difficult to derive and are not in the scope of this work. A possible method is described in Konyukhov et al. [52]. In the present study, a finite difference scheme is applied to derive the approximate tangent stiffness matrix.

Finite Difference Method

The derivative of a function $a(x)$ in x-direction is approximated by the first order forward finite difference formulation as:

$$a(x)_x^{foward} = \frac{a(x+\Delta x) - a(x)}{\Delta x} \tag{3.29}$$

where the disturbance term Δx is small but finite. A detailed introduction into finite difference schemes can be found in Hirsch [43]. Further schemes are the first order backward difference method (Equation 3.30) and the second order central difference method (Equation 3.31)

$$a(x)_x^{backward} = \frac{a(x) - a(x-\Delta x)}{\Delta x} \tag{3.30}$$

$$a(x)_x^{central} = \frac{a(x+\frac{\Delta x}{2}) - a(x-\frac{\Delta x}{2})}{\Delta x} \tag{3.31}$$

Following Wriggers [87], the forward difference method can be used to approximate the tangent stiffness matrix $\mathbf{K}$. When the Newton Raphson method [87] is applied in combination with the forward difference method, the *discrete Newton Raphson method* is derived. It uses the residual of the equation system, which is derived from Equation 2.45.

$$\mathbf{G} = \mathbf{F} - \mathbf{K} \cdot \mathbf{U} \tag{3.32}$$

To approximate the m^{th}-column $\mathbf{k}_m$ of the tangent stiffness matrix $\mathbf{K}$ with N unknowns, the following scheme can be used:

$$\mathbf{k}_m \approx \frac{1}{h_m}\left[\mathbf{G}(u_i + h_m\,\mathbf{e}_m, \lambda) - \mathbf{G}(u_i, \lambda)\right] \tag{3.33}$$

$$\text{with} \quad \mathbf{K} = [\mathbf{k}_1\ \mathbf{k}_2\ \mathbf{k}_3\ \cdots\ \mathbf{k}_m\ \cdots\ \mathbf{k}_N]\,. \tag{3.34}$$

The method is therefore depending on the residual $\mathbf{G}$, the step size h_m, the load factor λ, and the m^{th} unit vector $\mathbf{e}_m$ which is zero everywhere except at index m where it takes the value of one. In order to obtain a good approximation for $\mathbf{k}_m$, h_m should be chosen very small. Unfortunately the value of h_m is bounded by the computer's machine accuracy η. An estimate for the value of h_m can be derived by

$$h_m = \nu\left(|(u_m)| + 10^{-3}\right) \qquad \text{with} \quad \nu = 10^{-3}\ldots 10^{-5} < \sqrt{\eta}\,. \tag{3.35}$$

Applying the discrete Newton Raphson scheme with the forward difference scheme as given above, the tangent stiffness matrix $\mathbf{K}$ for contact problems can be derived. Due to the fact that the forward difference method only takes points on one side of the point of interest (x) into consideration, it is called a one-sided-difference formula. This property is in fact not well suited for contact problems, because of the inequality condition in the contact constraints. When calculating the derivative and hence the stiffness matrix it makes a big difference in which direction the disturbance is applied. If it is applied in such a way that the disturbed object comes in contact, a large increase of the individual stiffness term is expected. If the disturbance is applied in the opposite direction, away from the other contacting object, no change in the stiffness term will occur. It is therefore not possible (or only with additional effort) to derive a symmetric stiffness matrix by applying the forward, or backward finite difference scheme. From this it follows that the central difference method is due to its symmetric formulation the method which is (out of the three methods) best suited to capture the contact and derive a symmetric stiffness matrix. It is therefore used in the present work. The symmetric equation system[3] to derive the tangent stiffness matrix for the problem of contact mechanics, is therefore derived as:

$$\mathbf{k}_m \approx \frac{1}{h_m}\left[\mathbf{G}(u_i + \frac{h_m}{2}\,\mathbf{e}_m, \lambda) - \mathbf{G}(u_i - \frac{h_m}{2}\,\mathbf{e}_m, \lambda)\right] \, . \tag{3.36}$$

The mayor drawback of the applied method is the enormous computational effort that has to be spend to evaluate the residuum $\mathbf{G}$ for each disturbed solution vector $\mathbf{u}$. Each disturbance requires to check for contact and evaluate the gap function again. For an equation system with N unknown displacements, the residuum vector $\mathbf{G}$ has to be evaluated N times. In each evaluation, the check for contact has to be performed twice, because of the application of the central difference method. The whole computation time is therefore ruled by the derivation of the tangent stiffness matrix. A possible alternative to the method applied here is given by Konyukhov et al [52]. It defines the weak form of the contact in a local coordinate system living on the contact boundary. With this covariant form, the linearization of the contact term, even for large displacements and high-order ansatz spaces can be derived.

---

[3] It should be noted, that the normal direction on the disturbed position of each Gauss point should not be recomputed while computing the tangent stiffness matrix numerically. Instead the normal direction on each Gauss point in the undisturbed configuration has to be used to evaluate the gap function (Equation 3.7) in the disturbed configuration. That way a symmetric matrix system can be derived, even for the described case, where the stiffness matrix is computed by separate contact search runs along each objects' contact boundary.

Chapter 4

FE Extensions - Adaptive Mesh Methods

Important tasks in engineering practice are to develop, analyze, and plan for example economical and ecological impacts, consumer products, estimate processes and risks, and design rural and urban infrastructure. For each application and task the engineer is working with and generating simplified models to approximate the real world. The limits of these models have to be known and understood by engineers in order to obtain estimates which are sound and of such quality that decisions based on them are essentially the same as if the correct solution is known a priori. Applying this to mechanical problems solved with the Finite Element Method, we have to be sure that the approximation that we get for our solution vector u_{FE} is in a range which is acceptable for the problem at hand. As an optimum, the solution of the Finite Element Method is almost as good as the exact solution u_{ex}. In order to achieve this it is obvious that we need to take care of our problem's discretization, where discretization is meant to cover the whole range from linear and non-linear theories, material laws, meshes, ansatz spaces etc. A measure for the quality of the discretization can be a convergence of stresses, strains, displacements, reactions, strain energy, et cetera. To check their convergence, modifications of the FEM can be used, where *modification* stands for a process that systematically changes the FE discretization by means of an increase of degrees of freedom, or mesh adaption. With these progressively improving approximation properties, better solutions can be obtained and evaluated by means of convergence to an estimated exact solution. Before talking more about the extension strategies, a classification of error estimators and further criteria for the decision making should be discussed first.

4.1 Problem Classification

In order to distinguish between different problem types of partial differential equations, it is useful to establish a simple classification for the character of the exact solution u_{ex}, based on a priori informations about the problem's regularity. Further details about the classification can be found in [80, 81].

Category A: The nature of a problem of category A is that its solution u_{ex} is analytic everywhere in the solution domain, including the boundaries. A function is said to be analytic in a point when it can be expressed using a Taylor series expansion about that point.

Category B: A problem of category B has the nature that u_{ex} is analytic everywhere inside the solution domain, including the boundaries, but with the exception of a finite number of points. These finite number of points are called *singular points* which is due to the fact, that the solution is not analytic, but singular at these points. The position of the singular points is known a priori such that the Finite Element mesh can be constructed in a way that the singular points coincide with the Finite Element nodes. For 3D cases additional singular edges can occur. In between the singular points and edges, the solution is analytic.

Category C: Category C contains all problem types where u_{ex} can not be expressed by category A, nor category B. Singularities occur inside the solution domain or on the boundaries. Their position is not known a priori. Thus a FE mesh can not be constructed in a way that the points where the solution is not analytic are nodal points (or edges in 3D).

Alternating boundary conditions generally lead at least to a reduced regularity at the transition from for example a fixed support to a free boundary. A similar loss of regularity can be observed in the interface from boundaries with distributed loads to the free boundary conditions. These problems are therefore of category B, because the location of the points where the solution is not analytic is known a priori. In a similar way, contact mechanics can be understood as a problem with changing boundary conditions in each iteration step [87]. At the a priori not known location of the end of the contact interface, the boundary condition changes from contact (load boundary condition) to a free boundary condition. The nature of contact mechanics therefore is a problem of category C. The aim of adaptive mesh methods is to turn a problem of category C into a problem of category B. A posteriori error estimators (see following section) are used to modify the mesh in such a way that non analytic (singular) points either coincide with FE nodes (*rp*-version of the FEM) or are isolated by a single small element (*hp*-version of the FEM). Details on error estimators and the different adaptive schemes are given in the following sections. Due to the analogy of the contact problem to a Neumann boundary condition, studies will first show the convergence rates of the Neumann boundary condition (Section 4.5) before the results for the contact examples will be given in Chapter 5.

4.2 Error Estimation and Convergence Rates

During the last twenty years numerous authors have been working on the topic of error estimation. Several strategies have been developed in order to estimate the error which occurs in Finite Element approximations. For a detailed discussion the reader is referred to the work of [1], [85], and [87]. As a first and most obvious classification of error estimates, the following description is given which is based on the input data used.

a priori: These error estimates are available for many problems of category A, B, and C. They are not based on results obtained during the Finite Element computation itself, but based on an a priori analysis of the structure of the exact solution (like its smoothness). The structure depends on boundary conditions and the geometric layout of the problem for example. The a priori analysis enables to choose the right approximation method, discretization scheme, mesh layout, and estimates the possible convergence rates. Depending on the problem's category and chosen discretization, possible convergence rates can be of algebraic, or exponential nature (see Figure 4.1). A detailed survey can be found in [4, 71, 81].

a posteriori: These error estimates are also available for many problems of category A, B, and C. They make use of the data computed by the Finite Element Method. In a postprocessing routine, it estimates the error's distribution and magnitude. This qualifies it to be used for adaptive schemes, by judging which scheme should be used and how and where the adaptivity should be applied. Possible methods include global or local mesh refinements, global or local adaption of the shape functions' polynomial degree, and mesh relocation. Out of the large variety of a posteriori error estimators a few like explicit, implicit, residual based, and hierarchy based estimators should be named.

In the motivation of Chapter 2 several different error sources were mentioned. In order to measure the error $\mathbf{e}$ of a Finite Element approximation $\mathbf{u}_{FE}$,

$$\mathbf{e} = \mathbf{u}_{ex} - \mathbf{u}_{FE} \tag{4.1}$$

the strain energy of a solution as defined in Equation 2.31 can be used

$$\|\mathbf{u}\|_{E(\Omega)} \;=\; \sqrt{\mathcal{U}(\mathbf{u})} = \sqrt{\frac{1}{2}\,\mathcal{B}(\mathbf{u},\mathbf{u})}\ .$$

Besides others, the strain energy is a good measure for the quality of a solution (if the exact solution $\mathbf{u}_{ex}$ is known), because it generally covers the whole domain of the computation and can be computed for every problem without a priori knowledge of the solution's properties. The error in strain energy norm, as a measure for the quality of the approximation, is:

$$\|\mathbf{e}\|^2_{E(\Omega)} \;=\; \|\mathbf{u}_{ex} - \mathbf{u}_{FE}\|^2_{E(\Omega)}\ . \tag{4.2}$$

The relative error in strain energy norm η which is used in the convergence plots in the following Chapters and Sections is computed as:

$$\eta = \sqrt{\frac{|\mathcal{U}_{\mathrm{ref}} - \mathcal{U}_{\mathrm{FE}}|}{\mathcal{U}_{\mathrm{ref}}}} \cdot 100\,[\%]\ . \tag{4.3}$$

In general one distinguishes between different ratios of convergence for the various error types such as i.e. the error in energy norm. To judge the error's behavior, the relative error in energy norm is usually plotted in a double logarithmic scale where η is considered to be a function of the number of unknowns *log N*. In Figure 4.1, some fundamental convergence rates, reaching from algebraic to exponential, are sketched. In the conventional h-version of the Finite Element Method, global or local mesh refinement is used in order to improve the quality of the solution. The optimal rate of convergence for the relative error in energy norm (Equation 4.3) for the h-refinement is algebraic. The value of the negative gradient of the convergence rate β (plotted in Figure 4.1), is a function of the applied polynomial degree of

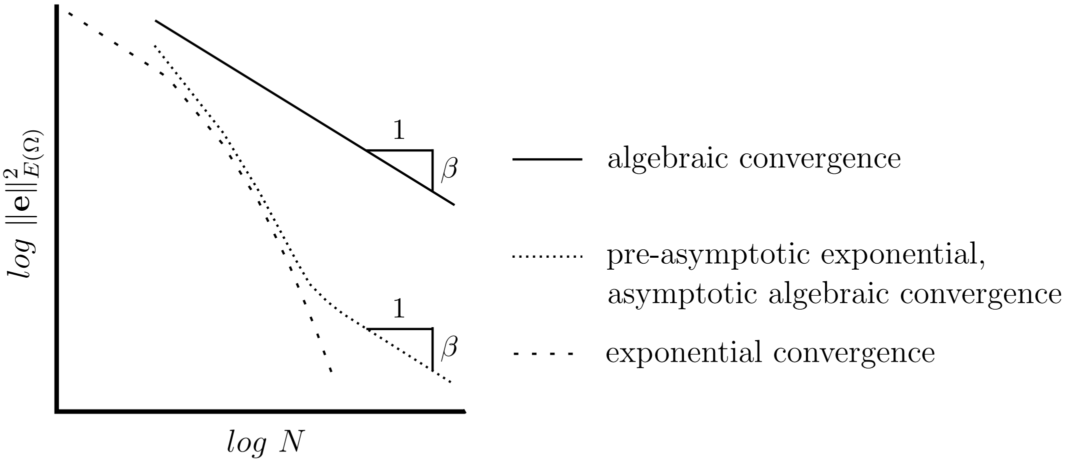

Figure 4.1: Overview of convergence rates in energy norm for a two dimensional problems.

the shape functions and has a value of $\beta = \frac{1}{2}p$ for two dimensional problems in linear elasticity. For a bilinear ansatz space, β takes the maximum value of 0.5 and for a biquadratic ansatz ($p = 2$) the gradient for β is ≤ 1. The given gradient is only defining the upper bound, but can vary according to the smoothness of the solution. The error $\|\mathbf{e}\|_{E(\Omega)}$ for algebraic convergence behavior is generally given by:

$$\|\mathbf{e}\|_{E(\Omega)} \leq \frac{k}{N^{\beta}} \tag{4.4}$$

with k being a constant, and N being the number of degrees of freedom.
For the p-version of the FEM as presented in Section 2.2.3, the mesh remains the same, but the polynomial degree of the applied ansatz function is increased. Exponential rates of convergence of the error in strain energy norm are possible for smooth problem types of category A. For problems of category B or C, containing singularities like reentrant corners or nonlinearities, like elasto-plasticity, or contact, the convergence rate is at least in the asymptotic range only of algebraic type if the general p-version of the FEM is used. Nevertheless it is still superior to the convergence rate of the h-version for problems of category B or C. The gradient is depending on the smoothness of the solution. In order to improve the convergence rate for these problem classes, enhanced Finite Element Methods like for example the hp-, rp-, or $hp-d$-method [18, 58] should be used. In the following it will be shown, that even for contact problems, exponential rates of convergence of the error in energy norm are possible if the p-version of the FEM in combination with adaptive methods is used. The error $\|\mathbf{e}\|_{E(\Omega)}$ for exponential convergence behavior is generally given by:

$$\|\mathbf{e}\|_{E(\Omega)} \leq \frac{k}{\exp\left(\gamma N^{\theta}\right)} \tag{4.5}$$

where γ and θ denote another constant with $\theta \geq 0.5$ [81].

4.3 Stress Intensity Factors

The stress intensity is an indicator for the evaluation of the smoothness, meaning continuity and differentiability of the problem at hand. With its help the identification of singular points inside the solution domain is possible. A short introduction into the topic is given in the following.

From a mathematical point of view, the exact solution for two-dimensional problems of linear elasticity can be written as a sum of two functions u_1 and u_2. Of these, u_1 is a smooth function and the function u_2 exists in the neighborhood of a finite number (m) of points P_i. The function u_1 is neglected in the following discussion and we will focus on function u_2:

$$u_2 = \sum_{i=1}^{\infty} A_i \cdot r^{\lambda_i} \cdot \psi(\theta_i) \tag{4.6}$$

The polar coordinates r and θ_i are centered on the singular points P_i. The coefficient A_i symbolizes the stress intensity factors. The exponent λ_i characterizes the smoothness of the solution and $\psi(\theta_i)$ are smooth functions [81].

The stress intensity factors A_i depend on material parameters, the loading, and in particular on the position of P_i. As indicators for the smoothness (continuity and differentiability) of the solution at P_i, the stress intensity factors A_i can be derived by an asymptotic expansion around P_i [21].

The lowest λ, corresponding to the term with a non-zero coefficient, governs the asymptotic rate of convergence. The size of A_i influences the pre-asymptotic behavior. Suppose $A_1 = 0$, A_2 is small in comparison with A_3. Then in the pre-asymptotic range the rate of convergence would be dominated by λ_3 but in the asymptotic range it would slow down to the rate corresponding to λ_2 [82].

4.4 Stress Intensity Factors for Contact Problems

Kinderlehrer [51] and Schumann [70] studied the regularity for Signorini's contact problem [50] in linear elasticity, where the Signorini problem is a generalization of the unilateral Hertzian 2D problem. In particular they studied the regularity of the solution at the end of the contact interface. They showed, that the solution of the Signorini problem belongs to the Hölder space $C^{1+\alpha}$ with $0 < \alpha \leq 1$. In this C^1 means that the function is one times continuously differentiable and $C^{1+\alpha}$ says that the first derivative satisfies the Hölder condition with index α [38]. For $\alpha = 1$, the first derivative is therefore Lipschitz continuous. For $\alpha = 0$, the first derivative is bounded. It can thus be summarized that the unilateral contact problem of Signorini type is not more than C^2 continuous.

This property is as well studied in the *obstacle problem* (Figure 4.2). It describes the behavior of a membrane which comes in contact with a rigid obstacle. Having two functions where $u(x)$ defines the membrane (boundary Γ_u) and $g(x)$ defines the boundary (boundary Γ_o) of the obstacle, one has to divide the solution domain Ω into two sub-domains D_1 and D_2. Domain D_1 is the area, where the differential equation for the general linear elasticity holds. Its complement D_2 is the contact interface where, additional to the linear elasticity, the solution u touches the obstacle with $u(x) = g(x)$. The so called *contact interface point* marks the end points of the contact interface where $\Gamma_* := \partial D_1 \cap \partial \overline{D}_2$. These points are generally not known a priori. The solution's regularity at this point is such that it is not more than H^2 regular,

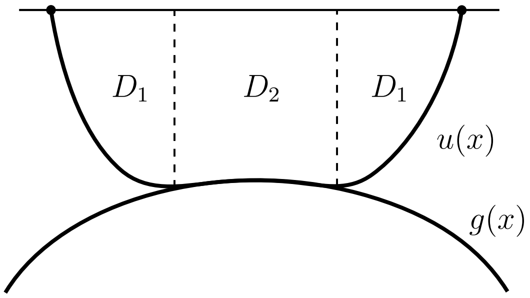

Figure 4.2: Setup of the obstacle problem - a membrane described by $u(x)$ in contact with a rigid obstacle whose surface is given by $g(x)$.

where H defines the *Sobolev space.* It can then be said that

$$u|_{\Gamma_*} = g|_{\Gamma_*} \quad \text{and} \tag{4.7}$$

$$\left.\frac{\partial u}{\partial x}\right|_{\Gamma_*} = \left.\frac{\partial g}{\partial x}\right|_{\Gamma_*} \tag{4.8}$$

which states that u and g are identical on Γ_*. Furthermore, the solution is continuous and possesses Lipschitz continuous (bounded by some finite value) first derivatives which is also identical in Γ_*. In addition, the solution is generally discontinuous in the second derivatives across Γ_*. For further informations on this topic the reader is referred to the book of Großmann and Roos [36], and Schröder [69].

Eck [21] studied the asymptotic expansion for the Signorini type problem and showed that the first term of the stress intensity factor vanishes in Γ_*. Unfortunately, the higher order terms do not vanish at the end of the contact interface as desired, thus introducing a reduced regularity at this point. Following this study, the rate of convergence for a general p-version of the FEM is therefore limited to be of algebraic type.

Another way to explain and understand the behavior of a Signorini type problem is to analyze the effect of the boundary condition arising from the contact side constraints. As shown in Section 4.1, the mechanical contact problem can be understood as a problem with changing boundary conditions in every iteration step. Assuming that the distribution of the contact stresses in the contact interface is known for every iteration step, it would from a theoretical point of view not make any difference if the contact problem is computed, or if an equivalent system of separate objects is computed where the known contact loads are applied in every iteration step. The contact boundary conditions can therefore be seen as a boundary condition of Neumann type, by applying distributed loads (stresses) along the boundary. In general it is well known that loads have to be applied carefully on a given domain in order to avoid singularities or at least avoid points with reduced regularity. Some aspects of Neumann boundary conditions are discussed in the following section.

4.5 Neumann boundary conditions

From an engineering and mathematical point of view it is well understood that concentrated point loads applied on a given domain lead to a singularity in the stresses at the application point. As the stresses are equivalent to the applied load per area it is clear, that the stresses become infinite when the affiliated element size (area) is decreased to zero in the limit point. But also distributed loads can reduce the regularity of a solution, depending on the object's geometry and whether the load is applied on finite area only (inhomogeneous boundary conditions). For example a jump in the stresses is generally introduced at the end of a rectangular distributed load acting normal to the boundary[1]. This jump in the stress distribution is not a problem for the convergence of the Newton algorithm during the computation, as it matches the C^0 continuity requirement of the FEM at Finite Element nodes, but it is certainly a point with reduced regularity in the solution domain (not part of problem category A). Some possible problematic setups are shown in Figure 4.3(a), (b), and (c). They show a reduced regularity at the end of the area where the load is applied. If this area is discretized with Finite Elements, attention has to be drawn to the chosen element size around this point. The error introduced is related to this element size as it frames the affected area and thus how far the error spreads. The solution will finally always be governed by this error. In the pre-asymptotic range, exponential rates of convergence can possibly be obtained for the p-version of the Finite Element Method. As long as the overall error in the solution domain is larger than the error introduced due to the singularity at the end of the load application area, the rate of convergence is of exponential nature (pre-asymptotic convergence rate). As soon as the solution in the domain is represented well by the applied high order shape functions, the singularity due to the loading will govern the convergence rate, leading to asymptotic algebraic rates of convergence. When an adaptive scheme like the hp-method is used, exponential rates of convergence are to be expected as the influence area for the error is reduced in each adaptive step (see Section 4.7).

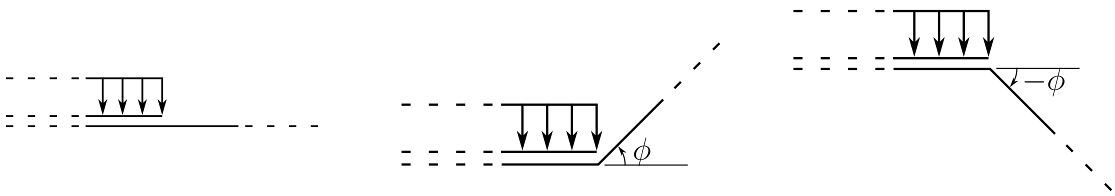

(a) (b) (c)

Figure 4.3: Rectangular load on different settings, causing solutions with reduced regularity.

For triangular loads, two problematic areas can occur. The end with high loading, will exhibit the same loss of regularity as described for the rectangular load. Assuming a proper treatment of this side and focusing on the end where the load approaches zero, a reduced regularity can be observed as well, leading to a similar convergence behavior, but with a higher rate. As for the rectangular load distributions, some setups are shown in Figure 4.4(a), (b), and (c) that lead to a reduced regularity at the end of the line (area) load.

As a simple test case, a model consisting of two elements is chosen to show the convergence characteristic for different Neumann boundary conditions acting on parts of a boundary. The distribution of the load is either rectangular or triangular. The loads are applied separately giving two different load cases. The material of the block is steel with a Young's modulus

---

[1] This does not cause a problem if the neighboring, unloaded edge is attached within an angle of exactly $\phi \pm 90$ degrees. Further studies should be performed to test the sensitivity of the enclosed angle of the neighboring edge to the amount of reduced regularity in the solution. An article dealing with these types of inhomogeneous boundary conditions and their resulting stress singularities in elasticity and asymptotic analysis is given by Sinclair [75].

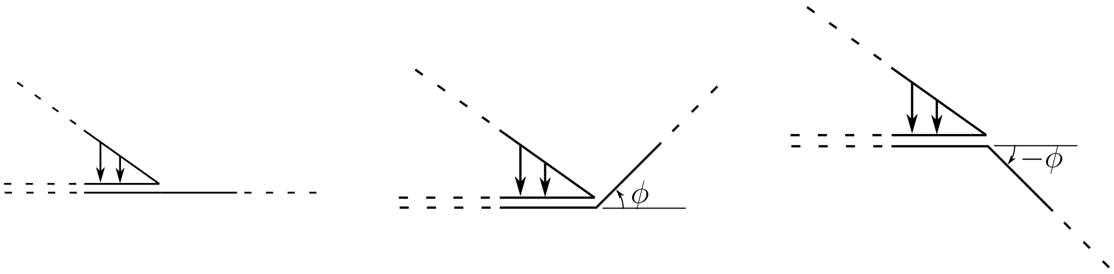

(a) (b) (c)

Figure 4.4: Triangular load on different settings, causing solutions with reduced regularity.

of 206900 $[N/mm^2]$ and a Poisson ration of 0.29. Small displacements are assumed and the polynomial degree is varied between three and twenty. The system for the numerical setup is shown in Figure 4.5. The reference solution for the computation of the relative error in energy norm is computed on a uniformly refined mesh with a refinement factor of ten, resulting in a mesh with 200 elements, computed with a polynomial degree of ten. The relative error in energy norm is plotted in Figure 4.6 for the two load cases. A pure algebraic rate of convergence is visible for both load cases, with a higher convergence rate for the triangular load. The algebraic rate of convergence is a consequence of the singularity occurring at the end of the load application area. Figure 4.7 shows the relative error of the von Mises stresses for the two different load patterns. The error in the domain is derived by showing the difference between the computation with two elements and $p = 20$ and the computation with two elements and $p = 10$. The model with two elements and $p = 20$ is therefore taken as a reference instead of the 200 element mesh. This is done because the error in the von Mises stresses are much easier derived from discretizations having the same meshes. But as it is shown in Figure 4.6, the solution of the two element mesh and $p = 20$ is also showing small errors in the energy norm for the rectangular and triangular load case.

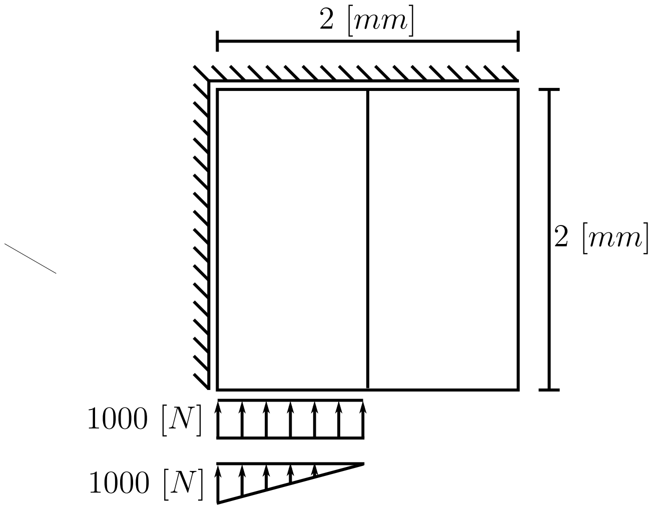

Figure 4.5: Simple test case of a rectangular block discretized by two elements, loaded by two different load cases (rectangular and triangular).

In Figure 4.7, the scaling in the legend gives the span from zero error to a relative error of 0.5%.

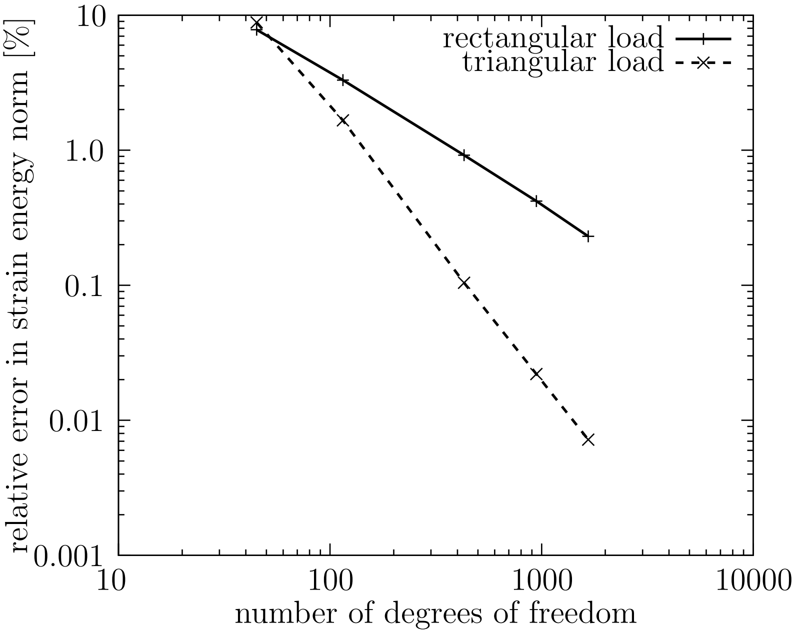

Figure 4.6: Convergence rate of the relative error in energy norm for the simple test case of a block discretized with two elements. The polynomial degree is varied between $p = 3$ and $p = 20$. A rectangular and triangular load case is studied.

The relative error of 0.5% means that the maximum value in this plot shows the area where the error is larger than 0.5% of the maximal von Mises stress occurring for this load. More interesting than the quantitative evaluation of this Figure is the qualitative information that it contains. It can well be seen that the system loaded with the rectangular load (Figure 4.7(a)) is experiencing larger oscillations than the system loaded with the triangular load (Figure 4.7(b)). This is due to the sudden change in the boundary condition occurring at the end of the rectangular load distribution. A jump in the stresses in vertical direction is induced at the end of the element by this load pattern. For the triangular load case, a reduced regularity in

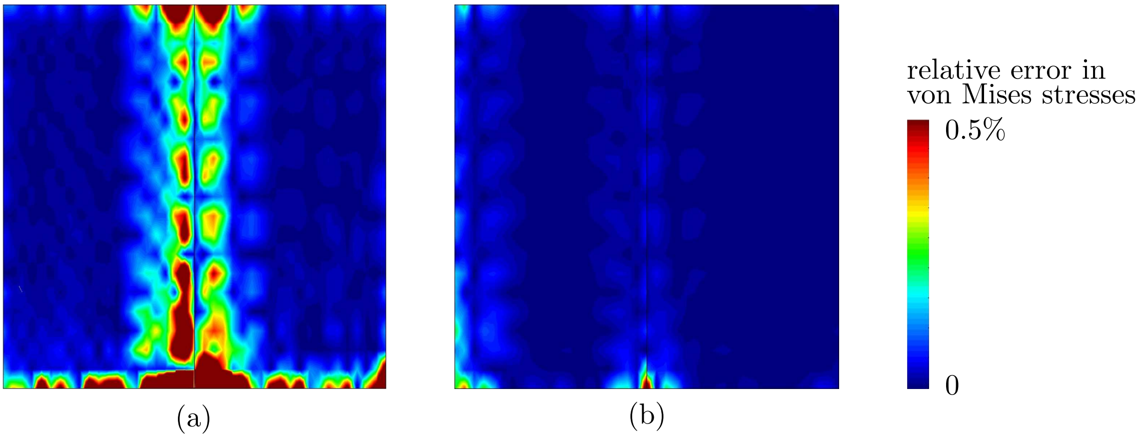

(a) (b)

Figure 4.7: Relative error in von Mises stresses for the two element example with different load cases given in Figure 4.5. High discontinuities are visible at the end of the applied load for the rectangular load case (a) and the triangular load case (b).

the stresses in y-direction is existing at the end of the load application area (where the value of the load is zero) and in the axis of symmetry. When picturing the full model (twice as wide), a kink in the load is also present at the axis of symmetry, leading to another reduced regularity there.

Due to the simple test case, the convergence rate (Figure 4.6) is even algebraic in the pre-asymptotic range as the displacement distribution inside the domain is basically linear. The deformation can therefore already be represented well with the ansatz space of $p = 1$. In this case, higher polynomial spaces do not improve the solution significantly in the interior domain, but only around the singularities. The convergence rate is therefore bounded by the regularity which occurs at the end of the distributed load and thus of algebraic type. For more complex geometries with more complex solutions for the displacement, an exponential rate of convergence would be visible in the pre-asymptotic range, but the asymptotic convergence behavior will always be of algebraic type due to the singularities at the end of the Neumann boundary condition[2].

To demonstrate this, further tests are performed on a different geometry to broaden the understanding of the effects of different load patterns. The studied example is a plate with a hole, loaded by five different loads. The plate's material is steel with a Hookean material having a Young's modulus of 200000 $[N/mm^2]$, computed with small displacements as a plane strain problem. The loads are applied in such a way that it starts and ends exactly with a Finite Element node, as in the previous example. The system, including the mesh with eight elements is shown in Figure 4.8 for each load case. The integral of each distributed load is kept constant and the material parameters and dimensions are chosen identical for each load case. The tested load cases are a constant rectangular load, a triangular load, a quadratic B-Spline load distribution (only one segment) with zero gradient where the load approaches zero, a quadratic B-Spline distribution with zero gradient on both ends of the load distribution (Equation 4.9), and a load distribution in the shape of a Hermite polynomial given in Equation 4.10. The B-Spline load distribution with the zero gradient on one side is built from the right section of a quadratic B-Spline and given as $1/2 \cdot (1-t)^2$. The B-Spline has a zero gradient on both sides and is composed from two piecewise quadratic B-Spline functions, with a C^1 continuity at their interface.

$$p = \begin{cases} -t^2 + t + \frac{1}{2} & 0.5 \leq t \leq 1 \\ \frac{1}{2}(1-t)^2 & 0 \leq t \leq 1 \end{cases} \tag{4.9}$$

$$p = 2 - 3t + t^3 \quad -1 \leq t \leq 1 \tag{4.10}$$

To locate the position of the maximum error in each computation, a comparison is performed between the calculation with a polynomial degree of $p = 20$ and a polynomial degree of $p = 10$ for each load case separately. Even though the solution of the eight element mesh and $p = 20$ might not be a real reference solution, its result is however of good quality as shown for the previous example of the rectangle discretized with two elements. The von Mises stresses are

---

[2] Remark: When studying the same geometry with loading along the complete bottom edge, no singularities occur in the solution domain. It would therefore not be possible to plot the convergence rate for the same geometry with a rectangular load along the complete edge. The linear displacement solution is too simple for a demonstration of the convergence behavior. A polynomial degree of one would therefore already represent the exact solution and an increase of the polynomial degree would have no benefit.

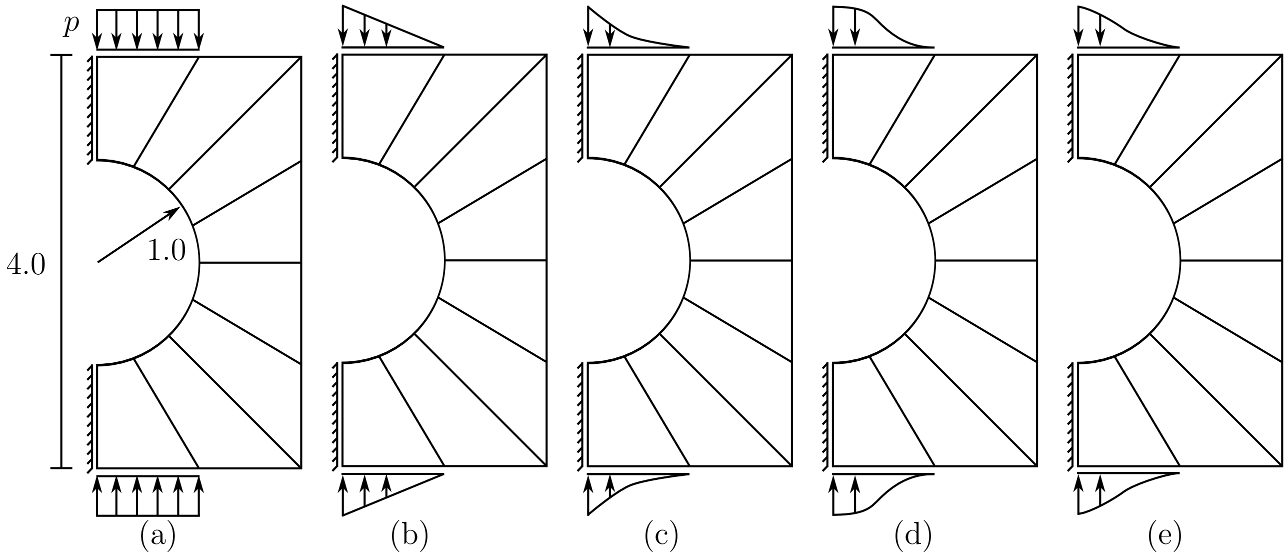

Figure 4.8: Plate with a hole and five different loading patterns. (a) rectangular, (b) triangular, (c) B-Spline with zero gradient where value is zero, (d) B-Spline with zero gradient on both sides, (e) Hermite polynomial.

chosen as an indicator for a qualitative measure to locate error sources. The relative error for each load case is shown in Figure 4.9. The legend of the plot is scaled to a maximum value of 0.1% of the maximal von Mises stress occuring inside the domain for the individual load pattern. The maximal value of the von Mises stress occurs where the horizontal axis of symmetry touches the circle. For the rectangular load distribution, e.g., the approximate maximal von Mises stress is around 2000 at this point (for $p = 20$ and $p = 10$). Values larger than 0.1% of the maximum von Mises stress are colored in red, as for the value of 0.1%. The plot in Figure 4.9 is thus displaying a range from 0 to 2. As an example for the error occurring in the rectangular load setup, the maximal difference in von Mises stresses (for the computation with $p = 20$ and $p = 10$) is around 70 and located at the end of the load application area.

As expected, a large error is visible at the end of the rectangular load (Figure 4.9(a)), in the middle of the upper and lower boundary. This results from the jump in the stresses, introduced by the rectangular load pattern. In comparison to the computation with $p = 20$, the polynomial of order ten is responsible for the checkerboard pattern in the error as it shows minor oscillations. The error induced at the end or the load, spreads though the two neighboring elements.

For the triangular load case plotted in Figure 4.9(b), a much smaller error (than for the rectangular load case) appears at the end of the load area in the middle of the upper and lower boundary. Still the two neighboring elements are affected by this error. The regularity of the solution is again reduced at this point, but not as much as for the rectangular load case. As in the previous example of the two element model, an error is also visible at the corner in the vertical axis of symmetry. It derives from the kink in the stresses at this point which is obvious if the full system would have to be modeled.

The plot in Figure 4.9(c) shows the error in the von Mises stresses for the quadratic B-Spline load distribution. Basically no error can be observed at the end of the applied load, where the

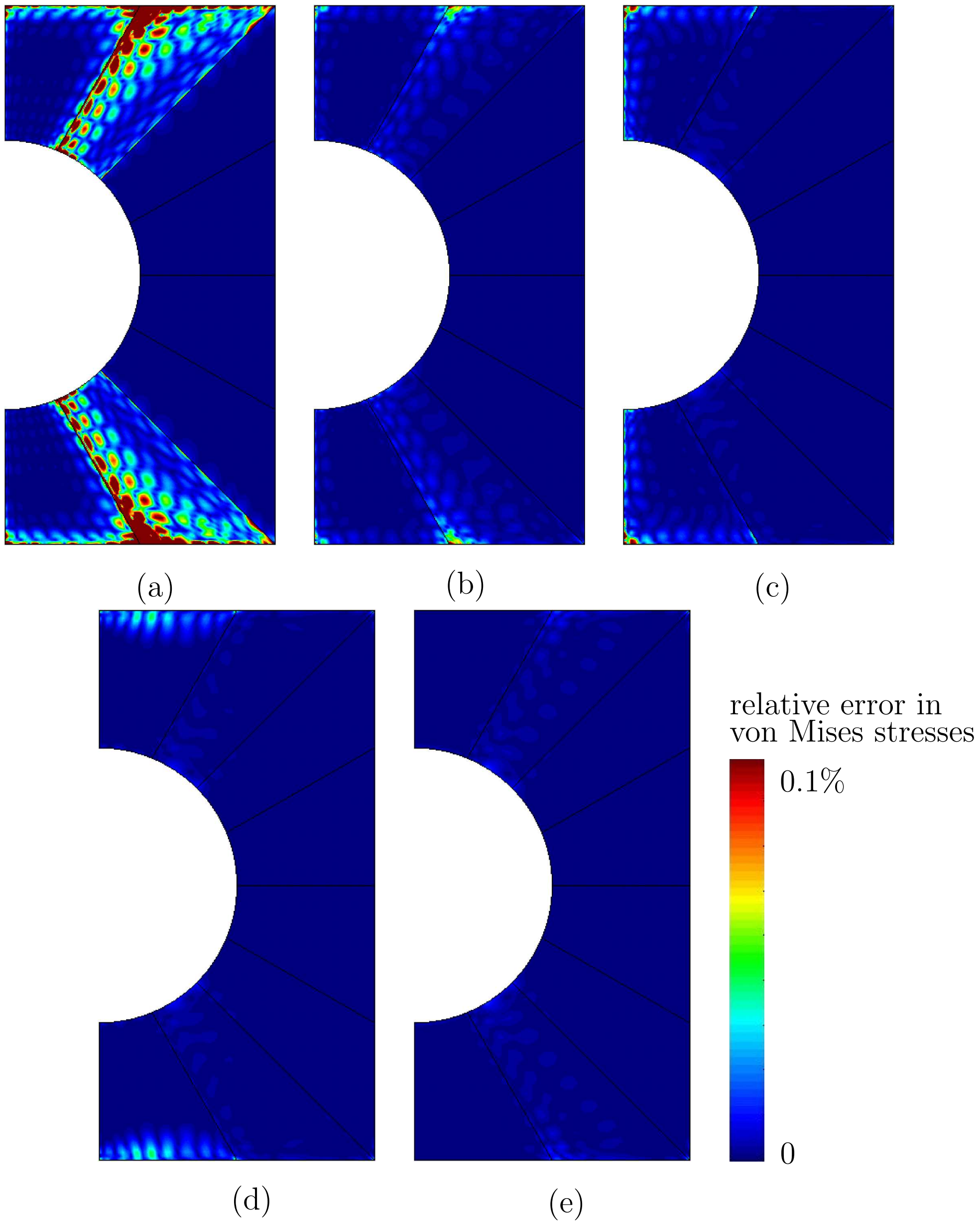

Figure 4.9: Relative error in von Mises stresses for the different load cases given in Figure 4.8. High discontinuities are visible at the end of the applied load for the rectangular load case (a) and the triangular load case (b). For the case of the plate with a hole being loaded by a B-Spline load distribution (c), very small errors are visible. No errors at the end of the loading are visible for loadings of type (d) and (e). Loading (d) shows errors at the C^1 continuous position where the segments of the piecewise B-Spline are assembled.

gradient of the load is zero. But here an error is visible in the same corner as for the triangular load case, at the axis of symmetry. This error results from the fact that the gradient of the loading function is nonzero in the symmetry axis, therefore imagining the full system and load, a kink in the load distribution is present at this point. This non-smooth load distribution in the axis of symmetry, induces a local error in the computation.

Another computation is performed with a quadratic piecewise B-Spline load function having a zero gradient at both ends of the load (Figure 4.9(d)). Here, no error prone area is visible at both ends of the applied load, but small oscillations can be seen in the interior of the loading domain. This derives from the fact, that a piecewise quadratic B-Spline with the given properties (zero gradient on both sides) is only C^1 continuous at the interior point where the segments of the piecewise B-Spline are assembled. This reduced regularity results in oscillations around this point when polynomial functions are used for its discretization. Even though the amplitude of the error is quite small, its influence area is relatively large compared to the triangular or B-Spline load case.

Finally another computation is performed, using a scaled Hermite polynomial to describe the load distribution. No error can be seen in the whole domain, proving that a load does only then induce no error to the solution, when not only the function value, but also its derivatives fulfills certain criteria. On the free boundary, the function value and its derivative needs to be zero and on the axis of symmetry, only the derivative (gradient) needs to be zero.

This example shows the sensibility of the results toward the shape of the applied distributed load. These Figures also show, that for every load pattern unlike the Hermite polynomial (or others with similar properties), some error source will remain in the solution.

The convergence rates of the error in energy norm is plotted for the plate with a hole and every load pattern in Figure 4.10 for polynomial degrees from $p = 2$ to $p = 15$. As reference solutions the energy for each individual load case and $p = 20$, computed on the same meshes, is used. The pre-asymptotic exponential, asymptotic algebraic rate of convergence is clearly visible

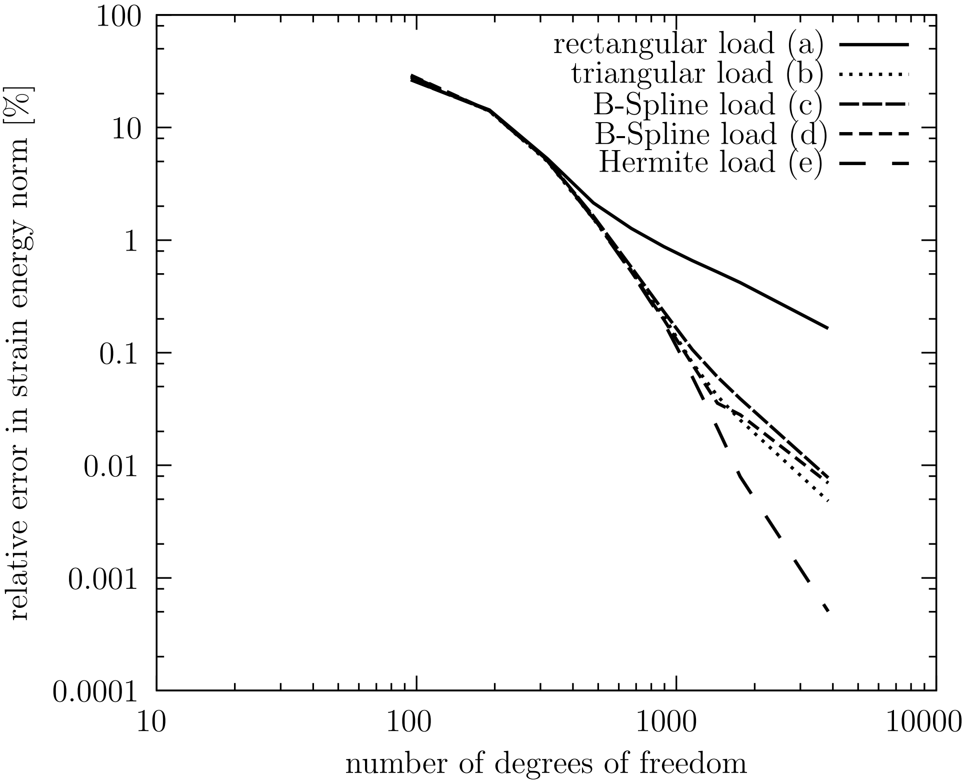

Figure 4.10: Pre-asymptotic exponential, asymptotic algebraic rates of convergence of relative error in energy norm for the plate with a hole under the five different loading patterns shown in Figure 4.8. It can well be seen that the rectangular load distribution shows the worst, and that the Hermite polynomial load distribution shows the best rates of convergence.

for all curves. The rectangular load case shows the slowest rate of convergence compared to the other curves. The pre-asymptotic range is shorter here because the singularity introduced at the end of the load is quantitatively larger than the remaining error in the domain and therefore governing the convergence behavior. The other load cases show better rates of convergence. The curve for the Hermitian load clearly possesses the highest convergence rates in this comparison which even have a tendency to be of exponential type. It should generally be noted, that all load cases exhibit a level of accuracy which is extraordinary. Additionally, the trend of the curves in Figure 4.10 is matching the results displayed in Figure 4.9 for the error in von Mises stresses very well.

To summarize the results obtained for the Neumann boundary condition it can be said that errors occur at the end of a Neumann load if this position does not coincide with for example a ninety degree corner of the geometry in the direction of the applied load. These errors can only be avoided by meeting special properties in the shape of the load. These special properties involve the smoothness of the load distribution and the value of the load and its derivative at the end of the load area. The load distribution has to be representable by a polynomial function. At the end of the load area, the value of the load and its directional derivative have to vanish. If these requirements are not met, areas with reduced regularity appear in the domain. This results in a potentially pre-asymptotic exponential, but certainly asymptotic algebraic rate of convergence because at some point the reduced regularity at the end of the applied load (or inside the load distribution for case (d)) will control the convergence rate.

4.6 Conclusions for the Mechanical Contact Problem

As discussed in the previous sections, the regularity for a general mixed boundary value problem like the contact problem is reduced at the contact interface point Γ_* on the boundary Γ. This was shown by the discussion on the stress intensity factor and by considerations regarding the Neumann boundary and its analogy with the contact problem. The solution of u admits near each of the Γ_* a separate asymptotic expansion of the type given in Equation 4.6. The stress intensity factor at the contact interface point is generally nonzero, indicating a reduced regularity at this point. Using the analogy of the contact problem to a Neumann boundary condition it turns out that for the general case of contact problems, at least a reduced regularity occurs at the end of the contact interface at Γ_*. The contact problem is therefore in general a problem of reduced regularity and is non-smooth, which theoretically entails a convergence rate of algebraic type for the error in energy norm when a pure h- or p-version of the FEM is used[3].

In the following, the *rp*- and *hp*-version of the FEM will be explained as two extensions for the classical h- and p-version. Both methods make use of a posteriori error estimators and are used in the study of contact mechanical problems.

---

[3] Beside the previously discussed matter of singularities at the end of a Neumann boundary condition the application of a pure h- or p-version is even more crucial, as generally the end point Γ_* of the contact interface does not coincide with a Finite Element node. This change in boundary condition inside a Finite Element leads to oscillations of the polynomial shape function.

4.7 *hp*-Extension

The *hp*-version, is an adaptive method and an extension of the *p*-version. It combines the *p*-version with a local mesh refinement. In areas with strong discontinuities, or large gradients, it uses small elements with low polynomial degrees to minimize the influence area of the singularity. In areas with smooth solutions large elements with higher polynomial degrees are used. In the case of a point singularity, the resulting meshes are graded, such that the sizes of elements decrease in geometric progression towards the critical point [81]. For the 1D case, the geometric progression factor which leads to the optimal results is 0.17 [81], even though some authors (see [15]) use a constant progression factor of 0.5. As the element size decreases towards the singular point, the elements' polynomial degree decreases in a optimal extension strategy as well. A singularity will therefore be discretized (framed) with small low order Finite Elements. This limits the influence area and reduces oscillations in the results which could occur when higher polynomials are used at the singularity. More details on the *hp*-version can be found in [2, 3, 15, 16, 17, 53, 61, 62, 71]. Even for problems with singularities, this method allows to obtain exponential rates of convergence of the error in energy norm. An example for this is the so called L-shaped domain which exhibits a singularity at the reentrant corner. The example is discussed in the literature, e.g. [81] or [59]. As the *hp*-version is beneficial when point singularities occur in the solution domain, its application to contact mechanical problems is logical. The idea is to refine the mesh close to the end of the contact interface at Γ_* in order to isolate the source of error which is present there. First an estimate of the approximate location of the contact interface point Γ_* has to be obtained. The new location of Γ_* can be derived from the gap values at the different Gauss points of an edge in contact (see Figure 4.11) after each Finite Element computation. The method is thus using a posteriori informations to modify the mesh for the next computation. The difference between the previous and current estimated position of Γ_* can be understood as an a posteriori error estimation. In Figure 4.11, the Gaussian points on boundary Γ_c^1 of object Ω^1 are denoted as GP_1, GP_2, and GP_3. The domain of the rigid objects is denoted as Ω^2 and Γ_c^2 is its corresponding boundary. As stated before, it is of crucial importance to detect the exact location of Γ_*. Knowing that the critical point is at the end of the contacting zone, an estimated position can be obtained from the active and inactive sets of Gauss points used for the contact detection. When the penalty method is used, a small penetration of the two bodies is allowed for in the contact interface. Due to the fact that Gauss points are used to calculate the gap between the two colliding objects, there must be two neighboring Gauss points where the gap function changes from penetration to no penetration (see GP_2 and GP_1 in Figure 4.11). By making use of the Pegasus method [22] as a numerical root finding algorithm, a new approximated location of the contact interface point Γ_* can be computed from the two neighboring Gauss points. Once Γ_* is determined for the current setup, the mesh will be refined in a *hp*-manner, such that the smallest element encloses Γ_*. A progression factor of 0.5 towards Γ_* is chosen. A sketch

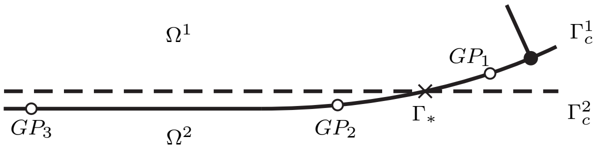

Figure 4.11: Derivation of the contact interface point Γ_*.

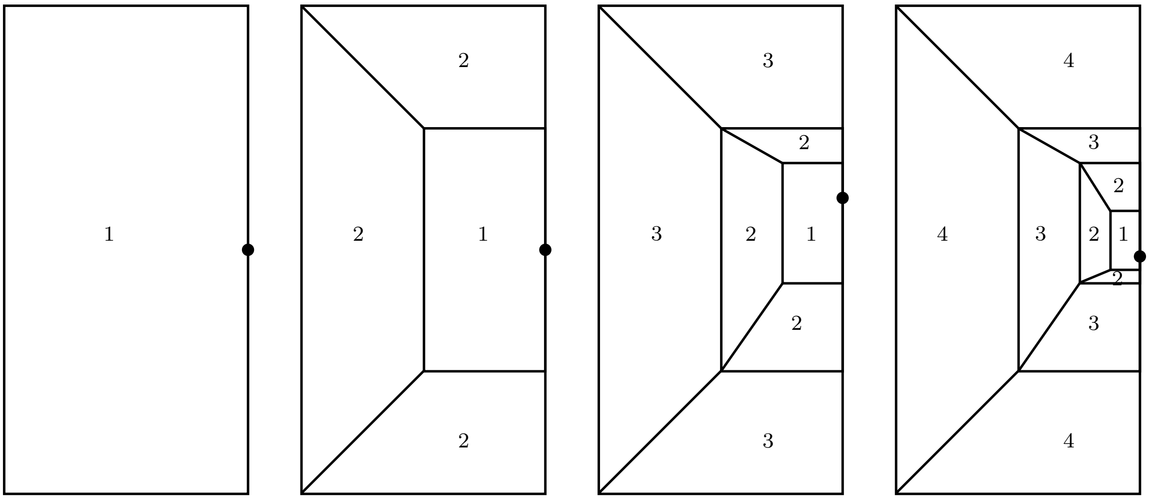

Figure 4.12: Schematic procedure of the *hp*-method for a fictitious singularity at the position marked with the dot. The progression rate of the *hp*-method in this example is 0.5.

of the schematic procedure of the *hp*-method is given in Figure 4.12. The numbers inside the mesh indicates the polynomial degree of the corresponding element. The dot • marks the position of a singular point in the solution (like the contact interface point Γ_*) whose position has changed after each iteration step. With decreasing element size it may happen that the new position of Γ_* does not fall in the previously defined interval where Γ_* is expected to be located in. Therefore a *hp*-refinement from at least the second last mesh towards the new guess of the contact point Γ_* needs to be allowed for.

A flowchart of the adaptive *hp*-method that is used in a contact mechanical simulation is given in Figure 4.13. The gap function will be evaluated in an a posteriori step, allowing to estimate

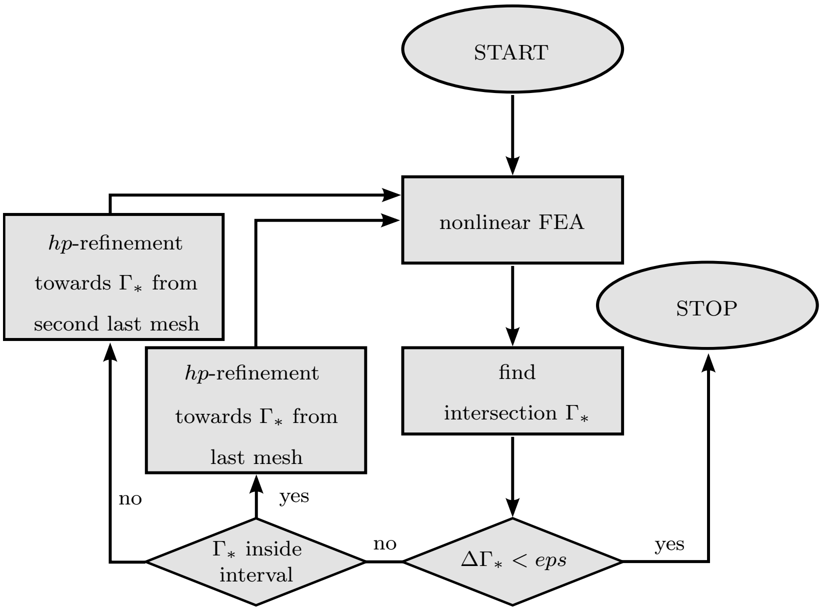

Figure 4.13: Iterative mesh generation for the adaptive *hp*-method of the FEM, by computing the contact interface point Γ_*.

a new position of the contact interface point Γ_*. The stop criterion is denoted by *eps*. The increment of the contact interface position Γ_* between the last and the current iteration step is given by $\Delta\Gamma_*$. The *hp*-refinement step involves, in addition to the mesh refinement, an adaptive *p*-refinement, which means a reset of the polynomial orders of each finite element.

4.8 *rp*-Extension

The *rp*-extension, like the *hp*-extension gives the opportunity to resolve singular points in the solution. The use of high order polynomials as shape functions for the displacements does cause problems when singularities are present within one element, as these singularities introduce an error in the computation. Its discretization with high order Finite Elements leads to oscillations in the stresses around the singular point as the polynomial function tries to resolve the singularity. One way to reduce, or even eliminate these oscillations is to make use of the C^0 continuous nature of the FEM and place a Finite Element node or edge exactly at the existing singularity. This also motivates the name of the method, as the *r* in the *rp*-method stands for *relocation.* In contrast to a complete remeshing, only one, or a few Finite Element nodes, or edges change their position during the relocation process. No extra FE node is added by applying this method. The method works in such a way that it relocates a FE-node, edge, and or face in order to coincide with the existing singularity. Exponential rates of convergence can be obtained for certain nonlinear problem classes.

It was shown in [60] that exponential convergence rates in energy norm are achievable with the *rp*-version for nonlinear problems of elastoplasticity in 2D. The exponential convergence rates were made possible by having the elastic-plastic front coincide with an element's boundary in an iterative edge relocation process, thus making use of the *rp*-method. A change from elastic to plastic material behavior inside one element leads to a kink in the element's displacement field. This kink has a similar influence on the solution as a loss of regularity has due to a change in the boundary conditions (as for contact problems), or a change in the material properties. For the case of non-fitting mesh and plastic front, the shape functions are not able to display the kink and therefore the approximation starts to oscillate.

Figure 4.14 gives the flowchart of the *rp*-algorithm for the contact problem. After one converged computation, the current contact interface point Γ_* is detected in the same manner as described for the *hp*-extension. Once the approximate position of Γ_* is known, the closest Finite Element node on the boundary will be moved to the position of Γ_*. Due to the nonlinear nature of the problem, several iterations are needed in order to get a good estimate for the position of Γ_*. As the polynomial degree of the ansatz space is constant over the domain and throughout the computation, no extra loop for a *p*-adaption is needed.

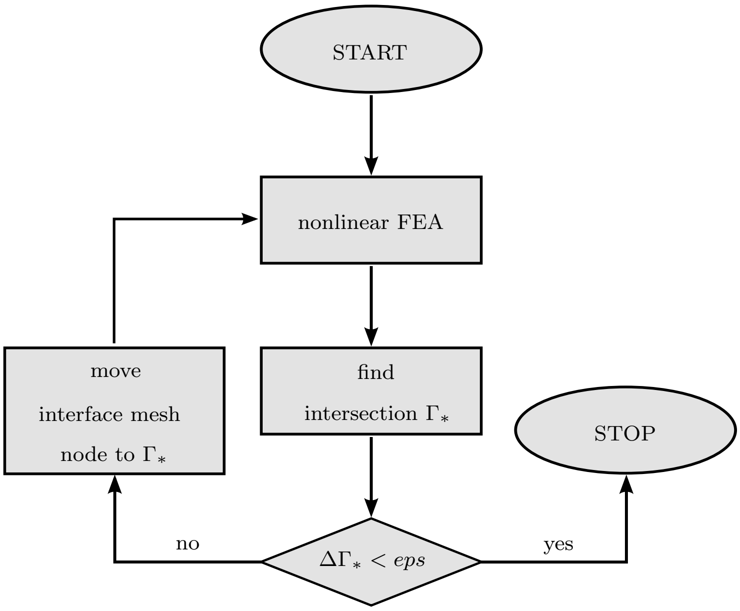

Figure 4.14: Iterative mesh relocation for the *rp*-method of the FEM by computing the contact interface point Γ_*.

4.9 Extrapolation Method to Estimate the Exact Solution

In order to be able to plot error curves of various kind, the exact solution of a given problem has to be known. For linear problems an analytical solution might be available for simple geometries, but as soon as the geometries become more complicated, nearly no exact solution is known. The same applies if physical or geometric nonlinearities are considered. For these examples usually a reference solution has to be derived numerically by for example an *overkill* solution, which is characterized by a very large number of elements and high polynomial orders. Another possibility to estimate the exact (reference) solution for a given problem is to extrapolate a solution from existing numerical simulations. This of course bears the risk to estimate a reference solution which is in no way close to the real exact solution if the used data for the extrapolation is far from exact. This could happen if for example important nonlinear effects are not at all considered in the computation, or the chosen model or discretization is simply not suited for this example[4]. Therefore the approximated results used for the extrapolation method should be checked against results obtained by a third party program.

In the following the extrapolation method will be presented which uses the numerical result of three consecutive computations. In case of the *h*-version of the FEM where the solution's quality is improved by global or local mesh refinement, it has to be ensured that the Finite Element meshes are hierarchically refined such that the finer meshes embed the coarser ones. For the *p*-version, three consecutive polynomial degrees have to be chosen and used for a computation on the same mesh to extrapolate the exact solution. The *p*-version's hierarchic

---

[4] This is of course a problem which is present for any numerical simulation.

ansatz space ensures a monotonic convergence characteristic which is a prerequisite for the application of the extrapolation method discussed here. The method has proven to be reliable and accurate (see [79]) especially when the number of degrees of freedom is sufficiently large. Starting with the strain energy $\mathcal{U}(\mathbf{u})$ given in Equation 2.30,

$$\mathcal{U}(\mathbf{u}) = \frac{1}{2}\,\mathcal{B}(\mathbf{u},\mathbf{u})$$

Equation 4.2 can be derived

$$\|\mathbf{e}\|^2_{E(\Omega)} \;=\; \|\mathbf{u}_{ex} - \mathbf{u}_{FE}\|^2_{E(\Omega)} = |\mathcal{U}(\mathbf{u}_{ex}) - \mathcal{U}(\mathbf{u}_{FE})| \;.$$

Using the property of Galerkin's methods that the strain energy $\mathcal{U}(\mathbf{u}_{FE})$ is monotonically increasing, and therefore $\mathcal{U}(\mathbf{u}_{ex}) > \mathcal{U}(\mathbf{u}_{FE})$, Equation 4.2 can be transformed to

$$\|\mathbf{e}\|^2_{E(\Omega)} \;= \mathcal{U}(\mathbf{u}_{ex}) - \mathcal{U}(\mathbf{u}_{FE}) \;. \tag{4.11}$$

The error for the algebraic rate of convergence given in Equation 4.4 is assumed to derive

$$\|\mathbf{e}\|^2_{E(\Omega)} \approx \frac{k^2}{N^{2\beta}} \tag{4.12}$$

for the error in energy norm. With Equation 4.11 being set equal to Equation 4.12 follows

$$\mathcal{U}(\mathbf{u}_{ex}) - \mathcal{U}(\mathbf{u}_{FE}) \approx \frac{k^2}{N^{2\beta}} \;. \tag{4.13}$$

Choosing the polynomial degrees of $\{p-2, p-1, p\}$ with the number of degrees of freedom $\{N_{p-2}, N_{p-1}, N_p\}$ and the strain energies $\{\mathcal{U}_{p-2}(\mathbf{u}_{\mathrm{FE}}), \mathcal{U}_{p-1}(\mathbf{u}_{\mathrm{FE}}), \mathcal{U}_p(\mathbf{u}_{\mathrm{FE}})\}$ of the exact solution $\mathcal{U}(\mathbf{u}_{\mathrm{ex}})$ can be estimated with Equation 4.14. For each of the three computation an equation of the form 4.12 can be formulated. When the logarithmic quotient of the number of degrees of freedom of subsequent calculations is considered as well, the exact solution can be estimated from the following relation:

$$\frac{\mathcal{U}(\mathbf{u}_{\mathrm{ex}}) - \mathcal{U}_p(\mathbf{u}_{\mathrm{FE}})}{\mathcal{U}(\mathbf{u}_{\mathrm{ex}}) - \mathcal{U}_{p-1}(\mathbf{u}_{\mathrm{FE}})} \;\approx\; \left(\frac{\mathcal{U}(\mathbf{u}_{\mathrm{ex}}) - \mathcal{U}_{p-1}(\mathbf{u}_{\mathrm{FE}})}{\mathcal{U}(\mathbf{u}_{\mathrm{ex}}) - \mathcal{U}_{p-2}(\mathbf{u}_{\mathrm{FE}})}\right)^{\left(\frac{\log\frac{N_{p-1}}{N_p}}{\log\frac{N_{p-2}}{N_{p-1}}}\right)} \tag{4.14}$$

where an iterative method like the Newton-Raphson scheme has to be used to derive an estimate for the exact solution of the energy norm $\mathcal{U}(\mathbf{u}_{\mathrm{ex}})$.

Chapter 5

Numerical Examples

To illustrate the performance of the developed and implemented methods, the concepts introduced in the previous chapter are applied in the following on various examples. The examples include unilateral, bilateral, frictionless and frictional contact problems with small and large displacements. Special attention is drawn to the Hertzian contact problem in 2D which is used to study the performance of each method presented earlier like the *h*-, *p*-, *rp*-, and *hp*-version of the Finite Element Method, for their application on mechanical contact problems[1].

5.1 Plate with a Hole in Full Contact

The first example is chosen to demonstrate that the chosen contact formulation is consistent and complete. The unilateral setup of the symmetric half of the plate with a hole being pressed onto a rigid plate is given in Figure 5.1. The bottom edge is completely in contact with the rigid block. Symmetry boundary conditions are chosen on the left side. The Neumann boundary at the top of the plate is loaded by a distributed force of 1000 $[N/mm^2]$ in vertical direction. The plate has a thickness of one. To incorporate the contact constraints with the penalty method, a penalty factor of $1000 * E$ (with E being the Young's modulus) and a Poisson ratio of $\nu = 0.29$ is chosen. The geometry of the plate with a hole is discretized with four elements. The circular geometry of the hole is represented exactly by the blending function method (see Section 2.2.4). Figure 5.2 shows the deformed mesh and the von Mises stresses for the described problem computed with a shape function's polynomial degree of six. For the same computation, the stresses in vertical direction are plotted in Figure 5.3. The deformation in both Figures is scaled by a factor of ten. The reference solution is derived on the same mesh, but with fixed Dirichlet boundary conditions in vertical direction along the bottom edge. It therefore does not allow for any penetration or angular deflection of the edge at the bottom. The reference solution is needed in order to plot the relative error in energy norm for different polynomial degrees in the ansatz spaces. The plot in Figure 5.4 shows the convergence of the relative error in energy norm for the given problem with polynomial degrees varying from $p = 2$ to $p = 6$. The x-axis plots the number of degrees of freedom, whereas the y-axis plots the relative error in energy norm (relative to the reference solution). Both axis have a logarithmic scale. An exponential rate of convergence can be observed in the chart. This

---

[1] The charts are generated with the software Gnuplot [32]. The colored stress-plots are created with the software-tool GiD [30]. The program Inkscape [47] is used to further format the Figures.

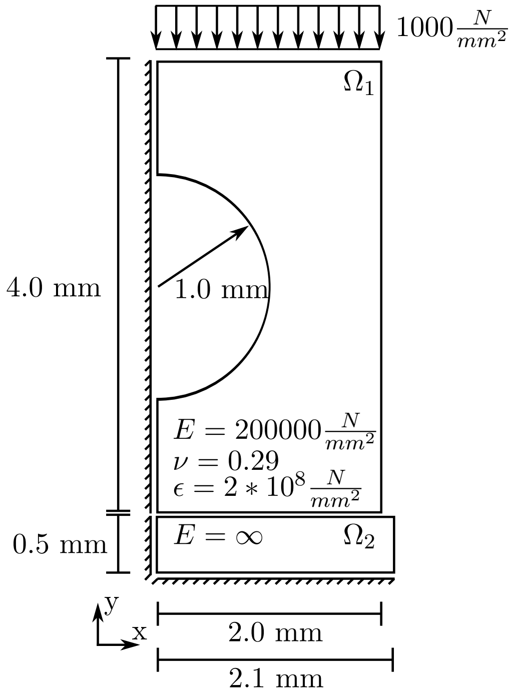

Figure 5.1: Model of the plate with hole Ω_1 in contact with a rigid plate Ω_2.

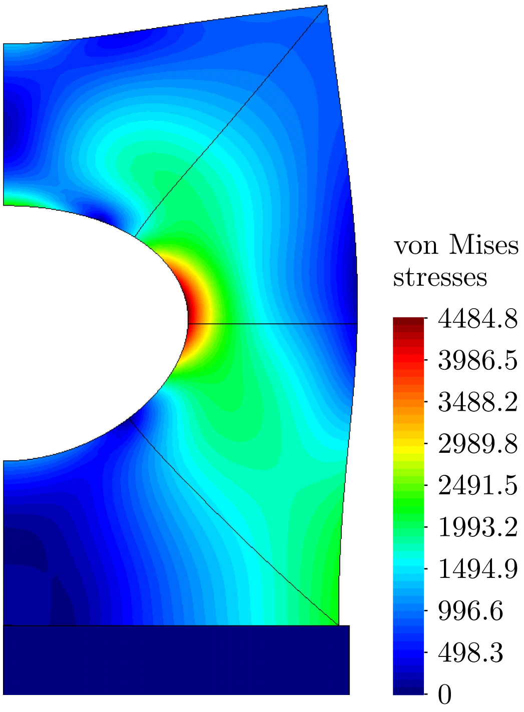

Figure 5.2: Von Mises stresses plotted on a ten times scaled deformed geometry for the plate with hole in contact and $p = 6$.

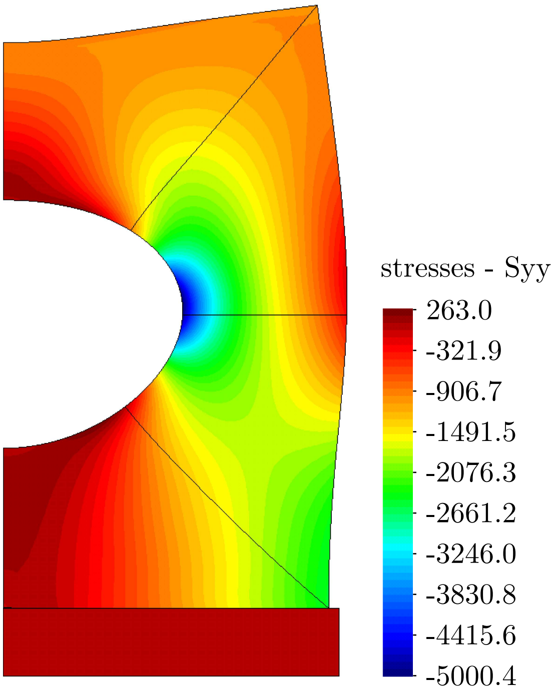

Figure 5.3: Stresses in vertical direction plotted on a ten times scaled deformed geometry for the plate with hole in contact and $p = 6$.

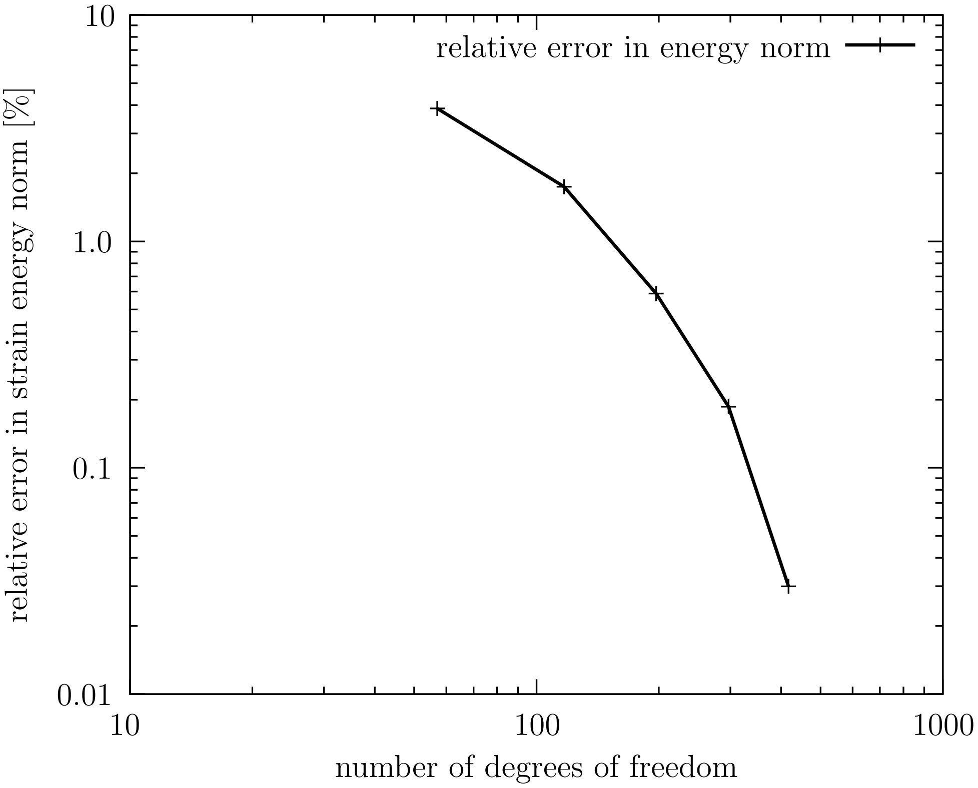

Figure 5.4: Exponential convergence rate of the relative error in energy norm for the plate with hole example for $p = 2$ to $p = 6$.

is due to the fact that the example has a nonuniform, but regular and continuous boundary condition without sudden changes. The bottom edge, which is contacting the rigid object, is completely in contact. Thus no singularity occurs inside the solution domain, neither on the loaded nor on the contact edge. The exponential rate of convergence obtained for this contact problem is therefore the usual convergence of the p-version of the Finite Element Method for smooth problems without singularities.

5.2 2D Hertzian Contact Problem

Intensive tests are performed on the two dimensional Hertzian contact problem. The general three dimensional problem of two contacting cylinders of infinite length, can be reduced to a two dimensional, plane strain problem as shown in Figure 5.5. This example is one of the few for which an analytical solution exists for various parameters like the contact width, and contact stresses in the contact interface. An analytical solution for this problem was first published by Hertz [42] in 1881.

5.2.1 Hertz Theory

Hertz introduced the following assumptions: Each body can be regarded as an elastic, homogeneous and isotropic half-space loaded over a small elliptical region of its smooth surface. The surfaces are assumed to be frictionless, the contact interface is assumed to be small compared to the surfaces' radii and body's dimensions. The circular geometry of the contact boundary is approximated by a quadratic polynomial. For the unilateral case where the radius of the bottom cylinder is taken as infinite, rigid material properties are assumed as shown in Figure 5.6.

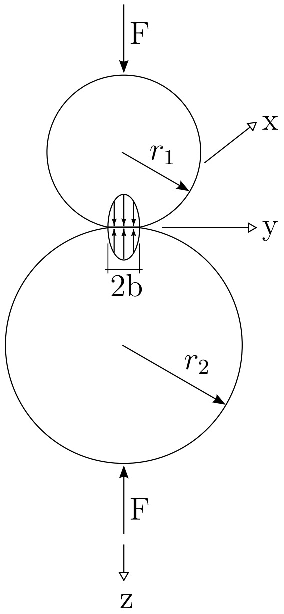

Figure 5.5: 2D plane strain Hertzian contact model for two infinitely long cylinders.

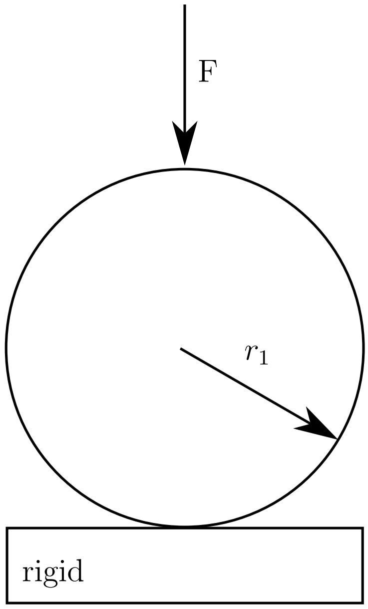

Figure 5.6: 2D plane strain Hertzian contact model for contact between a cylinder and a rigid plate.

We consider the situation of two cylindrical objects that are in contact as depicted in Figure 5.5. Following [72] Hertz's analytical solution, the half width b of the contact interface can be expressed as

$$b = \sqrt{\frac{4F}{\pi l} \frac{\left(1-\nu_1^2\right)/E_1 + \left(1-\nu_2^2\right)/E_2}{(1/r_1) + (1/r_2)}} \, . \tag{5.1}$$

In the x-direction, the contact interface of half width b has a rectangular shape. Its size depends on the applied force F in z-direction, the Poisson ratios ν_1 and ν_2 for each cylinder respectively, the corresponding elastic moduli E_1 and E_2, the sphere's radii r_1 and r_2, and the cylinder's length l in x-direction. The pressure distribution for the half width b in the contact interface is given with Equation (5.2) (see [33]):

$$\begin{aligned} p(y) &= \frac{2F}{\pi l b^2}\sqrt{b^2-y^2} \\ &= \frac{\frac{1}{2r_1}+\frac{1}{2r_2}}{\frac{1-\nu_1^2}{E_1}+\frac{1-\nu_2^2}{E_2}} \sqrt{\frac{2F\frac{1-\nu_1^2}{E_1}+\frac{1-\nu_2^2}{E_2}}{\pi l\left(\frac{1}{2r_1}+\frac{1}{2r_2}\right)} - y^2} \, . \end{aligned} \tag{5.2}$$

For the case of having one cylinder in contact with a flat and rigid plate, r_2 and E_2 have to be set to ∞. The pressure distribution in the contact interface, Equation (5.2), then reduces to

$$p(y) = \frac{E}{2r\,(1-\nu^2)}\sqrt{4F\frac{(1-\nu^2)\,r}{\pi l E} - y^2}\,. \tag{5.3}$$

More quantities can be calculated using Hertz's theory, but they will not be listed here. For further discussion see Shigley et al. [72], Goldsmith [33], Johnson [48], and Wriggers [88].

The Hertzian Model was improved by Shtayerman in 1939 by allowing for a general geometric description (e.g. higher order polynomials) of the contacting bodies in the contact interface. A detailed discussion can be found in Shtayerman [73]. The relevant equations are summarized in [49] and given below. The geometric outline of the gap function is defined by

$$f(t) = f_1(t) - f_2(t) \tag{5.4}$$

with $f_1(t)$ and $f_2(t)$ being the geometric representations of body one and two respectively. The interval of the contact width b is derived from the following two relations

$$\int_{-b}^{b} \frac{f'(t)dt}{\sqrt{b^2-t^2}} = 0 \tag{5.5}$$

$$\int_{-b}^{b} \frac{tf'(t)dt}{\sqrt{b^2-t^2}} = K\,F \tag{5.6}$$

$$\text{with} \quad K = \frac{\kappa_1+1}{4\,G_1} + \frac{\kappa_2+1}{4\,G_2}\,. \tag{5.7}$$

Using G_i for the shear modulus and ρ_i for the Poisson's ratio of i^{th} body ($i = 1, 2$), κ_i is derived as:

$$\kappa_i = 3 - 4\nu_i \text{ for plane strain} \tag{5.8}$$

$$\kappa_i = \frac{3-\nu_i}{1+\nu_i} \text{ for generalized plane stress}\,. \tag{5.9}$$

The contact pressure distribution in the interval $(-b, b)$ is then given by

$$p(y) = \frac{\sqrt{b^2-y^2}}{\pi\,K}\int_{-b}^{b} \frac{f'(t)dt}{\sqrt{b^2-t^2}(t-y)}\,. \tag{5.10}$$

5.2.2 Numerical Model

The geometric setup of the model used for the numerical simulation is plotted in Figure 5.7 for the unilateral plane strain case of a cylinder which is pressed onto a rigid plate. Only one quarter of the full model is discretized to reduce the computational effort. The circular geometry is represented exactly in this model by the blending function method. Symmetric boundary conditions are applied in the $x-z$ plane. In order to eliminate the influence of the concentrated single load at the top of the cylinder, the load is replaced by an equivalent uniform

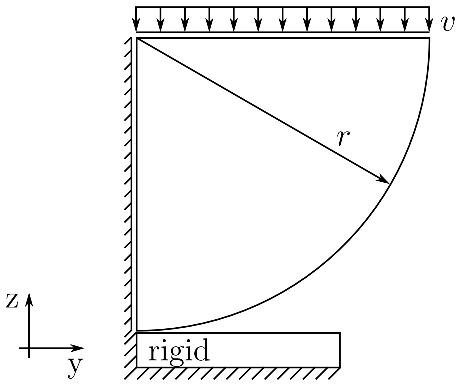

Figure 5.7: Hertz model for the unilateral 2D case.

$$
\begin{aligned}
E &= 2.1 \times 10^5 \frac{N}{mm^2} \\
\nu &= 0.29 \\
r &= 10mm \\
v_0 &= 0.49055988mm \\
\epsilon_n &= 2.1 \times 10^8 \frac{N}{mm^2}
\end{aligned}
$$

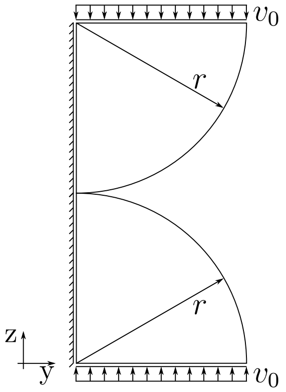

Figure 5.8: Hertz model for the bilateral 2D case.

Dirichlet boundary condition at the cylinders center plane. The simulation model applies the following parameter values [25]: The length of the cylinder is set to one (in x-direction) and the penalty value ϵ_n is chosen to be 1000 times higher than the Young's modulus E and therefore set to $\epsilon_n = 2.1 \times 10^8 [N/mm^2]$. The value of the penalty parameter is crucial for the accuracy and numerical stability of the contact problem. As the penalty parameter is directly influencing the amount of penetration which is allowed for the contacting objects, it also has an influence on the accuracy of the solution. Therefore a large penalty value is beneficial. Unfortunately the penalty parameter is assembled in the stiffness matrix and introduces large values in off diagonal positions. This dramatically increases the condition number witch effects the stability and convergence rate of the Newton algorithm. The choice of the penalty parameter is therefore a compromise between accuracy and condition number of the resulting equation system. For the given example, the penalty factor of $\epsilon_n = 2.1 \times 10^8 [N/mm^2]$ is chosen because further studies revealed that a further increase of the penalty parameter by a factor of more than 7 resulted in an increase of the maximal contact pressure of less than 0.02%.

The prescribed displacements v_0 along the Dirichlet boundary corresponds to a resulting load F on the Hertzian model of $70000 [N]$, see Figure 5.5. The use of a quarter system instead of a half, or even the full system has several advantages. First of all, the computational effort is reduced when the quarter system is computed. Furthermore, the reduced quarter system allows to eliminate the influence of the single concentrated load with which the Hertzian problem is usually loaded. As it was shown in Section 4.5, a single load, as well as most distributed loads induce singularities in the solution domain. Loading the quarter system by a Dirichlet boundary condition at its top boundary instead allows to omit these error sources. Differences in the results obtained during the following contact survey can thus only originate from a different discretization of the contact region. Therefore the following study allows to discuss solely the contact phenomena.

To derive the displacement distribution for the quarter system, computations are performed on the symmetric half system first. From these computations, the displacement distribution at the cylinder's mid height is plotted in Figure 5.9. By taking this displacement distribution as the load for the quarter system, singularities due to the loading do not occur. As a simplification, a constant displacement distribution is used as the load for the quarter system instead of the distribution derived from the symmetric half cylinder system. A small error is caused by using

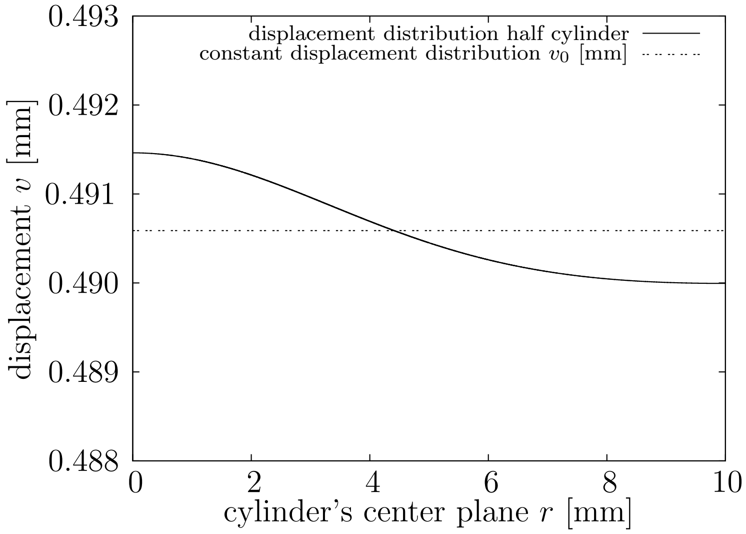

Figure 5.9: Comparison of the derived displacement in z-direction at cylinder's mid height and assumed constant Dirichlet boundary condition which is used in the following computations.

this constant displacement on the Dirichlet boundary v_0 on the quarter cylinder instead of a Neumann boundary condition F on the top of the half cylinder. Choosing a half cylinder with Neumann boundary condition for the computation, the resulting displacement distribution in z-direction at cylinder's mid height is almost constant over the cylinder's width, as plotted in Figure 5.9. The difference between the smallest and the biggest displacement value in z-direction on the cylinder's mid height is 0.3%. The Figure also shows the constant displacement distribution on the Dirichlet boundary which is applied in the following computations. The constant value for the prescribed displacement distribution on the Dirichlet boundary is chosen such that its integral value is equal to the integral displacement distribution derived from computations of the half cylinder model. Comparing the maximal contact pressure computed with the half cylinder and the maximal contact pressure computed with the Dirichlet boundary condition, the error $\left(\left(\sigma_{half} - \sigma_{average}\right)/\sigma_{half}\right)$ turns out to be in the order of 0.0001%.

5.2.3 Numerical Results

The numerical results presented in this section show the comparison of the different FE-methods described in the previous chapter. The comparison is performed by means of the contact pressure distribution in the contact interface and its vicinity against the Hertzian solution given in Section 5.2.1, and by means of the convergence rates of the error in energy norm. Although the maximal/minimal stresses and strains are generally a matter of engineering concern, it is the contact pressure that is mainly discussed in this section. In order to prove the reliability and accuracy of a method, a single value like the maximal or minimal stress would not be capable of giving the explanation for every phenomena observed. In addition to that, problems like wearing require that the stress distribution on the contact boundary is known as well. Wear, as a surface phenomenon, is a critical factor that can limit substantially the life span of machines [39]. Oscillations in the pressure distribution will artificially scarify the surface and reduce the simulated resistance against wear. Understanding the error's source is essential for the development of techniques to improve the quality of the solution.

5.2.3.1 Contact Stresses for the h-Version of the FEM

In a first step, we consider the Hertzian model defined in Section 5.2 and 5.2.1 (Figure 5.7). Starting with the classical h-version of the FEM we use three different meshes which are depicted in Figures 5.10(a), 5.10(b), and 5.10(c). Mesh 5.10(a) is a uniformly distributed, irregular mesh with 335 quadrilateral elements. Mesh 5.10(b) is uniformly refined and consists of 995 quadrilateral elements and mesh 5.10(c) is a mesh with 315 elements which is a priori locally refined in the contact region. The contact pressure distribution for each of the three meshes with isoparametric elements and a polynomial degree of one is presented in Figure 5.11. The axes in Figure 5.11 plot the normal contact pressure against the contact width. Both axes are normalized with the analytical value for the contact width b and the maximal analytical contact pressure p_{max} to a value of one[2]. The solid line represents the contact pressure distribution derived by the Hertzian formula (Equation 5.10), whereas the other three curves plot the pressure distribution for the meshes given in Figure 5.10. The circle in the lower left corner of the graph shows a magnification of the end of the contact interface. As the pressures are derived from the post processing (from the strains), a non-continuous pressure distributions in the contact interface can be observed. The zig-zag path follows from the C^0 continuous approach of the linear FE method, which leads to jumps in the stress distribution at element nodes. This effect is well known and discussed in literature [52, 37]. Mesh (c) (Figure 5.10) gives the best results out of this three meshes due to its refined discretization in the contact region. However, the advantage in accuracy and time against mesh (b) (Figure 5.10) is counterbalanced by the additional effort of creating the a priori or iteratively locally refined mesh.

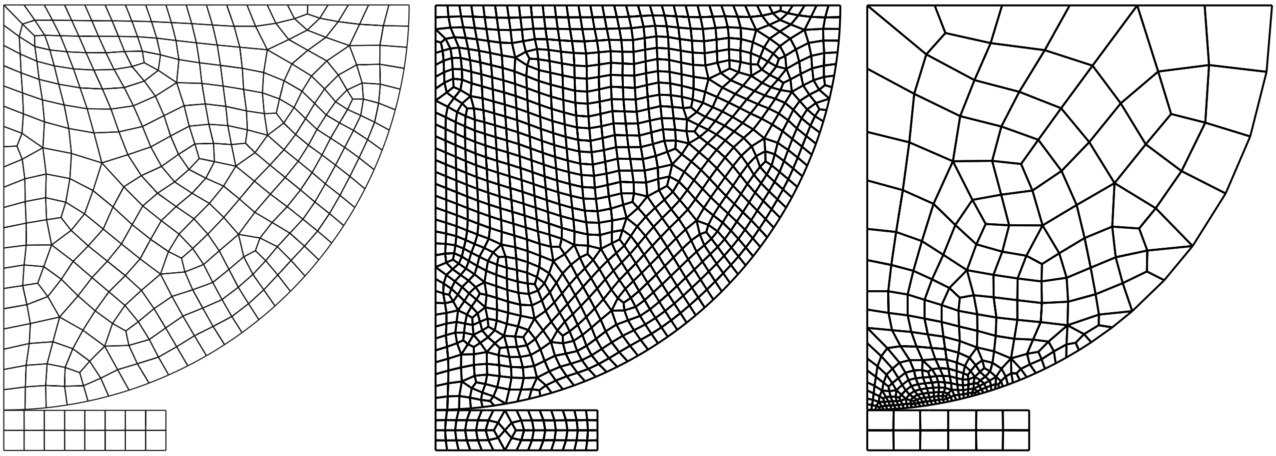

(a) (b) (c)

Figure 5.10: Isoparametric elements with a polynomial degree of one for a mesh with (a) 335, (b) 995 quasi-uniform distributed, and (c) a priori locally refined 315 elements.

---

[2] It should be noted that the plotted contact pressure distribution is derived in the regular post processing step from the solution vector $\mathbf{U}$ and hence results from the strains. It is not showing the distribution of the penalty force, representing the contact stresses which are applied during the computation.

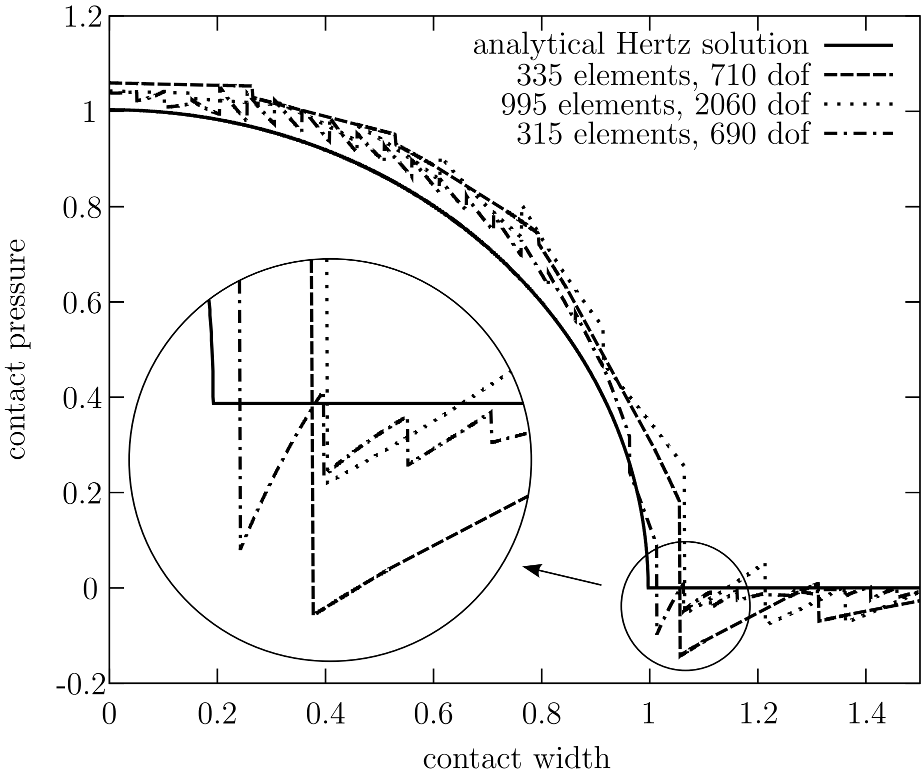

Figure 5.11: Contact pressure for the typical h-version of the FEM using isoparametric elements with linear shape functions.

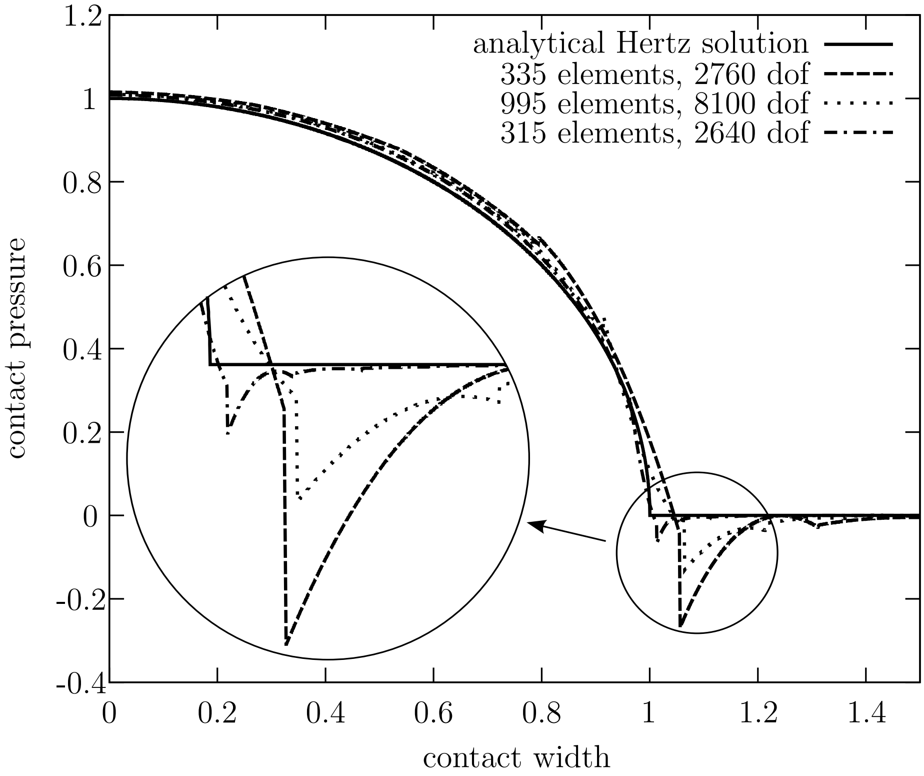

Figure 5.12: Contact pressure for the typical h-version of the FEM using isoparametric elements with quadratic shape functions.

The computations for a polynomial degree of two are performed on virtually the same meshes as used for $p = 1$ given in Figure 5.10. Due to the isoparametric concept that is usually applied for low order Finite Elements, the geometric representation of the circle is changed from a linear to quadratic polynomial for each element though. The corresponding contact pressure distributions in the contact interface are plotted in Figure 5.12. The most accurate results are obtained using the locally refined mesh (c) with 315 elements. Generally a much smoother and better approximation of the Hertz solution in the contact interface is obtained using quadratic isoparametric elements (compared to the linear isoparametric element description). No jumps in the contact interface can be observed at the Finite Element nodes. Looking at the end of the contact interface around Γ_*, a large error especially for the coarse mesh shown in Figure 5.10(a) occurs. For this mesh the error is even bigger than for the same example mesh using isoparametric linear elements (Figure 5.11). This overshooting behavior derives from the fact that the polynomial of second order has a point with reduced regularity in its interior domain. Naturally a smooth polynomial function is not able to represent the point with reduced regularity in the solution and therefore starts to oscillate. It is also visible that the influence area of the oscillation reduces, the closer the FE node is to the correct end of the contact interface Γ_*. This example also shows that for a given polynomial ansatz of the shape functions, a fine discretization of the mesh in the contact region is advantageous against a coarse discretization since the error in the pressure distribution due to not matching the end point of the contact interface is reduced drastically.

5.2.3.2 Contact Stresses for the *p*-Version of the FEM

The *p*-version of the Finite Element Method is characterized by coarse meshes as given in Figure 5.13(a). The geometric representation of the circular edge is obtained by using the blending function method as described in Section 2.2.4 (see [34, 35]). It should be noted that Figure 5.13(a) is a mesh that is modeled in such a way that element number one (bottom left) is mostly but not completely in contact. The element width is approximately 26% wider

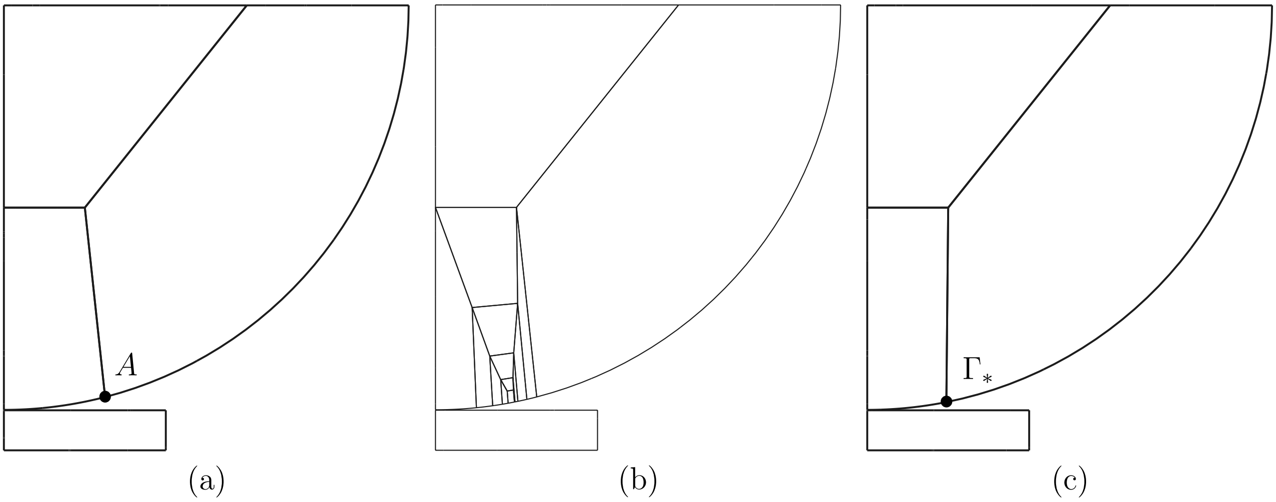

Figure 5.13: (a) 4 element mesh for *p*-version (including one element for modeling the rigid foundation); (b) final mesh for *hp*-version; (c) 4 element mesh after performing the iterative *rp*-version of the FEM.

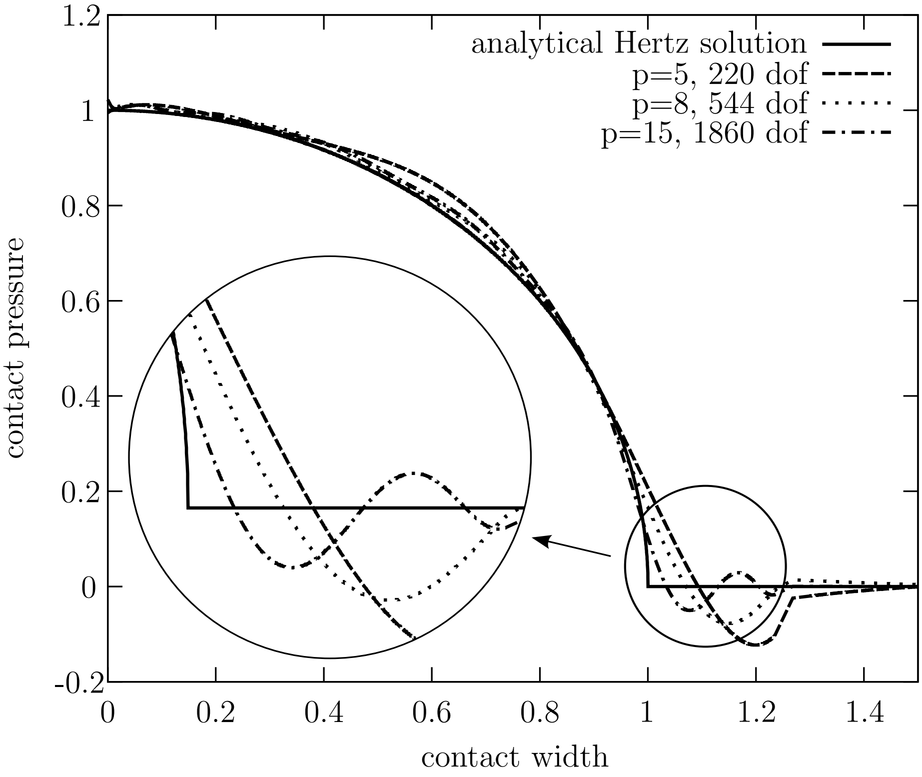

Figure 5.14: Contact pressure for three different polynomial degrees (pure p-refinement) on mesh 5.13(a) where the contact width does not coincide with the elements width.

than the contact interface. Node A in Figure 5.13(a) is therefore significantly off the contact interface. Thus the element experiences a change in boundary condition along one edge. Figure 5.14 shows the contact pressure distribution for mesh 5.13(a) for the three different polynomial degrees $p = 5$, $p = 8$, and $p = 15$. Due to the fact that for this mesh the end of the element does not coincide with the end of the contact interface at Γ_*, oscillations can be observed in the pressure distributions [26]. This effect is similar as already observed and discussed for the isoparametric elements with quadratic shape functions (Figure 5.12). Figure 5.14 shows that the amplitude of the oscillations reduces when the shape function's polynomial degree is increased. A higher polynomial order yet increases the frequency of the oscillations. For the curve of $p = 15$ the higher order oscillation is clearly visible. The oscillations are again due to the loss of regularity of the exact solution at the end of the contact interface which cannot be precisely represented by higher order polynomials, spanning this region.

5.2.3.3 Contact Stresses for the *hp*-Version of the FEM

Figure 5.13(b) depicts the final mesh which is used for the computation with the *hp*-version of the FEM (see Section 4.7). The mesh is generated iteratively by using a four element mesh as the starting mesh. After one FEM computation, the end point Γ_* of the contact interface is estimated and the mesh is refined towards this estimated point in a *hp*-manner. A constant progression factor of 0.5 is used for each refinement step, following [15]. This refinement procedure is applied four times to arrive at the mesh depicted in Figure 5.13(b). The point with reduced regularity given by Γ_* lies on the edge of the innermost element.

The contact pressure curves for three different refinement steps are given in Figure 5.15. It plots the pressure distribution for a constant polynomial degree of $p = 8$ on geometrically refined meshes. From this it is obvious that a refinement toward the contact interface point Γ_* decreases the error of the approximation significantly.

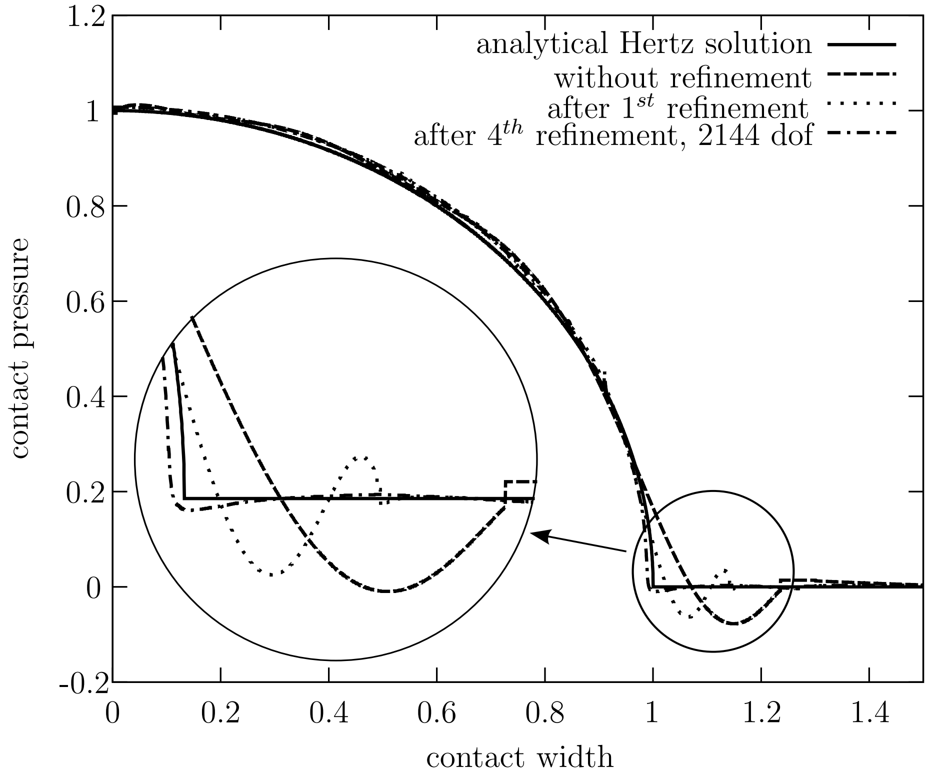

Figure 5.15: Contact pressure with a constant polynomial degree of $p = 8$ on different geometrically refined meshes. Starting with the initial mesh 5.13(a) to derive at mesh 5.13(b) after four refinement steps.

When the full adaptive *hp*-scheme is applied as pictured in Figure 4.12, a slightly different result is obtained for the pressure distribution plotted in Figure 5.16. The initial mesh for the adaptive *hp*-refinement is shown in Figure 5.33(a). The results are plotted for the first, second, fourth, and eighth refinement step. Following the adaptive *hp*-scheme, an element with polynomial degree of one is used in the area at the end of the contact interface around Γ_*. Due to this, a relatively poor representation of the stresses is achieved in the smallest element. The geometric refinement towards this point needs to be performed eight times in order to obtain a thorough and reliable result.

5.2.3.4 Contact Stresses for the *rp*-Version of the FEM

When the *rp*-version of the FEM is used to compute the Hertzian contact problem, very accurate results can be obtained for the contact stresses. The distribution of the contact stresses matches Hertzian's solution quite well for the case when the ends of the contact interface coincides with Finite Element nodes [27]. The final iterated four element mesh is shown in Figure 5.13(c). The corresponding contact pressure distributions for polynomial order of five, eight and fifteen respectively are plotted in Figure 5.17. The FE computation

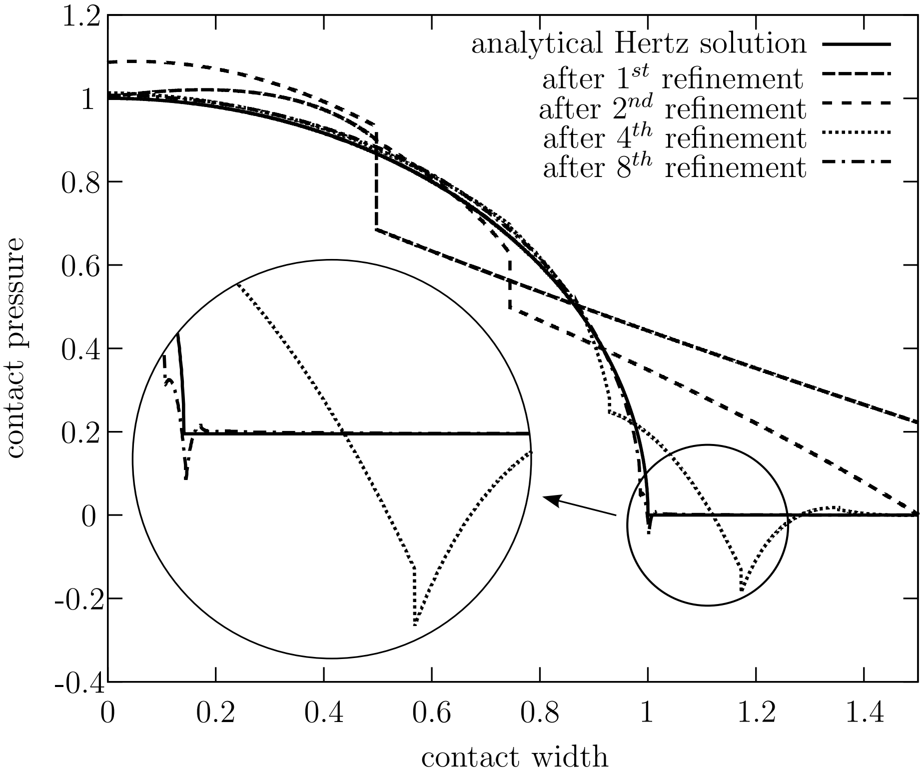

Figure 5.16: Contact pressure for different refinement steps of the adaptive *hp*-method. Starting with the mesh given in Figure 5.33(a), and refining it in a *hp*-manner as shown in Figure 5.33(c) after four refinement steps.

has to be performed several times in an iterative process until the location of Γ_* coincides with a Finite Element node. The number of iterations which is needed to obtain the final mesh differs depending on the chosen polynomial order and geometric discretization. With higher polynomial orders, the end point Γ_* of the contact interface is approximated better, already after the first computation. Therefore less iterations are needed to relocate the mesh in a way that Γ_* coincides with a Finite Element node. Obviously, very good results can be obtained when the *rp*-version is applied. Oscillations of the shape functions are avoided by placing a Finite Element node at the end of the contact interface at Γ_*, where a reduced regularity exists. This in combination with a smooth geometric description and a high polynomial degree leads to very accurate and smooth stress distributions in the contact interface. Interestingly it seems that the more accurate the numerical results become, the more does the contact width differ from the analytical Hertz solution and converge to a different solution. The same effect, can as well be observed in the previously shown results for the computations with constant polynomial degree on geometrically refined meshes and for the *hp*-method. This matter will be further discussed in the following.

The iteration process and hence convergence of the automatic relocation algorithm for the four element mesh of Figure 5.13(a) and a polynomial degree of five is visible in Figure 5.18. Apparently the algorithm works well and converges to the correct contact interface. The geometrical offset of the closest FE-node to the location of Γ_* has in the first iteration a value of 26% to the right with respect to the analytical contact width. After 20 iterations a very good match of the contact interface point Γ_* and the closest FEM node is found. The

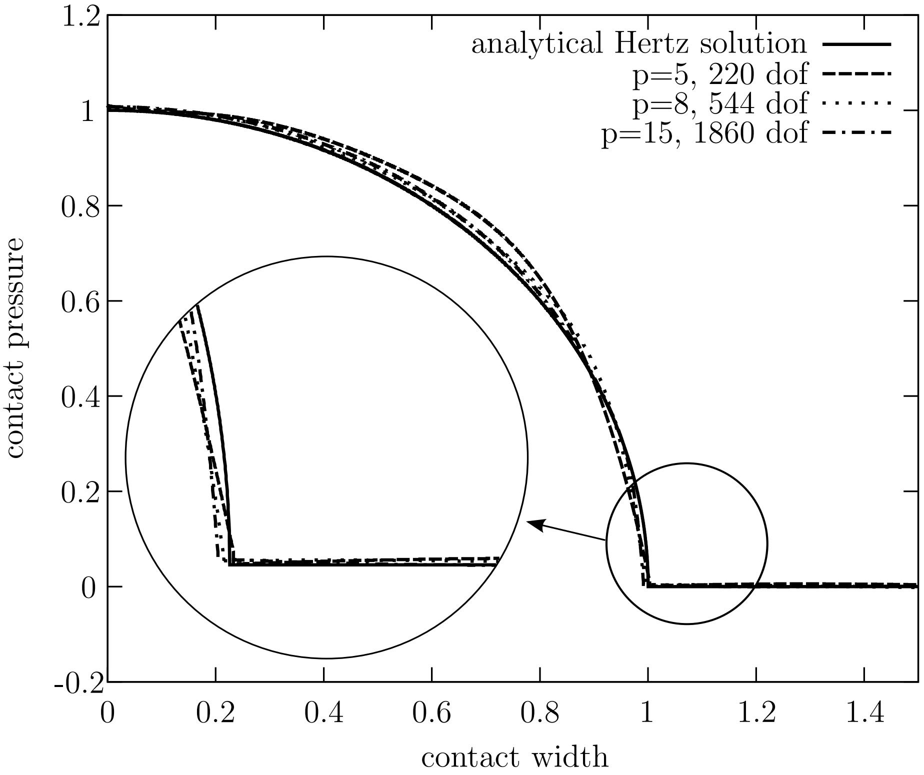

Figure 5.17: Contact pressure for three different polynomial degrees by using the *rp*-version of the FEM on a mesh shown in Figure 5.13(c).

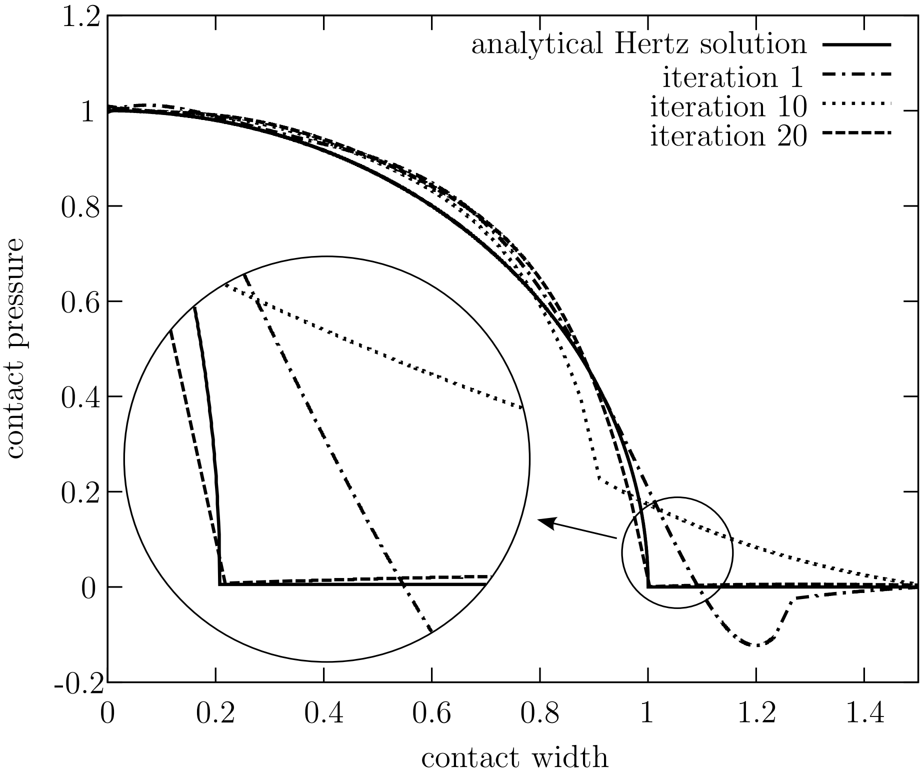

Figure 5.18: Contact pressure: three solutions during the *rp*-iteration process for the four element mesh and a constant polynomial degree of $p = 5$.

computational time needed for each iteration is seventeen seconds[3].

It is already stated above, that the numerical results do not match the Hertzian solution exactly. Especially the fact that the contact width in the numeric solution tends to converge to a smaller value than the one predicted by Hertz provokes further studies. Attention is drawn to the assumptions made by Hertz, especially the geometric simplification in the contact interface of using a polynomial of second order to represent the cylinder's circular shape. Tests are performed using Shtayerman's theory which allows to use the exact circular geometry and therefore the same geometry which is used in the numeric computation. A comparison of the two analytical solutions from Hertz and Shtayerman is given in Figure 5.19 where the equivalent contact stress distributions are plotted. Besides minor differences between the two curves, it can be observed, that the contact width of the Shtayerman solution (red dotted line) is slightly smaller than for the Hertzian solution. Comparing the best results shown previously (*rp*-method, p=15 and constant p=8 on geometrically refined meshes) with the analytical Shtayerman solution, a far better match of the contact width can be observed (Figure 5.20). The effect is interesting and worth to be mentioned, even though it should be stated, that in the present example, a contact width of nearly 20% of the radius is present. This could violate Hertz's assumption that the contact interface is small compared to the cylinders radius.

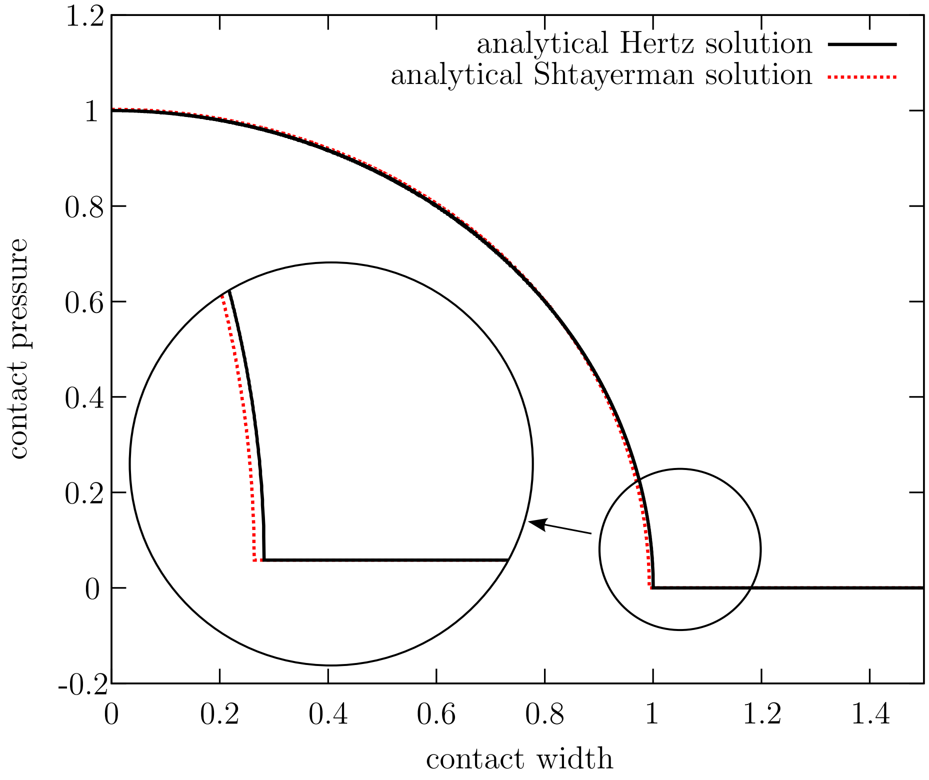

Figure 5.19: Contact pressure: comparison of the analytical Hertz and Shtayerman solution.

A comparison of the different results apart from the previously shown contact stress distribution is given in Table 5.1. It plots the degrees of freedom, calculation times, and error of the

---

[3] on an Intel Core 2 Quad CPU Q6600, 2,4GHz

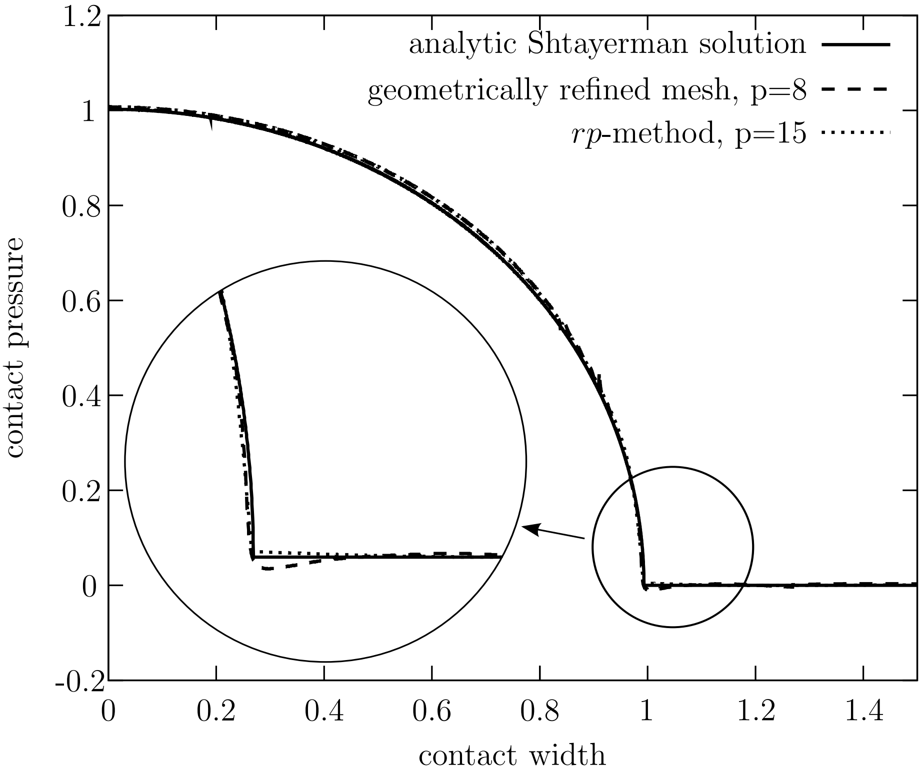

Figure 5.20: Contact pressure: Shtayerman solution plotted against the best results obtained for the rp-method and for $p = 8$ on geometrically refined meshes.

stresses in L^2-norm for each previously discussed discretization.

$$\|e_\sigma\|_{L^2} = \frac{\sqrt{\int_0^{1.5b} (\sigma_{Hertz} - \sigma_{FE})^2 \, dx}}{\int_0^{1.5b} \sigma_{Hertz} \, dx} \cdot 100 \; [\%] \tag{5.11}$$

The error in L^2-norm gives the error in the contact pressure between Hertz's or Shtayerman's analytical and the corresponding discretized solution respectively. To account for the oscillations outside of the contact interface, the L^2-norm is calculated up to a width of $1.5 \cdot b$. The error value is scaled by the analytical value for the contact pressure and multiplied with 100 and therefore given in percent.

The results for the bilateral Hertzian contact problem are generally the same as for the unilateral problem. For the case of contact between two equally sized cylinders with the same material parameters, the result is identical to the case of contact between a cylinder and a rigid plate discussed in the previous section. As specified in Section 3.6, in the present approach no conventional master-slave concept is applied in the bilateral contact interface. The gap function is derived in each iteration step for each boundary separately, giving no preference to either of the bodies. The result is a smooth and continuous contact boundary where each point on both boundaries satisfies the contact constraints (neglecting the error due to the penalty method). The vertical stresses for the bilateral model are plotted in Figure 5.21.
For the sake of completeness, all components of the stress distributions are plotted for the unilateral Hertzian contact problem in Figures 5.22 - 5.25.

discretization		deg. of freedom	calculation time [sec]	error in L^2-norm [%] compared	
				to Hertz	to Shtayerman
p=1	335 elements	710	87	6.5511	24.0830
	995 elements	2060	512	0.2285	0.2338
	315 elements	690	240	0.1022	0.1026
p=2	335 elements	2760	173	0.1316	0.1355
	995 elements	8100	896	0.0693	0.0706
	315 elements	2640	400	0.0331	0.0265
p=5	4 elements	220	17	0.1708	0.1738
p=8	4 elements	544	132	0.1050	0.1085
p=15	4 elements	1860	2945	0.0415	0.0420
rp=5	4 elements	220	17	0.0633	0.0547
rp=8	4 elements	544	132	0.0397	0.0301
rp=15	4 elements	1860	2945	0.0337	0.0207
p=8	locally refined mesh	2144	1069	0.0488	0.0317

Table 5.1: Discretization, degrees of freedom, calculation time, and error in L^2-norm for each model compared to the Hertzian and Shtayerman reference solution.

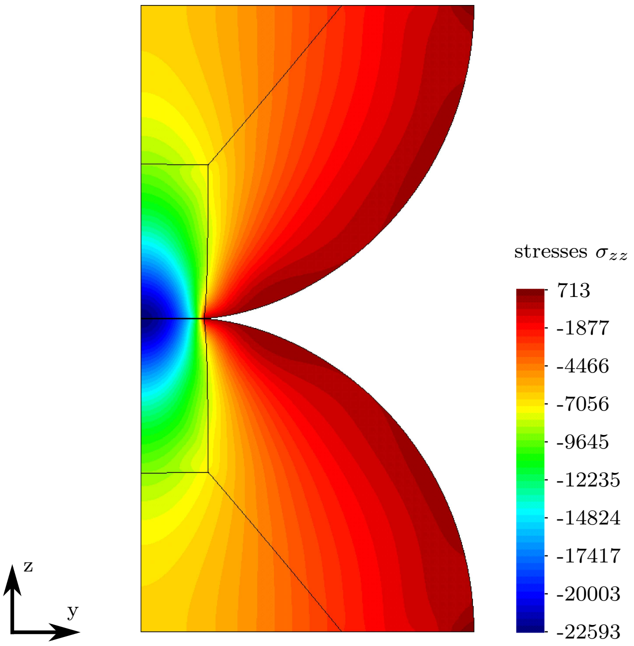

Figure 5.21: Bilateral Hertian contact using six elements and *rp*=6.

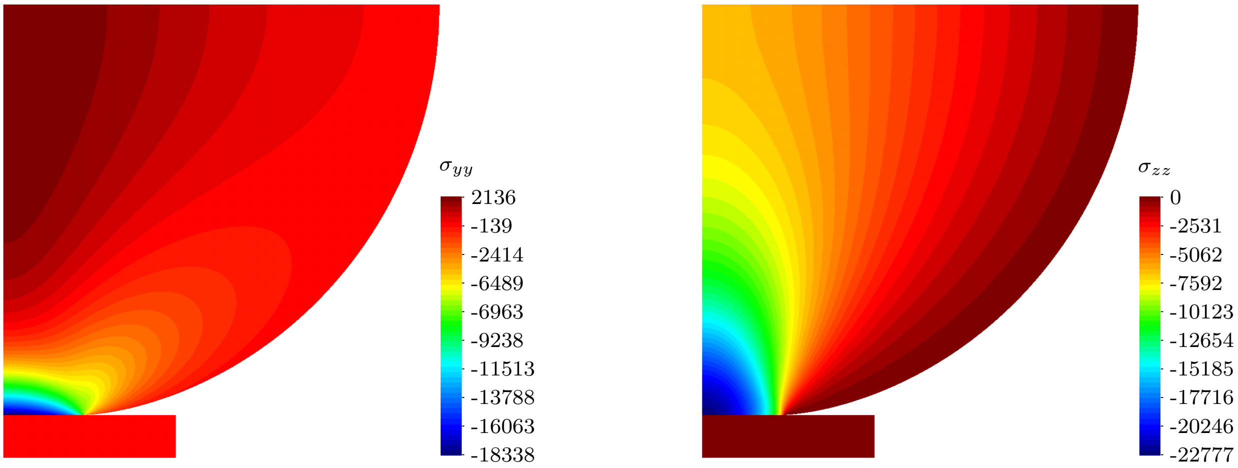

(a) (b)

Figure 5.22: Stresses σ_{yy} and σ_{zz} given in $[\frac{N}{mm^2}]$.

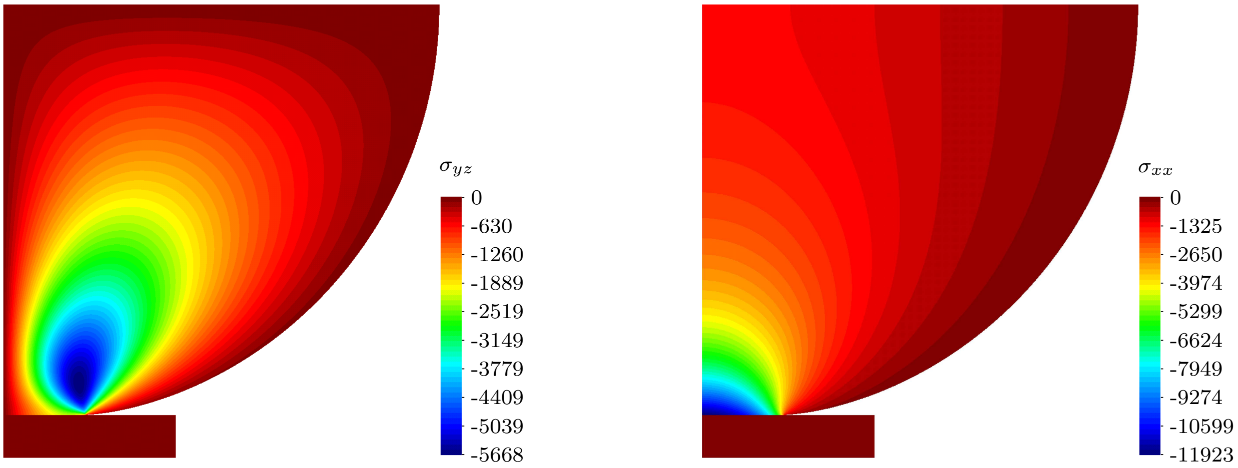

(a) (b)

Figure 5.23: Shear stresses σ_{yz} and stresses along the cylinder's axis σ_{xx} given in $[\frac{N}{mm^2}]$.

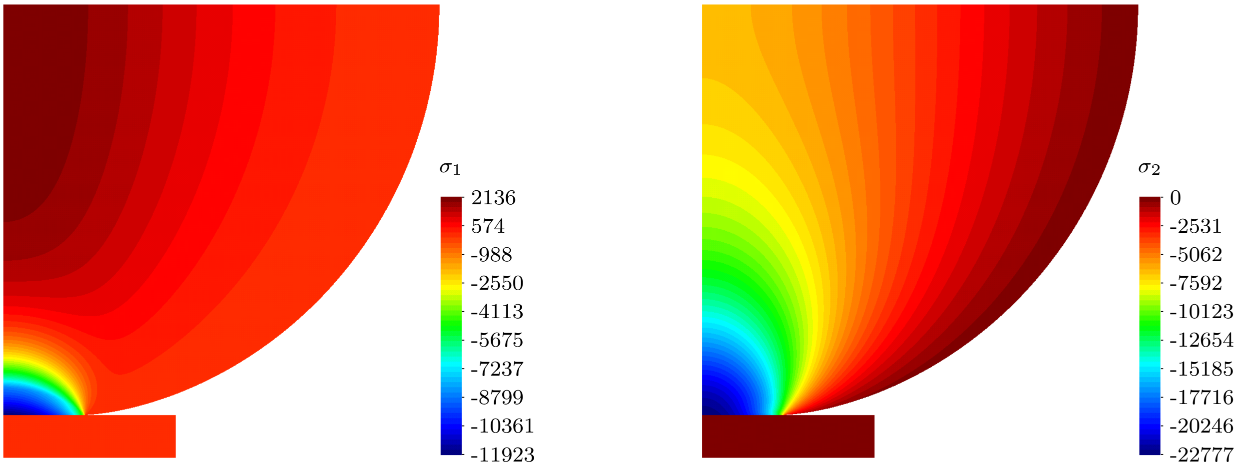

(a) (b)

Figure 5.24: Principal stresses σ_1 and σ_2 given in $[\frac{N}{mm^2}]$.

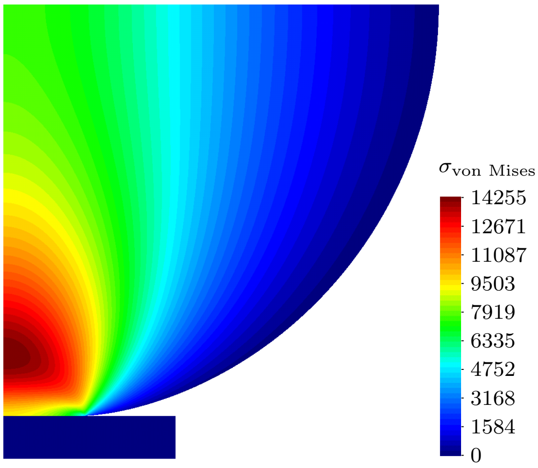

Figure 5.25: Von Mises stresses $\sigma_{\text{von Mises}}$.

5.2.4 Convergence of the error in energy norm for the unilateral Hertzian contact problem

An introduction into the theory of error estimation was given in Section 4.2. Different convergence properties were presented and discussed. Algebraic convergence rates are typical for low order Finite Element Methods and problems of nonlinear nature approximated by the *p*-version of the FEM. Uniform high-order Finite Element Methods have the potential to show exponential rates of convergence, but generally only for the case of smooth problem types. The application of the *hp*-version allows to obtain exponential rates of convergence even for problems including singularities. In [60] it was furthermore shown that exponential rates of convergence can also be obtained for solutions with singularities, like elastoplastic problems by making use of the *rp*-version of the FEM.

According to Schumann [70] and Schröder [69], the contact problem is at most C^2 regular. It was shown and discussed in Section 4.5, that a point singularity exists at the end of the contact interface in the contact interface point Γ_*. A change from a contact boundary condition to a non-contact boundary condition is present in this point. The behavior is similar to a change from Neumann boundary condition to a free boundary condition.

Studies by Paczelt et al. [61] were performed on an example similar to the Hertzian contact problem. The bottom object was rigid and flat and the top object was curved with a given parabolic boundary representation. The *rp*-version of the FEM was applied for this example as well. The convergence of the error in energy norm was plotted in logarithmic scale and seen to be of algebraic type. Further studies on the convergence rates were performed by Baksa [5] for the *h*-, *p*-, *hp*-, and the *rp*-method.

Besides all the different methods which are applied in the present study, a big problem is to obtain a good and reliable reference solution for the Hertzian strain energy. Hertz does not supply an analytic reference solution for the strain energy because he only considered the contact interface in his studies and did not take the rest of his object into account. Therefore no closed solution exists describing the stresses or strains throughout the whole cylindrical body. Numerical models suffer from the fact of the point singularity at the end of the contact interface at Γ_*.

In the present study, the reference solution is obtained by applying the adaptive *hp*-method with eight refinement steps towards the end of the contact interface, starting with the mesh shown in Figure 5.33(a). The maximal polynomial degree used in this computation of the reference solution is therefore of order ten, with decreasing polynomial order advancing the singularity at the end of the contact interface (see Figure 4.12 for a schematic sketch of the adaptive *hp*-FEM). For this model, a strain energy of 7754.057 $[\frac{N}{mm^2}]$ is derived which is used as a reference solution in the following studies.

Convergence studies are performed for the *h*-, *p*-, *rp*-, and *hp*-version of the Finite Element Method. The respective results are shown and discussed in the following sections.

5.2.4.1 Convergence Rates for *h*-Version of the FEM

The convergence rates for the unilateral Hertzian contact problem with pure *h*-refinement (global mesh refinement) is plotted in Figure 5.26. The meshes are unstructured quadrilateral meshes with isoparametric ansatz spaces similar as the meshes plotted in Figure 5.10. The meshes are non-adaptive and do not use a priori or a posteriori informations to optimize the element size in the contact region. Polynomial orders of $p = 1$ and $p = 2$ are studied here. The rate of convergence is of algebraic nature, where the slope of the curve as a measure for the convergence rate is $\beta \approx 0.5$ for $p = 1$ and $\beta \approx 0.8$ for $p = 2$.

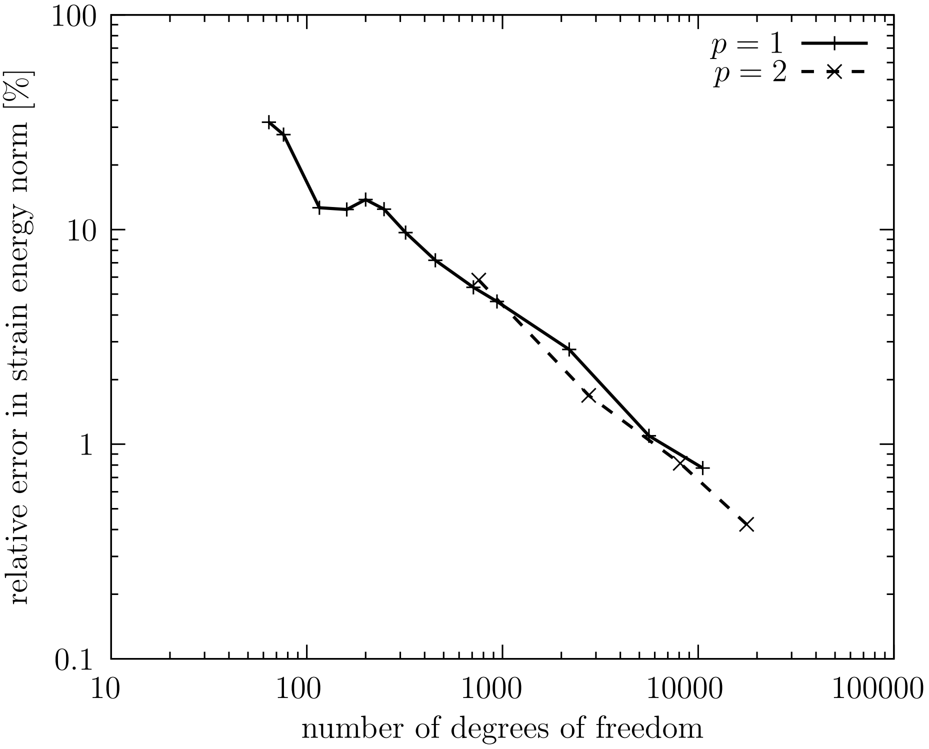

Figure 5.26: Algebraic convergence rate of relative error in energy norm for the Hertzian contact problem computed with isoparametric element formulations with polynomial orders of $p = 1$ and $p = 2$.

5.2.4.2 Convergence Rates for p-Version of the FEM

The rate of convergence for a pure p-refinement, without special treatment of the end of the contact interface, is plotted for the four element mesh (Figure 5.13(a)) in Figure 5.27. The Finite Element node A in Figure 5.13(a) does not coincide with the end of the contact interface Γ_*. It is approximatively 26% further to the right than the contact interface point Γ_*. For this kind of mesh the rate of convergence is seen to be of algebraic type with a gradient of $\beta \approx 1.0$. From the comparison of the two Figures 5.26 and 5.27 it can clearly be seen that for a relative error in strain energy norm of less than 1% approximately 6500 degrees of freedom (DOF) are needed in the h-version, but only around 900 DOF in the p-version.

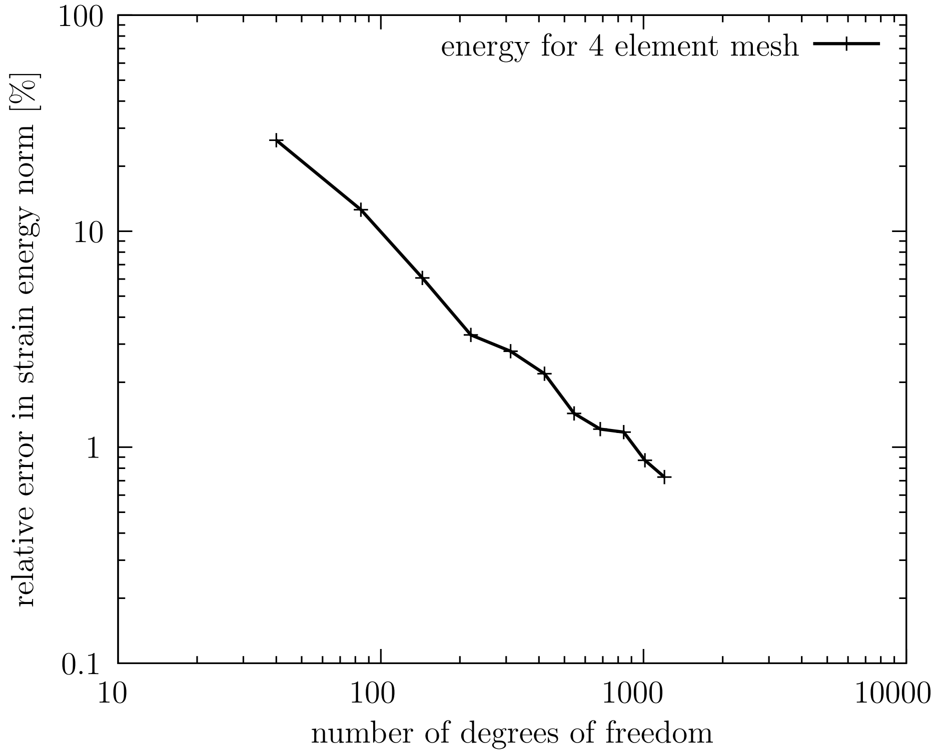

Figure 5.27: Algebraic convergence rate of relative error in energy norm for the Hertzian contact problem computed with the four element mesh given in Figure 5.13(a) and polynomial orders ranging from $p = 2$ to $p = 12$.

Referring to the studies shown in Section 4.4 for the plate with a hole, the error in the von Mises stresses is studied for the unilateral Hertzian problem as well. Here again, the difference in the von Mises stresses for $p = 10$ and $p = 20$ is investigated and plotted in Figure 5.28. It indicates the location of error sources like singularities, occurring in the domain. As before, the legend in Figure 5.28 is scaled to show the range from zero to the maximal value of about 0.1% of the maximal von Mises stress occurring in the reference model (eight hp-refinement steps on initially four element mesh with $p = 20$). It can well be seen that the main error is induced in the bottom left element which is only partly in contact. The oscillations of this element are in an order of magnitude that it is influencing the neighboring element as well.

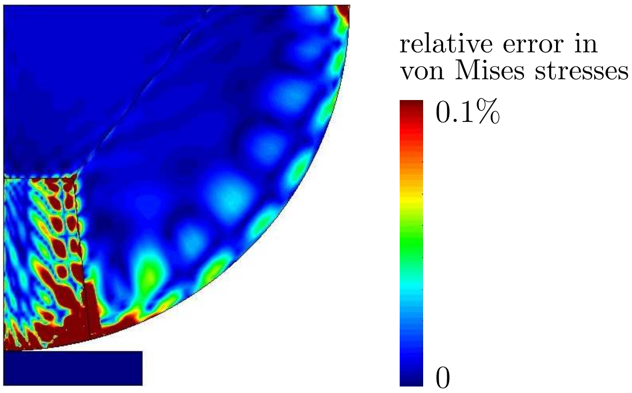

Figure 5.28: Relative error in von Mises stresses for the 4 element mesh shown in Figure 5.13(a) by applying the p-version of the FEM. The maximal value in the legend shows 0.1% of the maximal von Mises stress occurring in the reference model.

5.2.4.3 Convergence Rates for *rp*-Version of the FEM

Judging from the quality of the stress distribution plots shown in the previous section, a high accuracy and rate of convergence in energy norm is expected for the rp-version of the FEM. In order to resolve the $C^{1+\alpha}$ continuity at the end of the contact interface at Γ_*, it should be sufficient to have this point Γ_* coincide with a Finite Element node. Thus making use of the C^0 continuous property of the Finite Element solution at nodes and edges. Unfortunately the continuous, but reduced differentiability at Γ_* continues into the domain surrounding Γ_*. In order to resolve this with an appropriate discretization, knowledge about the direction of the 'vault line' is required. This is unfortunately not the case for general geometries and load directions.

The effect of a contact pressure acting on a defined part of a boundary is first tested in a simplified test case.

5.2.4.3.1 A Simplified Test Example

As a test case for the given boundary condition in the contact example, a geometry very similar to the Hertzian problem is chosen. Here only the quarter circle is calculated as in the original example, but no contact takes place. Instead, a triangular load is applied on the contact boundary, as a simplification of the parabolic Hertzian load distribution. Symmetry boundary conditions are applied at the left and top boundary. The rest of the parameters is chosen as for the Hertzian contact example given in the previous section. The example is studied since the boundary conditions are fixed and known a priori. No iteration of the end of the contact interface (Γ_*) is necessary, because the load is applied on a specified area. The reference solution is obtained by the extrapolation method presented in Section 4.9 for the respective meshes.

The convergence of the error in energy norm is plotted for the two meshes given in Figure 5.29 with polynomial orders between p=2 and p=20 in Figure 5.30. The convergence characteristic for this example is of algebraic nature. The slope $\beta \approx 1.75$ for the 3 element mesh and $\beta \approx 1.85$ for the 147 element mesh. Due to the fact that the boundary conditions are known and the deformations and stress distribution is not very complex, the absence of the exponential

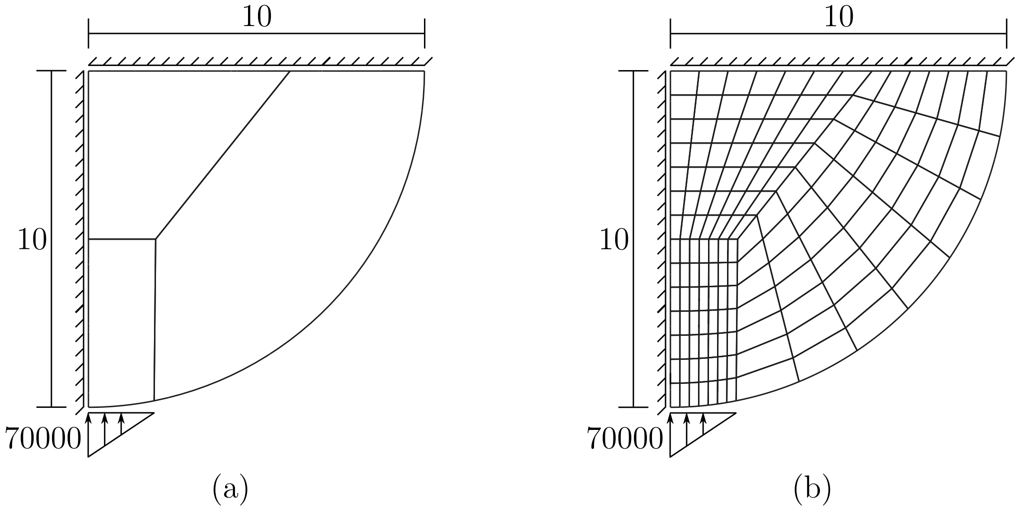

(a) (b)

Figure 5.29: Test case for the convergence in energy of a body with circular boundary and triangular load on a (a) 3 element mesh and a (b) 147 element mesh.

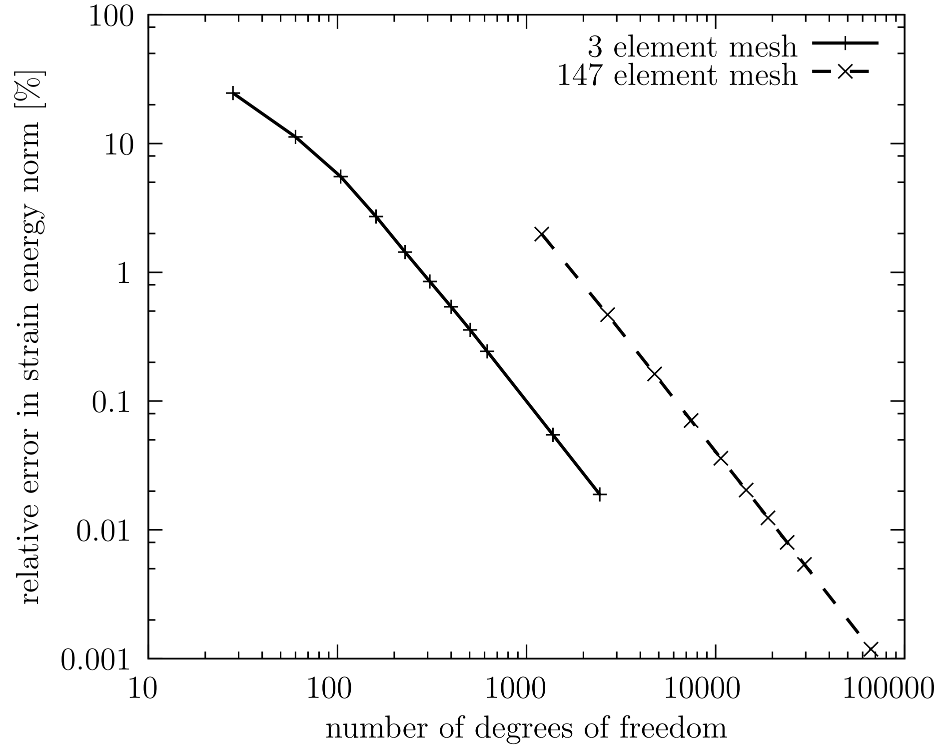

Figure 5.30: Algebraic convergence rate of relative error in energy norm for the simplified Hertzian geometry and load boundary conditions without contact. The plotted graphs show the p-convergence for the three (p=1 to p=20) and 147 element (p=1 to p=15) mesh given in Figure 5.29(a) and (b).

convergence rates results from the reduced regularity at the end of the Neumann boundary.

5.2.4.3.2 Convergence Rates for Hertz Problem with the *rp*-Refinement

After showing the results for the simplified test example of the Hertzian contact problem, convergence studies are performed on various meshes and high polynomial orders. The errors in energy norm derive from computations with meshes which are iterated in such a way that the end of the contact interface Γ_* coincides with a Finite Element node. The meshes are given in Figure 5.13(c) and 5.31. The 36 and 144 element mesh are uniform refinements of the 9 element mesh. The iteration to derive the correct position of Γ_* is performed to a degree that it coincides with the Finite Element node at this position up to the tenth digit of the y-coordinate. The corresponding convergence rates are plotted in Figure 5.32 for each mesh. They are of algebraic type with a negative slope of $\beta \approx 1.4$. A relative error of less than 1% is obtained by a computation with about 550 DOF for the four element mesh. As for the small test example, the reduced regularity at Γ_* controls the slope of the convergence curve and limits it to be of algebraic type. Due to the rather simple deformation and pressure distribution for this geometry and boundary condition, exponential rates are not even visible in the pre-asymptotic range.

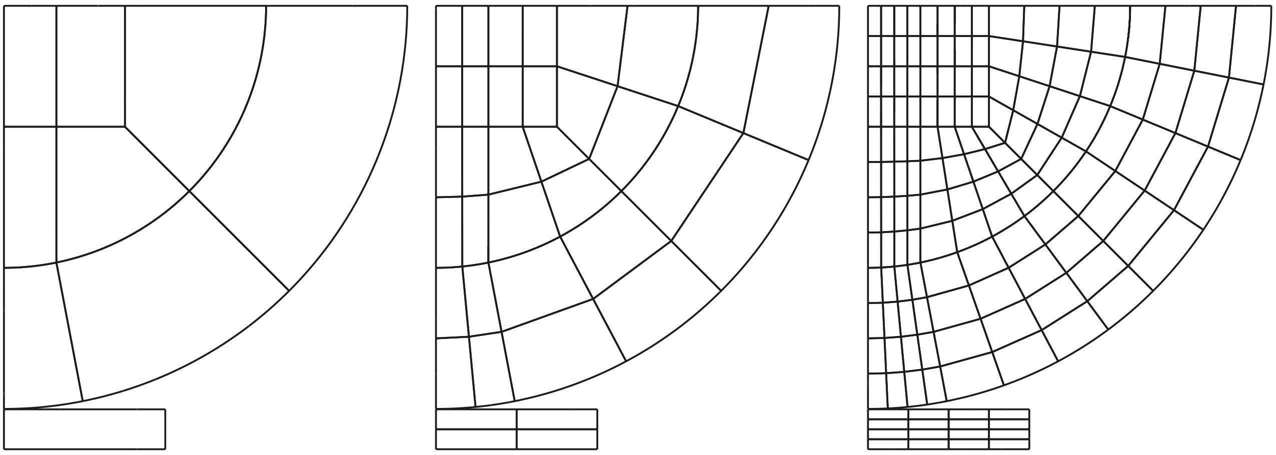
(a) (b) (c)

Figure 5.31: (a) 9 element interface mesh; (b) 36 element interface mesh; (c) 144 element interface mesh for calculation with the p-version of the FEM.

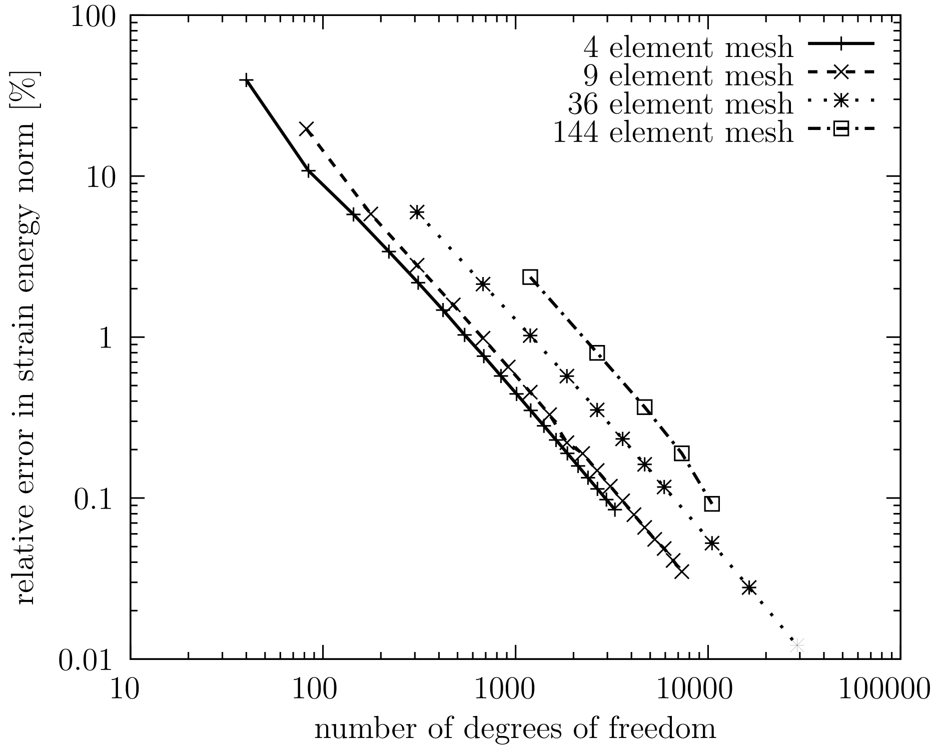

Figure 5.32: Algebraic convergence rate of relative error in energy norm for the Hertzian contact problem in two dimensions computed with the *rp*-version of the FEM on the meshes given in Figure 5.13(c) and Figure 5.31.

5.2.4.4 Convergence Rates for *hp*-Version of the FEM

The computations with the *hp*-method are performed on the initially four element mesh shown in Figure 5.33(a), turning into the 16 element mesh shown in Figure 5.33(c) after four adaptive refinement steps.

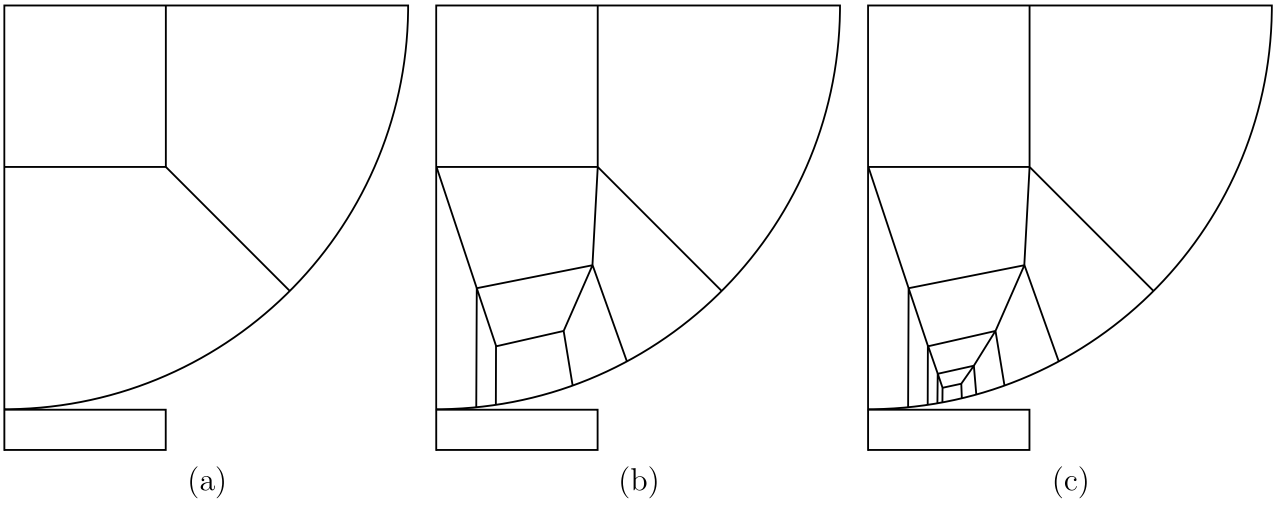
(a) (b) (c)

Figure 5.33: Meshes used for the derivation of the convergence rate of the error in energy norm. Mesh (a): initial mesh, mesh (b): after two *h*-refinements, and mesh (c): after four *h*-refinement steps.

The convergence of the relative error in energy norm for each mesh given in Figure 5.33 (initial mesh and meshes refined twice, and four times) is plotted in Figure 5.34. The dashed curves represent the computations performed with a constant polynomial degree of $p = 2$ to $p = 10$ on geometrically h-refined meshes shown in Figure 5.33. For the computations with constant lower polynomial orders ($p = 2,\ p = 3,\ p = 4$) on h-refined meshes, an asymptotic algebraic rate of convergence is visible. It derives from the poor discretization of the large element with the relatively low polynomial orders which is partly in contact. The rate of convergence for the computations with higher polynomial orders and h-refined mesh, is of exponential nature. The rate of convergence reaches a value of $\beta = 5.5$. The solid line shows the convergence of the error in energy norm for the full hp-scheme. Here, the element having the change in boundary conditions from contact to no contact is always having the minimal polynomial degree of $p_{min} = 1$. For each element further away from the end of the contact interface, the element's polynomial degree is increased by one. The rate of convergence for the computations with the full adaptive hp-scheme, is of exponential nature. The convergence rate is equal to $\beta = 2.7$. Around 750 DOFs are necessary to get an error of less than 1%. It can therefore be assumed that the reduced regularity at the end of the contact interface is sufficiently isolated by the inner element, not causing significant oscillations in the neighboring elements and limiting the influence area by enclosing the singular point.

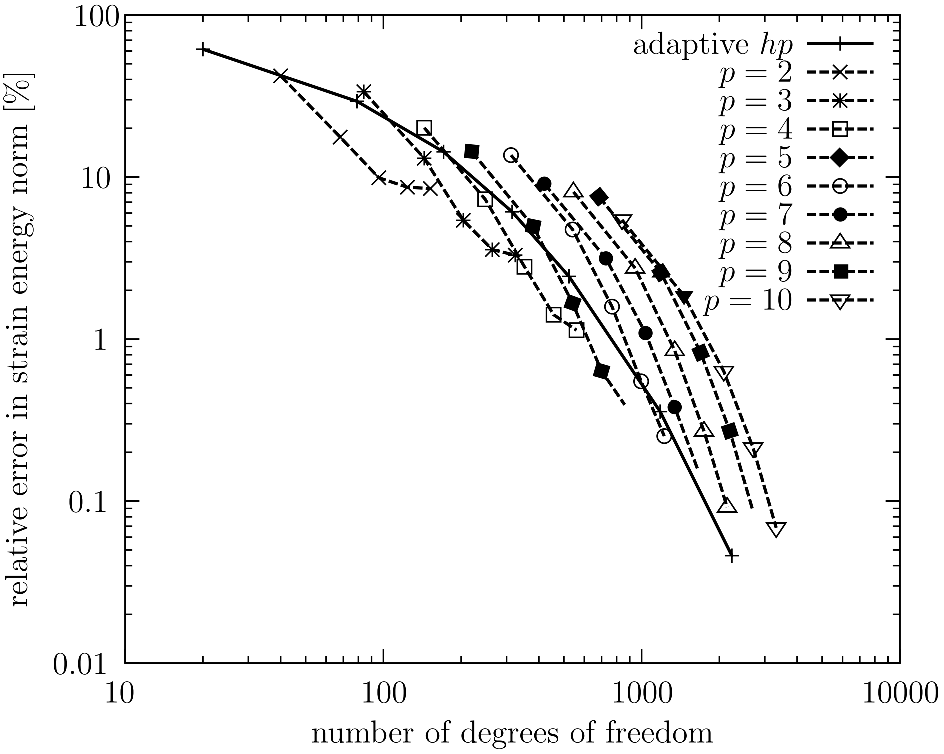

Figure 5.34: Exponential rates of convergence of the relative error in energy norm for the Hertzian contact problem when the hp-method (solid line) is applied. The dashed lines, showing exponential convergence rates as well, represent the computations performed with a constant polynomial degree of $p = 2$ to $p = 10$ on geometrically h-refined meshes shown in Figure 5.33.

The difference in von Mises stresses is studied as well for the *rp*- and *hp*-method of the FEM for the unilateral Hertzian contact problem. The difference in the von Mises stresses for $p = 10$ and $p = 20$ is plotted for the corresponding meshes in Figure 5.35. A large error zone is visible in plot 5.35(b) at the end of the contact interface around Γ_* for the 36 element mesh with the *rp*-adaption applied. The two elements next to it are dominated by this error, which is geometrically limited by the edges of these elements. The checkerboard pattern derives from the polynomial of order ten, which oscillates with small amplitudes compared to the polynomial of order 20. The maximum relative difference in the von Mises stresses for $p = 10$ and $p = 20$ is about seven percent and located at the end of the contact interface at point Γ_*. The four element mesh shown in Figure 5.35(a) behaves much worse. Due to its very large elements, basically the whole domain is affected by the error which is introduced at the end of the contact interface. It is also interesting to see, that the error travels through the whole large curved element even up to the upper right corner of the model, which could already be seen in the studies of the Neumann boundary condition in Section 4.5 for the rectangular load cases. Even though Figure 5.35(a) looks tremendously flawed one should keep in mind that the red color is indicating the area with more than only 0.1% of the maximal von Mises stress occurring for this model. The maximal difference in the von Mises stresses for this model is around fifteen percent, located in the singular point Γ_* at the end of the contact interface.

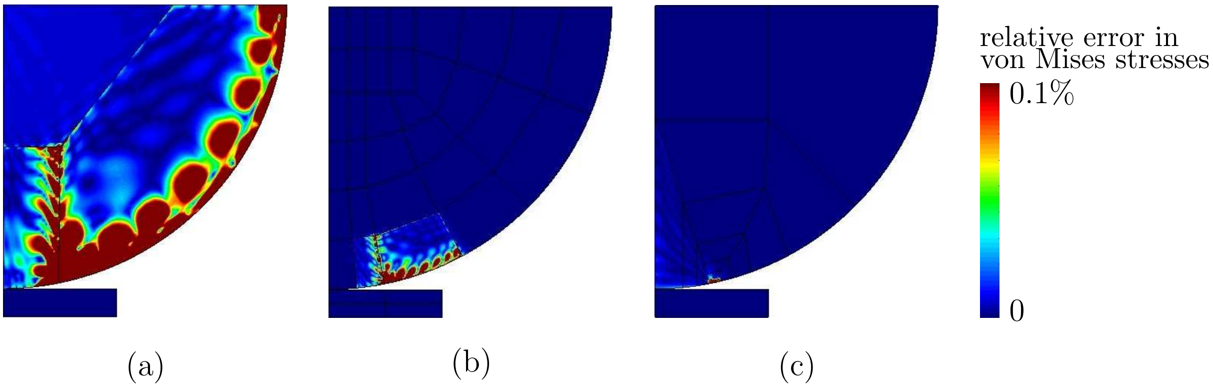

Figure 5.35: Relative error in von Mises stresses for the 4 and 36 element mesh by applying the *rp*-version of the FEM shown in Figure 5.31(a) and (b) and for the 18 element mesh derived by the *h*-refinement and shown in Figure 5.33(c). The label on the right is scaled to a maximum value of 0.1% of the maximal von Mises stresses occuring in the reference solution (max. value in reference solution: 14253).

The zone of the error in the von Mises stresses plotted in Figure 5.35(c) for the four times *h*-refined model is geometrically limited by the smallest element, framing the end of the contact interface. The error, or largest difference between $p = 10$ and $p = 20$ on this mesh is approximately ten percent of the von Mises stresses in the reference solution. Its value is therefore larger than for the (*rp*-adapted) 36 element mesh shown in Figure 5.35(b), but more limited in space extension, therefore affecting the solution more locally than the 36 element mesh.

Contrary to the statement of Eck et al. given in Section 4.4 that there will not be a singularity at this point for the Signorini type problem, clear hints for a stress concentration (or singularity) can be identified in the numerical result.

In order to compare the convergence rates and show the performance of the four presented discretization schemes, Figure 5.36 plots the convergence rates for the h-version with $p = 1$, p-, and rp-version for the four element mesh, and for the adaptive hp-version of the FEM. It is clearly visible, that the convergence rate of the h-FEM is much slower than for every other (p-FEM) method.

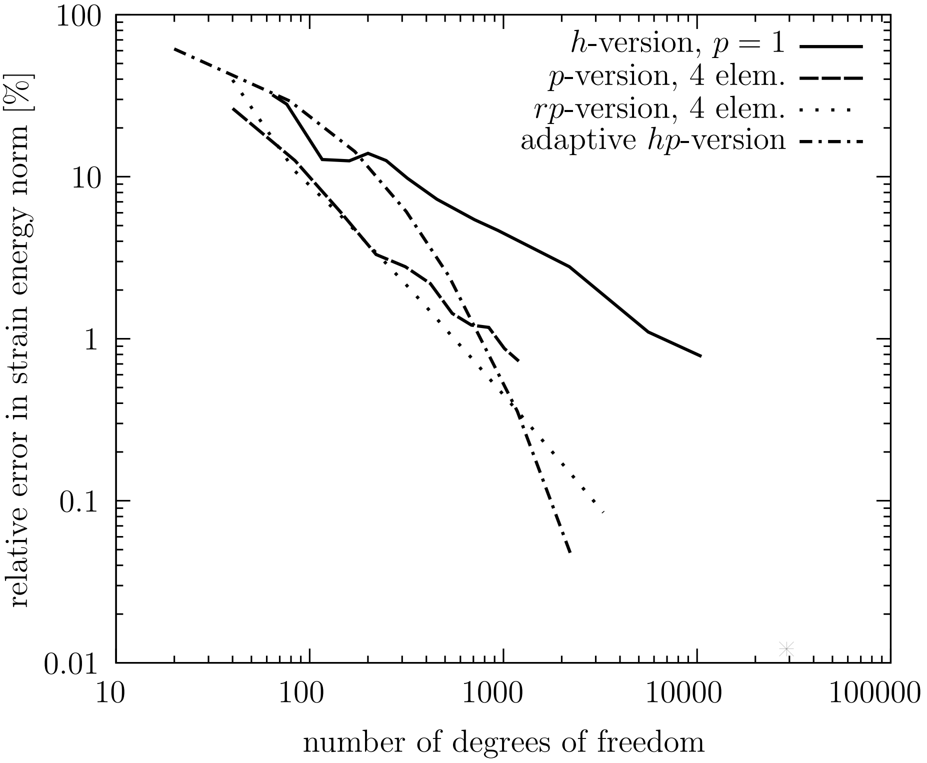

Figure 5.36: Rate of convergence of the relative error in energy norm for the Hertzian contact problem in two dimensions for the h-version with $p = 1$, p-, and rp-version for the four element mesh, and for the adaptive hp-version of the FEM.

5.3 Contact of an Elastic Ring with a Rigid Foundation

We consider a numerical example which has been presented by Fischer [23]. It is in several ways more complex than the Hertzian contact problem. Besides the nonlinearity introduced by the contact problem, the shell like structure undergoes large deformations and exhibits a nonlinear material behavior. Even when taking advantage of the symmetry, in the rp-version approach the positions of two FE-nodes have to be controlled to coincide with the end of the contact interface in order to obtain an accurate approximation. The problem setup is as follows: An elastic ring is in contact with a rigid foundation. The structure consists of an outer and an inner ring both having the same thickness $t = 5[mm]$ but different material properties. The stiffness of the inner ring is 100 times higher than the stiffness of the outer ring. A Neo-Hooke material law is assumed. The mesh which discretizes the ring with only twelve elements is displayed in Figure 5.37. Contrary to the initial setup used in [23], the

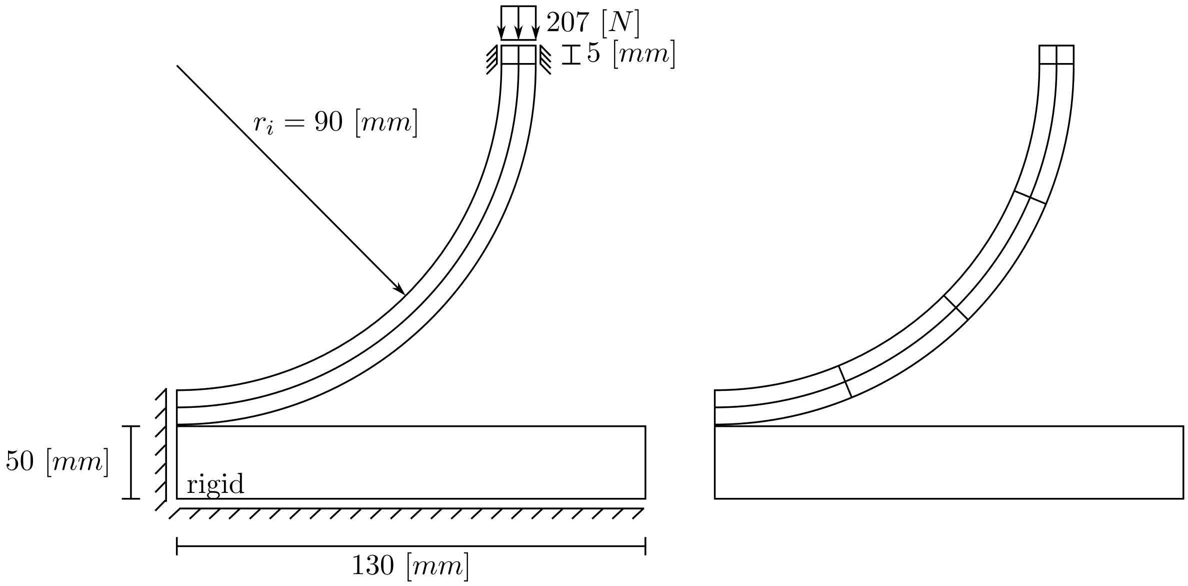

Figure 5.37: Geometric setup, loads and mesh for a composite elastic ring in contact with a rigid foundation.

displacement boundary condition is replaced by a Neumann boundary condition[4] acting in vertical direction, see Figure 5.37. To obtain a similar deformation pattern as in [23], the traction is applied on a stiff strip which has a high Young's modulus of $E = 10^7[N/mm^2]$. In addition to this, the deformation of the strip is constrained in horizontal direction. The cylindrical Arclength Method [13] is utilized in this computation. The penalty parameter equals $\epsilon_N = 10^6[N/mm^2]$, and a polynomial degree of $p = 5$ is chosen for the ansatz space of the quadrilateral elements. The material parameters are as follows:

inner ring:	outer ring:
$E = 10^5[N/mm^2]$	$E = 10^3[N/mm^2]$
$\nu = 0.3$	$\nu = 0.3$

Due to the applied load, a maximum displacement of 35.28 [mm] occurs at the top of the rings. The maximal lift off occurring at the axis of symmetry has a value of 1.6 [mm]. The *rp*-method of the FEM is used in this example to eliminate oscillations in the contact stresses at the contact boundary. In Figure 5.38, the deformed ring and the distribution of the von Mises stresses are shown. The inner part of the composite ring is carrying the main load due to its higher material stiffness[5]. To get an idea about the accuracy of the shown discretization we consider the reaction force which is computed by integrating the traction vector over the contact interface. The reaction force amounts to 2200 [N]. Comparing this value with the

---

[4] The Arclength Method used in this simulation is only implemented for load controlled problems. Therefore the boundary conditions had to be changed from Dirichlet, to Neumann boundary conditions.

[5] The occurring stresses in the inner ring due to bending are large compared to the contact stresses in the contact interface. Convergence problems were experienced during the computation of this example presumably due to the large element deformations. As a result of these problems it was not possible to obtain results for two different FEM versions having the same load factor. Therefore no comparison of different versions of the FEM is presented for this example.

applied load of 2070 [N], we find that the relative error of the reaction force becomes 6.3%. More accurate results can be obtained by further increasing the polynomial degree. However, from this example it is evident, that a rather coarse discretization provides already a quite accurate approximation when applying the rp-version of the FEM.

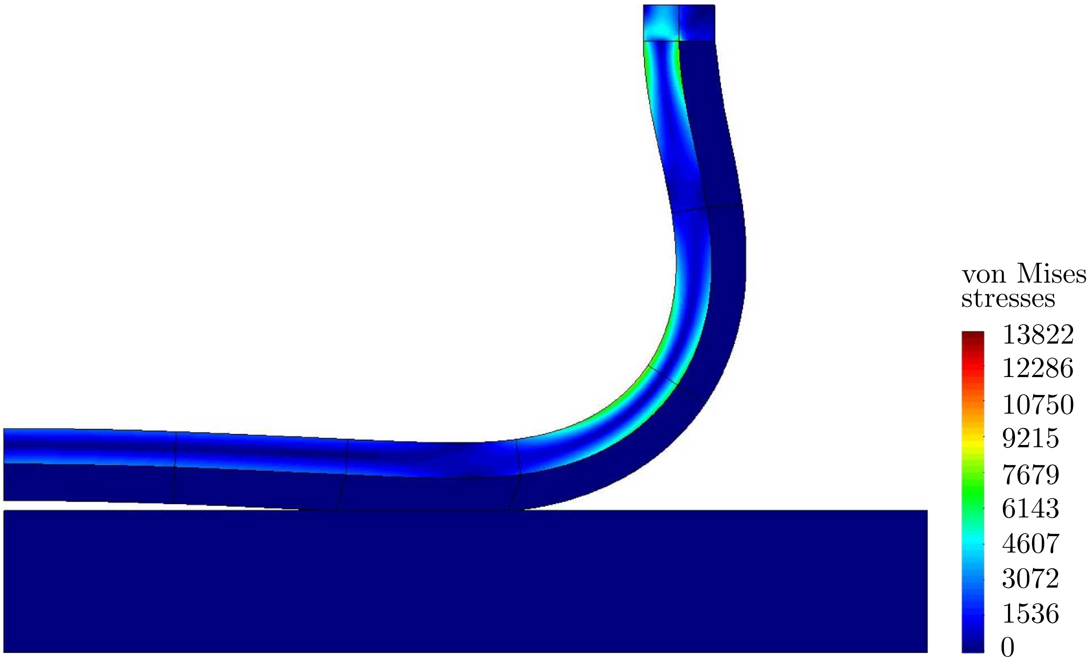

Figure 5.38: Von Mises stresses and deformation for the composite ring in contact with a rigid foundation.

5.4 Stiff Axle in Elastic Ring

Another example studied for the unilateral case is the setup of a rigid axle located in an elastic ring. The geometric parameters of the plane strain problem are shown in Figure 5.39. The radii are $r_1 = 2.0$, $r_2 = 0.7$, and $r_3 = 0.6$. Only one half of the symmetric system is modeled in the numerical setup. The Young's modulus of the ring is set to $E = 1000$ with a Poisson ratio of $\nu = 0.0$. The computations are performed geometrically nonlinear, allowing for large displacements. Only normal contact is considered using a penalty parameter of $\epsilon_N = 10^6$. The displacement based load $v_0 = 0.45$ acts on the rigid axle in vertical direction. Three different meshes are used for the computation. For each mesh the principal stress σ_1 is plotted in the following Figures. Its distribution is indicated in Figure 5.40(a) by the blue color. The contact stress acts in normal direction on the contact boundary. As it (the contact stress) defines the main stresses in the given setup, it is equivalent to the principal stress on the boundary. Figure 5.40(b) shows the result where the ring is computed with two elements only having a polynomial degree of $p = 4$. The results for a uniformly refined mesh with 12 elements is shown in Figure 5.41(a), computed also with a polynomial degree of $p = 4$. A locally h-refined mesh is used for the computations with the 16 element mesh (for the ring) and the polynomial degree is set to $p = 5$. The corresponding strain energy is: $\|\mathbf{u}\|_{E(\Omega)} = 77.01673366$ for the two element mesh, $\|\mathbf{u}\|_{E(\Omega)} = 76.52192848$ for the 12 element mesh, and $\|\mathbf{u}\|_{E(\Omega)} = 76.51554562$ for the 16 element mesh.

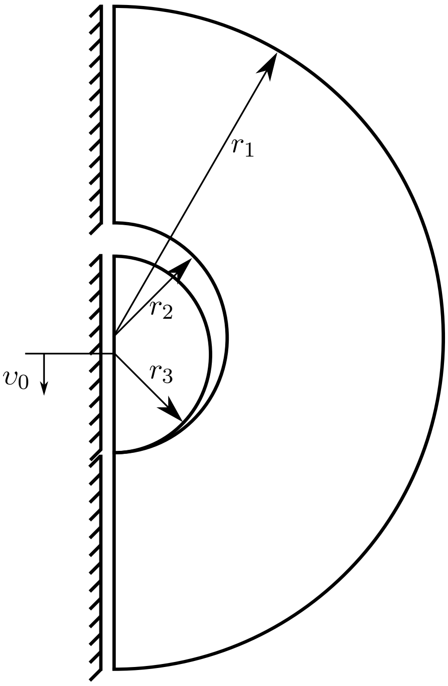

Figure 5.39: Geometric Setup of elastic ring with rigid axle.

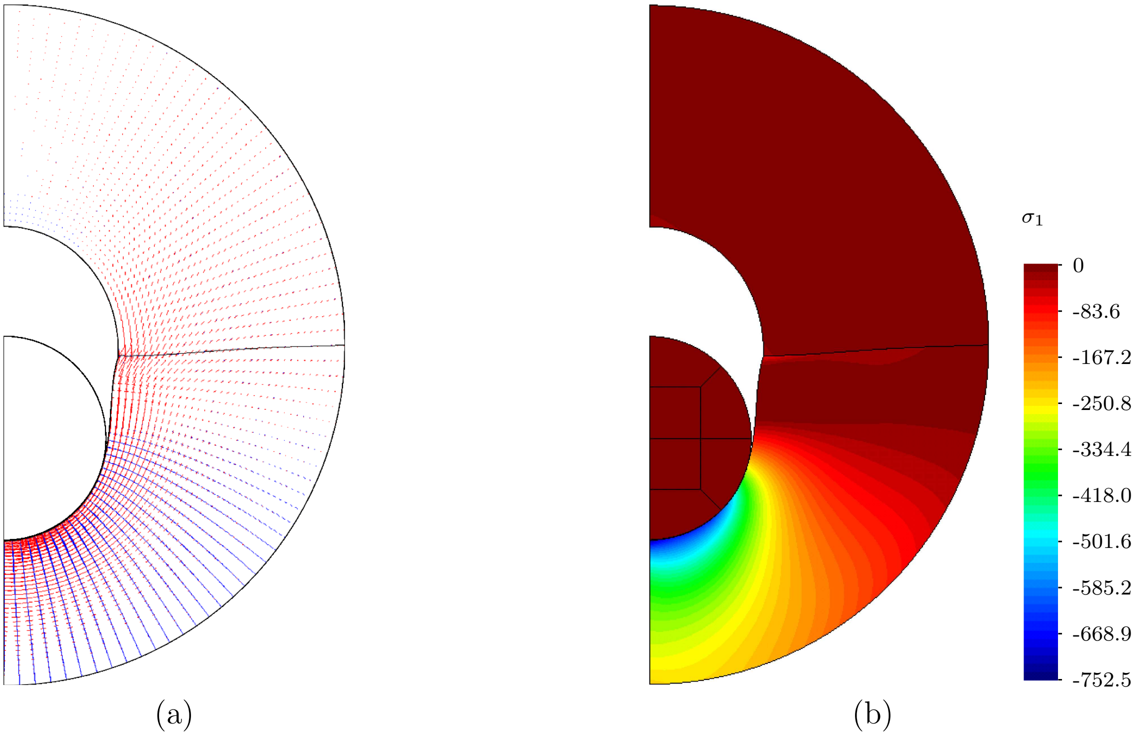

(a) (b)

Figure 5.40: (a) shows the principal stress trajectories for the contact between an elastic ring and a rigid axle computed with two elements and p=4. The principal stresses σ_1 are displayed in blue and stresses σ_2 are displayed in red. (b) shows the principal stresses in σ_1-direction for a mesh where the ring is modeled with two elements and p=4.

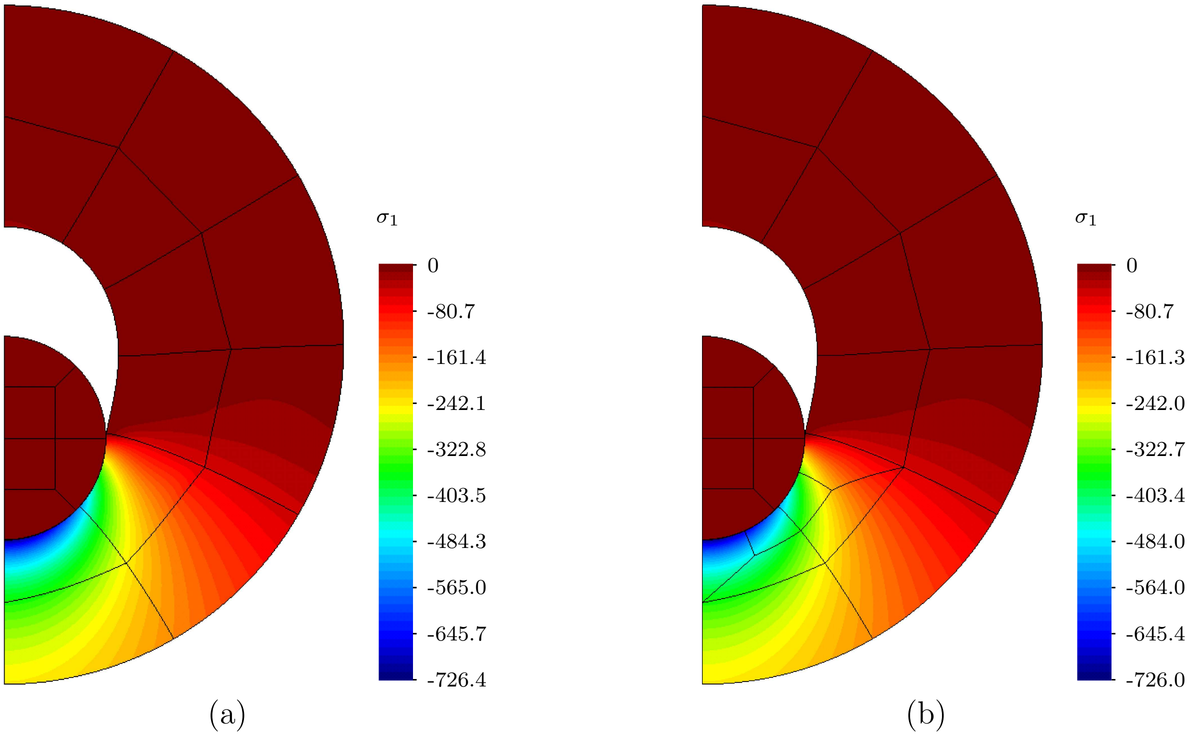

Figure 5.41: (a) shows the principal stres of the normal contact component σ_1 for a mesh where the ring is modeled with 12 elements and p=4. (b) shows the equivalent results for a h-refined mesh with 16 elements and p=5.

5.5 Frictional Two Bar System

Contact including friction is studied for the unilateral and bilateral case. The corresponding theory is given in Section 3.3. At the end of the contact interface, a point with reduced regularity exists, as described for the normal contact in the previous section. When sliding contact with the Coulomb friction model is to be considered as well, a second point with reduced regularity occurs. This point is located at the interface between the zone in stick and slip. A kink in the stress distribution occurs there. As for the reduced regularity at Γ_*, the hp- or rp-method can be used to resolve this singularity. Applying the rp-method, a Finite Element node has to coincide with this point. When the hp-method is used, the area around this second point with reduced regularity has to be refined adaptively.

5.5.1 Numerical Model and Reference Solution

The example studied for the case of frictional contact is a system that consists of two beams which are placed on top of each other as shown in Figure 5.42. The bottom beam is relatively stiff with a Poisson ratio of zero. The top beam is pressed onto the bottom beam by a Dirichlet boundary condition of $v_0 = 0.03$ to establish contact and then loaded horizontally by a uniformly distributed load of 300. The penalty parameter is chosen to be $\epsilon_n = 10^8$. The polynomial degree is set to $p = 15$ in x-direction and to $p = 5$ in y-direction (vertical direction). For the case of pure stick, this geometric setup corresponds to the system of a monolithic plate with inclined edge (also referred to as the L-shaped domain), studied extensively by [81] and

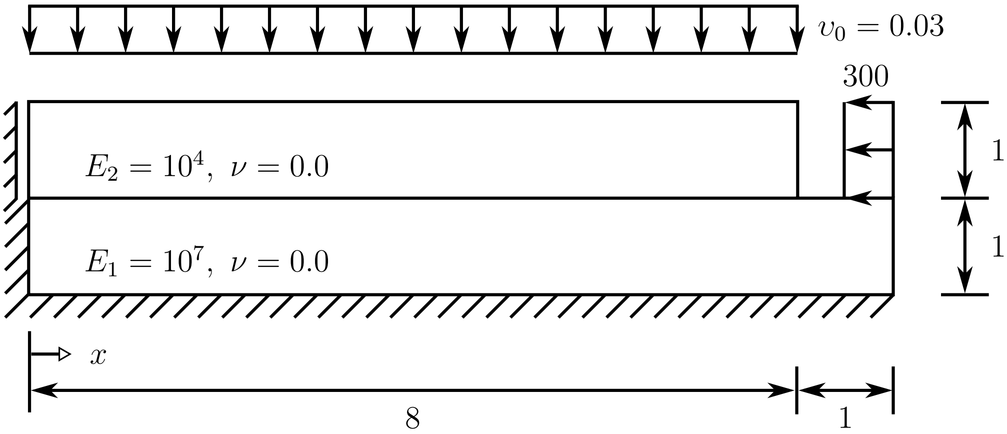

Figure 5.42: Geometric setup and loads for the two bar example with frictional stick.

[59]. It is well known that for this problem type a singularity is present in the solution at the inclined corner of the plate.

In order to prove the accuracy of the contact algorithm for bilateral problems, the results of the contact simulation have to be compared to a reference solution. The reference solution for the case of pure stick is computed in a setup where both beams are connected monolithically. As the penalty method is used to incorporate the contact constraints, the non-penetration condition is violated by allowing for some small penetration of the two beams in the contact interface. This reduces the effective displacement, acting on the two bars, as the displacement of 0.03 applied on the top of the upper beam is partly dissipated by the penetration of the two beams. A model without a penalty parameter (spring) in the contact interface (monolithic model) therefore needs a smaller displacement at the top in order to exhibit the same strains inside the domain and serve as a reference solution. The reduced value for the displacement boundary condition applied at the top can be derived by taking a system of coupled springs, once with and once without the penalty spring stiffness. Figure 5.43 shows the difference between the spring models of the contact model (Figure 5.43(a)) and monolithic model (Figure 5.43(b)). In the contact model, the Young's modulus of each bar forms the stiffness of the top and bottom springs. In between, the spring stiffness is equivalent to the penalty parameter. The residual spring stiffness K^a_{res} for the monolithic system (a) is:

$$\frac{1}{K^a_{res}} = \frac{1}{E_1} + \frac{1}{E_2} \ . \tag{5.12}$$

The residual spring stiffness K^b_{res} for system (b) is derived by:

$$\frac{1}{K^b_{res}} = \frac{1}{E_1} + \frac{1}{\epsilon_n} + \frac{1}{E_2} \ . \tag{5.13}$$

As the forces $F_i = K_i \cdot \upsilon^i_0$ should be equal for both models the equality $K^a_{res} \cdot \upsilon^a_0 = K^b_{res} \cdot \upsilon^b_0$ can be formulated. The new value of υ^b_0 for the monolithic system is then derived by

$$\upsilon^b_0 = \frac{K^b_{res}}{K^a_{res}} \cdot \upsilon^a_0 = 0.029997003 \ . \tag{5.14}$$

Both models, the reference solution and the frictional contact solution have to deal with the singularity at the inclined edge, as explained before. In order to be able to compare the results

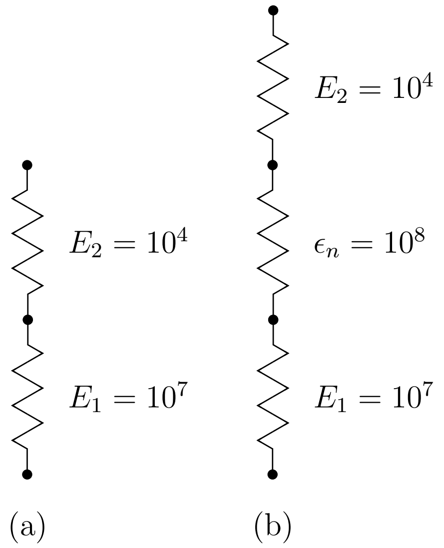

Figure 5.43: Substituted mechanical system to derive the reduced value for the Dirichlet boundary condition on the monolithic two bar example with frictional stick.

derived from the contact simulation with the reference simulation, the discretization of both problems (contact and monolithic) has to be exactly identical. Therefore the mesh for the reference solution, its material parameters, and its ansatz space are the same for both models. The effect of the tangential penalty parameter, accounting for the stick part of the friction model is more complex. The tangential penalty parameter allows for some artificial micro slip in tangential direction which is not accounted for in the monolithic setup and is therefore mainly introducing an error in the horizontal displacement and its derivative, the strain σ_x.

5.5.2 Numerical Results

Numerical results are shown for the model where the frictional contact is modeled with full stick and for the model where a Coulomb friction model is used for the frictional contact part.

5.5.2.1 Comparison of monolithic solution and contact solution with stick

A comparison of the error in strain energy shows a good correlation of both models (contact and monolithic model). The geometry is discretized using three elements only. The mesh can for example be seen in the displacement pot in Figure 5.47. For an ansatz space of fifteen in x-direction and five in y-direction, the monolithic model has a strain energy of 39.71208524 whereas the model including contact results in a strain energy of 39.71209717. Scaling it to the strain energy of the monolithic model it turns out to be an error of $3 \cdot 10^{-5}\%$. The error of the strains in L^2-norm, given in Equation 5.15, is computed in the contact domain for the monolithic model compared with the contact model.

$$\|e_\varepsilon\|_{L^2} = \frac{\sqrt{\int_0^8 \left(\varepsilon_{monolytic} - \varepsilon_{contact}\right)^2 dx}}{\int_0^8 \varepsilon_{monolytic}\, dx} \tag{5.15}$$

The error in L^2-norm for the strains in y-direction is $\left\|e_{\varepsilon_y}\right\|_{L^2} = 0.002\%$. The error for the strains in x-direction is much larger due to the aforementioned difference between the two models, therefore the error turns out to be $\|e_{\varepsilon_x}\|_{L^2} = 30.696\%$ when the full contact interface is considered. From these 30.696%, the largest part is observed in the vicinity of the inclined edge. Dividing the domain, we get an error in L^2-norm of $\|e_{\varepsilon_x}\|_{L^2} = 2.501\%$ for the interval $x = (0, 7.5)$ and an error $\|e_{\varepsilon_x}\|_{L^2} = 45.633\%$ in the interval $x = 7.5, 8.0)$. This becomes evident when looking at the corresponding ε_x-strains, plotted in Figure 5.44. In the monolithic solution, tensile strains are occurring in the vicinity of the singularity, turning into compressive strains further away from the singular point. The contact solution is allowing for some displacement in tangential direction by definition. Therefore, deflection and compressive strains arise already at x=8, explaining the large difference occurring there locally. Even more interesting is a plot of the strains ε_{xy} (see Figure 5.45), which correspond in this setup to the tangential strains in the contact interface and therefore to the contact stresses. Its error in L^2-norm turns out to be $\left\|e_{\varepsilon_{xy}}\right\|_{L^2} = 0.172\%$ which is good concerning the error due to the tangential penalty parameter. The plot shows clearly the singularity at the inclined edge, occurring in the case of stick. The result of both models coincide in Figure 5.45, showing only one line. The plot also clearly shows the pattern of a polynomial of order 15, as minor oscillations can be observed. Figure 5.46 shows the corresponding trend of the shear stresses σ_{xy} for the monolithic model, or tangential contact stresses σ_t. In this case the stresses are connected to the strains by a linear material law. Therefore the trend of the curves given in Figures 5.45 and 5.46 are identical.

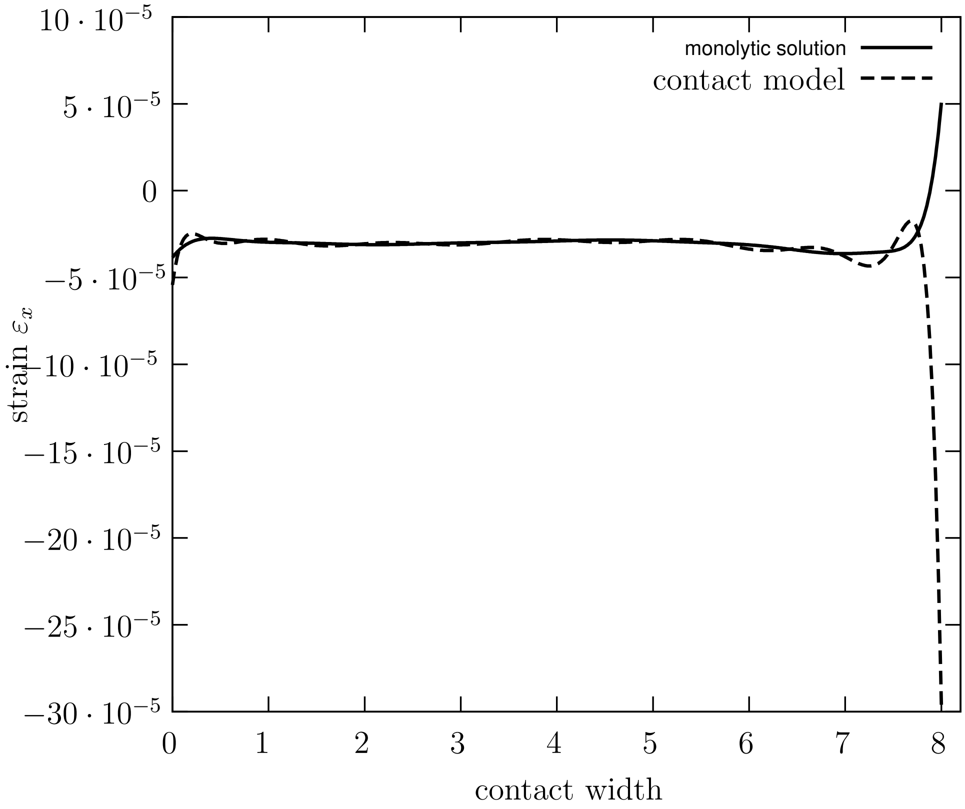

Figure 5.44: Strain ε_x for monolithic model and contact model in the contact interface.

In Figures 5.47, and 5.48, the displacement and stress in x-direction for the contact model of the two bar system with friction in the pure stick case is shown. Figure 5.49 plots the tangential shear stresses σ_{xy} for the model considering contact. The error in the von Mises

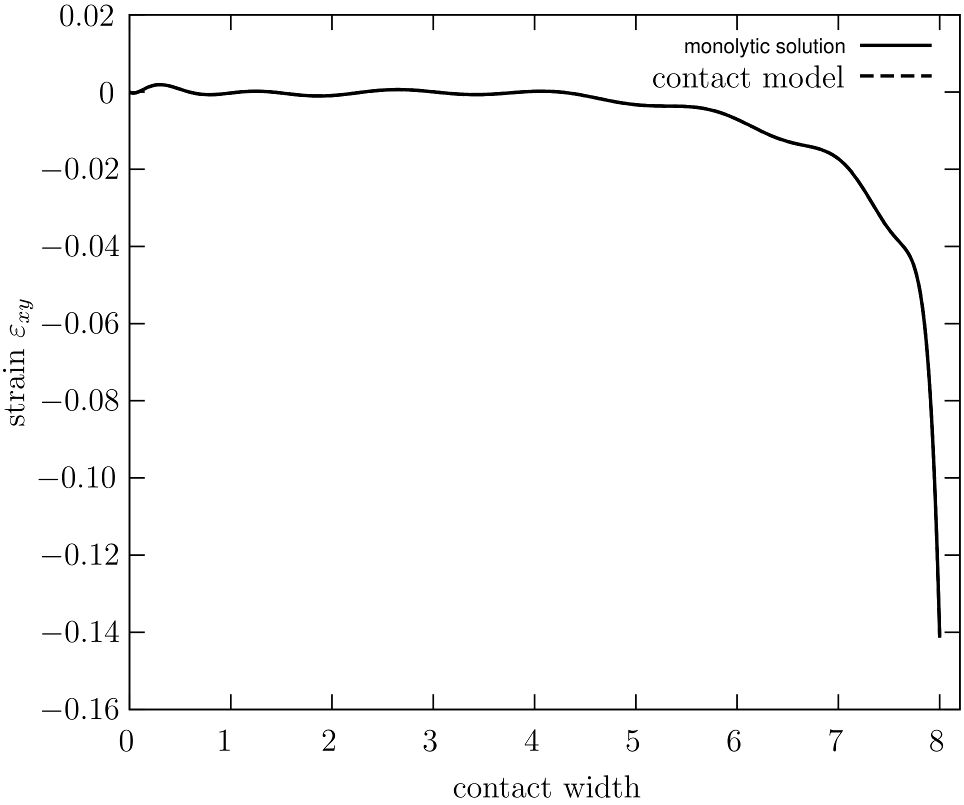

Figure 5.45: Strain ε_{xy} for monolithic model and contact model coincide in the contact interface.

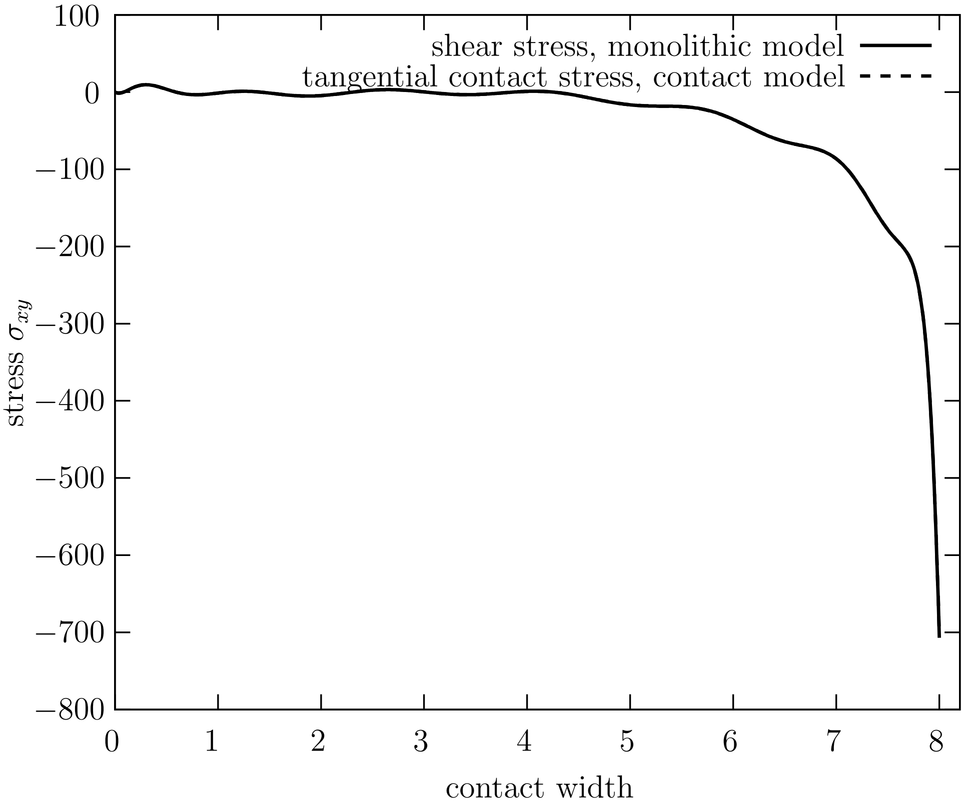

Figure 5.46: Stresses σ_{xy} for monolithic model and contact model coincide in the contact interface.

stresses is shown in Figure 5.50. The maximal value in the legend shows an error of 0.1% of the maximal von Mises stress occurring in the monolithic model. As already seen in the previously plotted line charts, the only position where an error occurrs is around the area of the inclined edge.

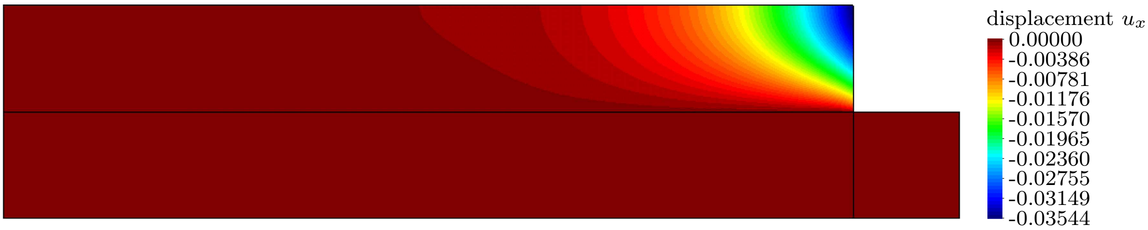

Figure 5.47: Horizontal displacement in x-direction for pure stick case.

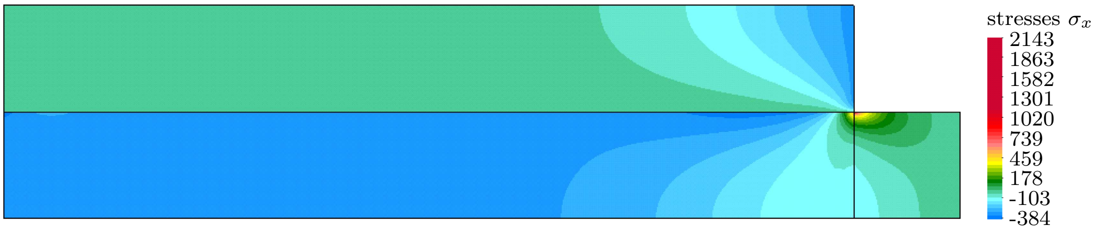

Figure 5.48: Stresses in x-direction for pure stick case.

Figure 5.49: Tangential shear stresses σ_{xy} for pure stick case.

Figure 5.50: Relative error in von Mises stresses for the 3 element mesh of the two bar example. Comparison of monolithic model and frictional contact model in the case of pure stick. The maximal value in the legend shows an error of 0.1% of the maximal von Mises stress occurring in the monolithic model.

5.5.2.2 Results using the Coulomb Friction Model

Computations are also performed for the frictional contact with sliding, using a Coulomb friction model. A friction coefficient of $\mu = 0.3$ is assumed. The geometry, loads, boundary condition, material and polynomial degree is chosen to be the same as in the previous model, $p = 15$ in x-direction and $p = 5$ in y-direction. Figure 5.51 plots the normal and tangential contact stress in the contact interface. Especially when compared to Figure 5.46 it is clearly visible, that the Coulomb friction law limits the maximal tangential friction stress σ_t. The dotted line marks the friction bound of $0.3 \cdot \sigma_n$. The frictional contact stress in slip (solid line) is generally seen to be bounded by this value, even though oscillations in the tangential stresses can be observed. They derive from the fact that a point with reduced regularity is existing in the tangential stress distribution. At the interface from slip to stick, a reduced regularity in the solution is present. The continuous polynomial of order $p = 15$ is not able to resolve this point and therefore starts to oscillate. The oscillatory behavior could be avoided by either have the interface from stick to slip coincide with a Finite Element node (by applying the rp-method), or by framing this singular point with a small element in a hp-manner.

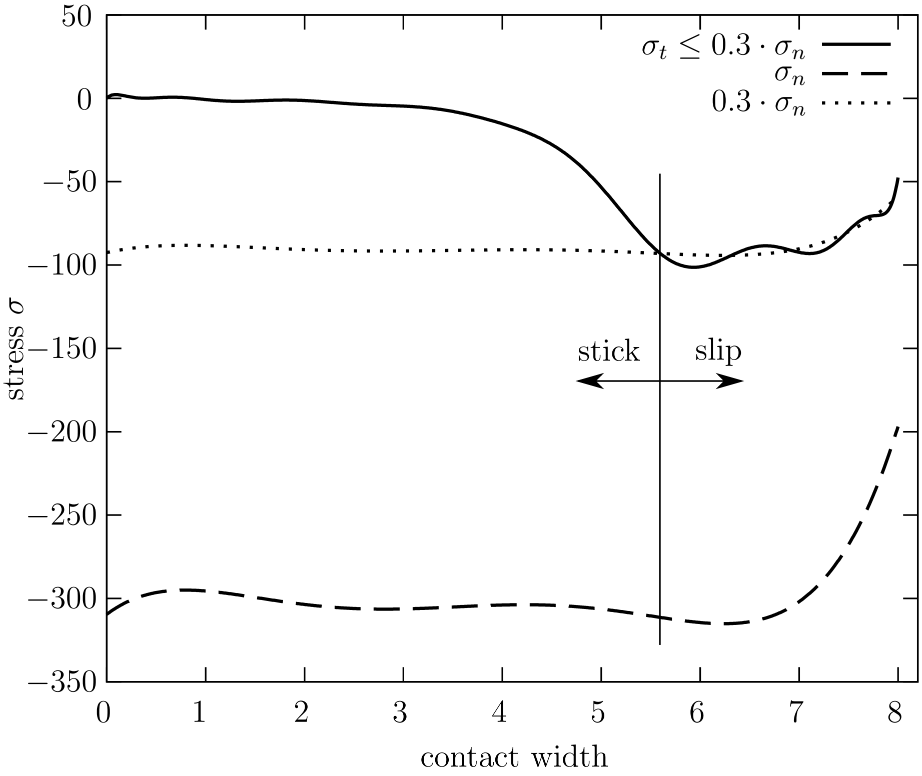

Figure 5.51: Normal and tangential contact stress in the contact interface for Coulomb friction model.

The horizontal deformations u_x the horizontal stresses σ_x and tangential stresses σ_{xy} are plotted in Figures 5.52 - 5.54.

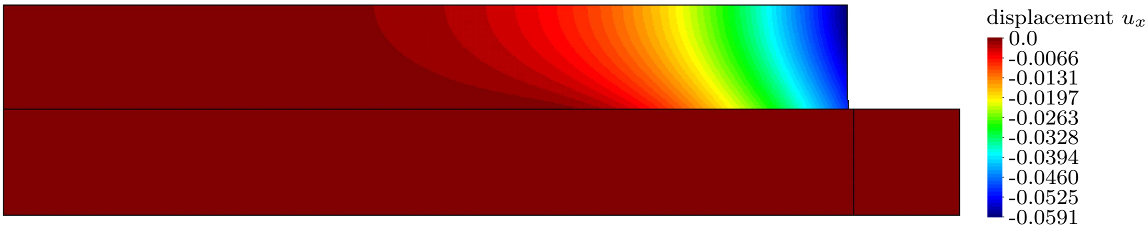

Figure 5.52: Horizontal displacement u_x with Coulomb friction law and frictional contact in stick and slip.

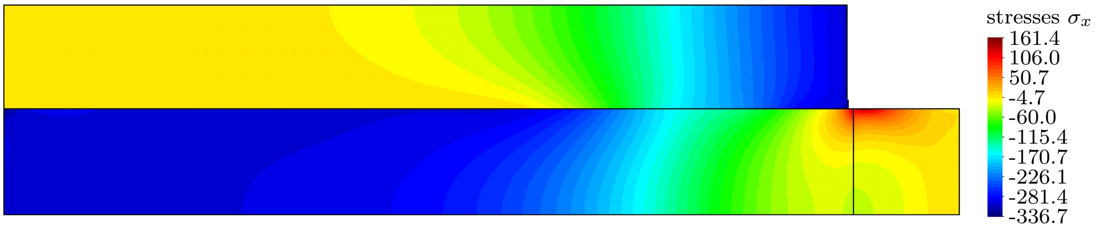

Figure 5.53: Horizontal stresses σ_x with Coulomb friction law and frictional contact in stick and slip.

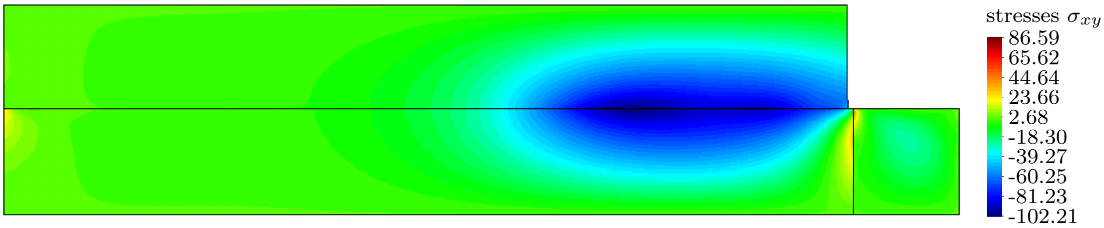

Figure 5.54: Tangential shear stresses σ_{xy} with Coulomb friction law and frictional contact in stick and slip.

Chapter 6

Summary and Outlook

In the present work the applicability and performance of high-order Finite Elements in the field of computational contact mechanics is investigated. Studies are performed for two dimensional unilateral, bilateral, frictionless and frictional contact cases with infinitesimal and finite strains considering non-matching meshes. Various high- and low-order schemes are investigated in terms of accuracy of the contact stresses and in terms of the convergence behavior of the error in strain energy norm. To incorporate the contact constraints into the analysis, the penalty method is implemented, allowing for a small penetration of the contacting objects. The error introduced by this approximative fulfillment of the non penetration condition is small and without a significant influence on the present study. Nevertheless, the applied high- and low-order schemes could also be used with different discretization methods like the Lagrangian or augmented Lagrangian method. The mortar method could as well be applied, but it is assumed that no significant benefit would result from it, as its main advantage lies in the treatment of non matching meshes, which is solved differently in the present study. Furthermore, the border of the contact interface where the boundary condition changes from contact to non-contact, would have to be treated in the same way as presented here to avoid oscillations of the high-order polynomials used as the ansatz space.

This can be seen in the study of the contact stresses. For the test case of the unilateral frictionless Hertzian contact problem, conventional low-order (*h*-version) and high-order (*p*-version) schemes of the Finite Element Method are investigated. Within the *p*-version approach, the *hp*- and the *rp*-version as an adaptive extension of the *p*-version are applied. The *hp*-method increases its accuracy at singular points by a combination of a local mesh refinement and an adaptive method where the shape function's polynomial degree for each element is chosen separately. The *rp*-method resolves the singular point by moving a Finite Element node into the singular point in the solution domain. The evaluation of the results for the contact stresses shows rather that the conventional low order methods with isoparametric element concepts lead to bad results especially for curved geometries. When high-order ansatz functions are used instead, the quality of the result is generally improved. However, the reduced regularity at the end of the contact interface at Γ_* (where a change exists in the boundary conditions) leads to oscillations in the case of the high polynomials. These oscillations can be reduced or avoided when the adaptive *hp*- or *rp*-method is applied. The improved accuracy of both methods is achieved by an adaptive scheme, requiring a precise location of the contact interface for the *rp*-, and a fairly precise location of the contact interface for the *hp*-method. Therefore several iterations have to be performed to obtain the desired accuracy in the contact stresses. The *hp*-method minimizes the influence area of the point Γ_* with reduced regularity at the end of the contact interface, therefore limiting the oscillatory area and its effect as well. Oscillations occur, but only in the innermost element, which contains the change in the boundary condition. When the *rp*-version of the FEM is applied, oscillations in the contact stresses can even be completely avoided, by having a Finite Element node coincide with Γ_* at the end of the contact interface.

Studies performed on the convergence rate of the error in strain energy norm also provide a measure for the quality of the overall solution. These studies are performed for the same *h*-, *p*-, *hp*-, and *rp*-version of the FEM. The results have a similar trend than the one obtained for the survey of the contact stresses. The *h*- and the *p*-version show an algebraic rate of convergence, with a higher gradient β for the pure *p*-FEM approach. The application of the *rp*-FE method shows as well an algebraic rate of convergence, but with a higher gradient than the non-adaptive methods. The convergence is faster because oscillations in the polynomial ansatz functions are avoided by the method. The reason for the algebraic rate of convergence can be explained with the analogy of the contact problem to a Neumann boundary condition. Contact stresses acting on a boundary cause the same kind of reduced regularity at the end of the contact interface at Γ_* as in general a Neumann boundary at its ends of a distributed loading zone. Only under certain geometric and loading conditions, this singularity does not introduce any error to the numerical solution. The reduced regularity therefore limits the convergence rate to be of algebraic type in the asymptotic range. In the pre-asymptotic range exponential rates of convergence can occur for structures having complex solution patterns if the *p*-version and its extensions are used. Even higher rates of convergence can be observed for the *hp*-version. The rate of convergence is of exponential nature if the full adaptive *hp*-scheme is applied. The combinations of high polynomial degrees in the solution domain and a low polynomial order in the small area where the singularity at the end of the contact interface occurs further limits the influence area in each refinement step and therefore results in an exponential rate of convergence. Furthermore the number of iteration steps needed for a certain level of accuracy in the *hp*-scheme, is less than the one needed in the *rp*-scheme. This counterbalances the additional introduced degrees of freedom due to the additional elements and the increased computation time for each single iteration step.

Bilateral frictional contact is studied for the case of stick and slip for the example of two contacting bars. For both cases, a good correlation of the model with contact and the reference solution without contact can be observed. The error in tangential direction occurring in the case of stick is solely due to the tangential penalty factor. In the case of frictional contact with slip, a Coulomb friction model with elastic stick is applied. It generally shows reasonably good results, but demonstrates the need to resolve the location between the stick and the slip zone. This could either be done by the *rp*- or the *hp*-method as described for the normal contact. This example also shows the performance of the implemented bilateral contact description.

The application of high-order Finite Element Methods is therefore well suited for mechanical contact problems. The discretization of the domain should contain rather large elements and the contact boundaries should have a rather smooth geometric setup with considerably large contact interfaces. The *hp*-version of the FEM shows the overall best solution regarding the contact stresses and the convergence of the error in strain energy norm.

A topic that should be addressed by future research is the extension of the proposed *hp*-version to three-dimensional problems, especially to thin solids. The success of such a research significantly depends on the mesh generation and adaptive refinement in the 3D contact zone. This is especially true if curved geometries are considered. Studies on hexahedral mesh generation for these curved geometries have lately been performed by Sorger et al. [76, 77]. Especially for the simulation of deep drawing processes of thin sheet metal with the p-version of the Finite Element Method the described method creates meshes of high quality and great geometric accuracy, which are therefore well suited for the computation. Furthermore the linearization of the contact problem needs to be changed from the numerical discrete Newton method to an analytical method suited for the high-order approach. A promising linearization technique was introduced by Konyukhov [52] which is based on a covariant description of the contact problem.

As the Isogeometric Element concept introduced by Hughes [46] and Cottrell [12] is closely related to the p-version of the Finite Element Method, it is believed that many of the results obtained for the p-version of the FEM in the present study do also apply for the Isogeometric concept. Nevertheless, a detailed study should be performed to prove this assumption.

The Neumann boundary condition and its reduced regularity at the end of the load distribution zone should also be studied in more detail. This is, independent from the contact formulation, a field of research which is of great interest due to its frequent appearance. It is assumed, that having the Finite Element node coincide with the end of the distributed load is generally sufficient for the discretization of the edge, but the reduced regularity due to the load must travel into the domain as well, causing the error there. If the path of the 'fault line' could be located, the reduced regularity might be resolved by having it coincide with a Finite Element edge. Possibly a detailed study of the stress intensity factor at this point could help in classifying and localizing the direction of the error in the domain.

Bibliography

[1] M. Ainsworth and J.T. Oden. *A posteriori error estimation in finite element analysis.* John Wiley & Sons, 2000.

[2] M. Ainsworth and B. Senior. Aspects of an adaptive *hp*-finite element method: Adaptive strategy, conforming approximation and efficient solvers. *Computer Methods in Applied Mechanics and Engineering*, 150:65–87, 1997.

[3] I. Babuška and B.Q. Guo. Approximation properties of the hp-version of the finite element method. *Computer Methods in Applied Mechanics and Engineering*, 133:319–346, 1996.

[4] I. Babuška and T. Strouboulis. *The finite element method and its reliability.* Oxford University Press, 2001.

[5] A. Baksa. *Érintkezési feladatok numerikus vizsgálata.* Dissertation, Miskolc, 2005.

[6] K.J. Bathe. *Finite element procedures.* Prentice Hall, 1996.

[7] C. Bernardi, N. Debit and Y. Maday. Coupling finite elements and spectral methods: First results. *Mathematics of Computation*, 54:21–39, 1990.

[8] C. Bernardi, Y. Maday and A.T. Patera. Domain decomposition by the mortar element method. In *Asymptotic and numerical methods for partial differential equations with critical parameters (Beaune, 1992)*, volume 384 of *NATO Adv. Sci. Inst. Ser. C Math. Phys. Sci.*, pages 269–286. Kluwer Acad. Publ., Dordrecht, 1993.

[9] C. Bernardi, Y. Maday and A.T. Patera. A new nonconforming approach to domain decomposition: the mortar element method. In *Nonlinear partial differential equations and their applications. Collège de France Seminar, Vol. XI (Paris, 1989–1991)*, volume 299 of *Pitman Res. Notes Math. Ser.*, pages 13–51. Longman Sci. Tech., Harlow, 1994.

[10] J. Bonet and R.D. Wood. *Nonlinear continuum mechanics for finite element analysis.* Cambridge University Press, New York, 1997.

[11] R. W. Clough. Early history of the finite element method from the view point of a pioneer. *International Journal for Numerical Methods in Engineering*, 60:283–287, 2004.

[12] J.A. Cottrell, T.J.R. Hughes and Y. Bazilevs. *Isogeometric Analysis: Toward Integration of CAD and FEA.* Wiley Publishing, 2009.

[13] M.A. Crisfield. *Non-linear finite element analysis of solids and structures, Volume 1.* John Wiley & Sons, 1991.

[14] L. De Lorenzis, I. Temizer, P. Wriggers and G. Zavarise. A large deformation frictional contact formulation using nurbs-based isogeometric analysis. *International Journal for Numerical Methods in Engineering*, Available online 2011.

[15] L. Demkowicz. *Computing with hp-adaptive finite elements: one and two dimensional elliptic and Maxwell problems*, volume 1. Chapman & Hall / CRC Applied Mathematics & Nonlinear Science, 2006.

[16] L. Demkowicz, J. Kurtz, D. Pardo, M. Paszyński, W. Rachowicz and A. Zdunek. *Computing with hp-adaptive finite elements: three dimensional elliptic and Maxwell problems with applications*, volume 2. Chapman & Hall / CRC Applied Mathematics & Nonlinear Science, 2007.

[17] S. Dey. *Geometry based three-dimensional hp-finite element modelling and computation.* Dissertation, Faculty of Rensselaer Polytechnic Institute, 1997.

[18] A. Düster. Die hp-d Methode für Reissner-Mindlin Plattenprobleme. In M. Hauser and P. Katrunoschkov, editors, *9. Forum Bauinformatik*, Fortschrittberichte VDI, Reihe 4: Bauingenieurwesen, pages 211–218. VDI-Verlag, 1997.

[19] A. Düster. *High order finite elements for three-dimensional, thin-walled nonlinear continua.* Dissertation, Lehrstuhl für Bauinformatik, Fakultät für Bauingenieur- und Vermessungswesen, Technische Universität München, 2001.

[20] A. Düster, S. Hartmann and E. Rank. p-fem applied to finite isotropic hyperelastic bodies. *Computer Methods in Applied Mechanics and Engineering*, 192:5147–5166, 2003.

[21] C. Eck, S.A. Nazarov and W.L. Wendland. Asymptotic analysis for a mixed boundary-value contact problem. *Archive for Rational Mechanics and Analysis*, 156:275–316, 2001.

[22] G. Engeln-Müllges and F. Reutter. *Numerik-Algorithmen.* VDI-Verlag, Düsseldorf, 1996.

[23] K.A. Fischer. *Mortar Type Method Applied to Nonlinear Contact Mechanics.* Dissertation, Institut für Baumechanik und Numerische Mechanik, Universität Hannover, 2005.

[24] K.A. Fischer and P. Wriggers. Frictionless 2d contact formulations for finite deformations based on the mortar method. *Computational Mechanics*, 36:226–244, 2005.

[25] D. Franke, A. Düster, V. Nübel and E. Rank. A comparison of the *h*-, *p*-, *hp*-, and *rp*-version of the FEM for the solution of the 2d Hertzian contact problem. *Computational Mechanics*, 45:513–522, 2010.

[26] D. Franke, A. Düster and E. Rank. The p-version of the FEM for computational contact mechanics. *Proceedings in Applied Mathematics and Mechanics*, 8(1):10271– 10272, 2008.

[27] D. Franke, A. Düster and E. Rank. Computational contact mechanics based on the *rp*-version of the Finite Element Method. *International Journal of Computational Methods*, 8:493–512, 2011.

[28] D. Gabriel. *Numerical Solution of Large Displacement Contact Problems by the Finite Element Method.* Dissertation, Faculty of Mechanical Engineering, Czech Technical University of Prague, 2003.

[29] V. Galishnikova, P.E. Dunaiski and J.P. Pahl. *Geometrically nonlinear analysis of plane trusses and frames.* Sun Press, Stellenbosch, South Africa, 2009.

[30] http://gid.cimne.upc.es.

[31] M. Gitterle, A. Popp, M.W. Gee and W.A. Wall. Finite deformation frictional mortar contact using a semi-smooth Newton method with consistent linearization. *International Journal for Numerical Methods in Engineering*, 84:543–571, 2010.

[32] http://www.gnuplot.info.

[33] W. Goldsmith. *Impact.* Dover Publications, New York, 1. Auflage, 2002.

[34] W.J. Gordon and Ch.A. Hall. Construction of curvilinear co-ordinate systems and applications to mesh generation. *International Journal for Numerical Methods in Engineering*, 7:461–477, 1973.

[35] W.J. Gordon and Ch.A. Hall. Transfinite element methods: Blending function interpolation over arbitrary curved element domains. *Numerische Mathematik*, 21:109–129, 1973.

[36] C. Grossmann and H.-G. Roos. *Numerical Treatment of Partial Differential Equations.* Springer, 2007.

[37] S. Hartmann. *Kontaktanalyse dünnwandiger Strukturen bei großen Deformationen.* Dissertation, Institut für Baustatik und Baudynamik, Universität Stuttgart, 2007.

[38] M. Hazewinkel. *Encyclopaedia of Mathematics.* Springer-Verlag, Berlin, Heidelberg, New York, 2002.

[39] V. Hegadekatte, N. Huber and O. Kraft. Development of a simulation tool for wear in microsystems. In D. Löhe and J. Haußelt, editors, *Advanced Micro and Nanosystems*, volume 4 of *Microengineering of Metals and Ceramics Part II*, pages 605–623. WILEY-VCH GmbH & Co. KGaA, Weinheim, 2008.

[40] U. Heißerer. *High-order finite elements for material and geometric nonlinear finite strain problems.* Dissertation, Lehrstuhl für Computation in Engineering, Fakultät für Bauingenieur- und Vermessungswesen, Technische Universität München, 2008.

[41] U. Heißerer, S. Hartmann, A. Düster and Z. Yosibash. On volumetric locking-free behavior of p-version finite elements under finite deformations. *Communications in Numerical Methods in Engineering (in press) DOI: 10.1002/cnm.1008*, 2007.

[42] H. Hertz. Über die Berührung fester elastischer Körper. *Journal für die reine und angewandte Mathematik*, 92:156–171, 1881.

[43] C. Hirsch. *Numerical Computation of Internal & External Flows.* Butterworth-Heinemann, Great Britan, 2007.

[44] S.M. Holzer and C. Haußer. Ergebnisverbesserung von Finite-Element-Berechnungen durch exakte Geometriemodellierung. *Forschung im Ingenieurwesen*, 56(3):65–70, 1990.

[45] T. J. R. Hughes. *The Finite Element Method: Linear Static and Dynamic Finite Element Analysis.* Dover Publications, 2000.

[46] T. J. R. Hughes, J. A. Cottrell and Y. Bazilevs. Isogeometric analysis: CAD, finite elements, NURBS, exact geometry and mesh refinement. *Computer Methods in Applied Mechanics and Engineering*, 194:4135–4195, 2005.

[47] http://inkscape.org.

[48] K.L. Johnson. *Contact mechanics.* Cambridge University Press, 1. Auflage, 1985.

[49] M.L. Kachanov, B. Shafiro and I. Trukrov. *Handbook of Elasticity Solutions.* Kluwer Academic Publishers, Dordrecht, 1. Auflage, 2003.

[50] N. Kikuchi and J.T. Oden. *Contact problems in elasticity: A study of variational inequalities and finite element methods.* SIAM Studies in Applied Mathematics, 1988.

[51] D. Kinderlehrer. Remarks about signorini's problem in linear elasticity. *Annali della Scuola Normale Superiore di Pisa - Classe di Scienze*, 8:605–645, 1981.

[52] A. Konyukhov and K. Schweizerhof. Incorporation of contact for high-order finite elements in covariant form. *Computer Methods in Applied Mechanics and Engineering*, 198(13-14):1213 – 1223, 2009.

[53] R. Krause, R. Mücke and E. Rank. hp-version finite elements for geometrically nonlinear problems. *Communications in Numerical Methods in Engineering*, 11:887–897, 1995.

[54] T.A. Laursen. *Computational contact and impact mechanics.* Springer, Berlin, 2003.

[55] J. Lu. Isogeometric contact analysis: Geometric basis and formulation for frictionless contact. *Computer Methods in Applied Mechanics and Engineering*, 200(5-8):726 – 741, 2011.

[56] D.G. Luenberger. *Lineare and Nonlinear Programming.* Addison-Wesley, Reading, 1984.

[57] A. Muthler. *Berechnung der elastischen Rückfederung von Tiefziehbauteilen mit der p-Version der Finiten-Elemente-Methode.* Dissertation, Lehrstuhl für Bauinformatik, Fakultät für Bauingenieur- und Vermessungswesen, Technische Universität München, 2005.

[58] A. Niggl, A. Düster and E. Rank. Coupling 1d and 2d elasticity problems by using the *hp-d*-version of the finite element method. In *Proceedings of the Second M.I.T Conference on Computational Fluid and Solid Mechanics*, Cambridge, USA, 2003.

[59] V. Nübel. *Die adaptive rp-Methode für elastoplastische Probleme.* Dissertation, Lehrstuhl für Bauinformatik, Technische Universität München, 2005.

[60] V. Nübel, A. Düster and E. Rank. An *rp*-adaptive finite element method for elastoplastic problems. *Computational Mechanics*, 39:557–574, 2007.

[61] I. Páczelt, B. Szabó and T. Szabó. Solution of contact problem using the hp-version of the finite element method. *Computers & Mathematics with Applications*, 38:49–69, 2000.

[62] I. Páczelt and T. Szabó. Solution of contact optimization problems of cylindrical bodies using hp-fem. *International Journal for Numerical Methods in Engineering*, 53:123–146, 2002.

[63] V. Padmanabhan and T. A. Laursen. A framework for development of surface smoothing procedures in large deformation frictional contact analysis. *Finite Elements in Analysis and Design*, 37(3):173–198, 2001.

[64] P. Papadopoulos and R.L. Taylor. A mixed formulation for the finite element solution of contact poblems. *Computer Methods in Applied Mechanics and Engineering*, 94:373–389, 1992.

[65] M. Puso and T. Laursen. A 3d contact smoothing method using Gregory patches. *International Journal for Numerical Methods in Engineering*, 54:1161–1194, 2002.

[66] E. Rank. *A-posteriori-Fehlerabschätzungen und adaptive Netzverfeinerung für Finite-Element- und Randintegralelement-Methoden.* Dissertation, Elektronisches Rechnen im Konstruktiven Ingenieurbau, Bauingenieur- und Vermessungswesen, Technische Universität München, 1985.

[67] R. A. Sauer and P. Wriggers. Formulation and analysis of a three-dimensional finite element implementation for adhesive contact at the nanoscale. *Computer Methods in Applied Mechanics and Engineering*, 198(49-52):3871 – 3883, 2009.

[68] P.J. Schneider and D. Eberly. *Geometric Tools for Computer Graphics.* Elsevier Science Inc., New York, NY, USA, 2002.

[69] A. Schröder. *Fehlerkontrollierte adaptive h- und hp-Finite-Element-Methoden für Kontaktprobleme.* Dissertation, Mathematisches Institut, Universität Bayreuth, 2006.

[70] R. Schumann. Regularity for Signorini's problem in linear elasticity. *manuscripta mathematica*, 63:255–291, 1989. 10.1007/BF01168371.

[71] Ch. Schwab. *p- and hp-finite element methods, theory and applications in solid and fluid mechanics.* Oxford University Press, 1998.

[72] J.E. Shigley, C.R. Mischke and R.G Budynas. *Mechanical engineering design.* McGraw-Hill, 7. Auflage, 2004.

[73] I.Ya. Shtayerman. *Contact Problem of the Theory of Elasticity.* Gostekhizdat, Moscow, 1949. Available from the British Library in an English translation by Foreign Technology Div., FTD-MT-24-61-70, 1970.

[74] J.C. Simo, P. Wriggers and R.L Taylor. A perturbed Lagrangian formulation for the finite element solution of contact problems. *Computer Methods in Applied Mechanics and Engineering*, 50:163–180, 1985.

[75] G.B. Sinclair. Stress singularities in classical elasticity—ii: Asymptotic identification. *Applied Mechanics Reviews*, 57(5):385–439, 2004.

[76] C. Sorger, A. Düster and E. Rank. Generation of curved high-order hexahedral finite element meshes for thin-walled structures. In *11th ISGG Conference on Grid Generation*, Montreal, Canada, 2009.

[77] C. Sorger, S. Kollmannsberger and E. Rank. Visual domesh: Hexahedral meshing for thin curved solid structures. In *Proc. of the 11th International Congress of Computational Mechanics*, Minnesota, USA, 2011.

[78] M. Stadler and G.A. Holzapfel. Subdivision schemes for smooth contact surfaces of arbitrary mesh topology in 3D. *International Journal for Numerical Methods in Engineering*, 60:1161–1195, 2004.

[79] B.A. Szabó. Estimation and control of error based on p convergence. In I. Babuška, O.C. Zienkiewicz, J. Gago and E.R. de A. Olivera, editors, *Accuracy estimates and adaptive refinements in finite element computations*, pages 61–70. John Wiley & Sons, 1986.

[80] B.A. Szabó. The use of a priori estimates in engineering computations. *Computer Methods in Applied Mechanics and Engineering*, 82:139–154, 1990.

[81] B.A. Szabó and I. Babuška. *Finite element analysis.* John Wiley & Sons, 1991.

[82] B.A. Szabó and I. Babuška. *Introduction to Finite Element Analysis – Formulation, Verification and Validation.* John Wiley & Sons, 2011.

[83] B.A. Szabó, A. Düster and E. Rank. The p-version of the Finite Element Method. In E. Stein, R. de Borst and T. J. R. Hughes, editors, *Encyclopedia of Computational Mechanics*, volume 1, chapter 5, pages 119–139. John Wiley & Sons, 2004.

[84] I. Temizer, P. Wriggers and T.J.R. Hughes. Contact treatment in isogeometric analysis with NURBS. *Computer Methods in Applied Mechanics and Engineering*, 200(9-12):1100 – 1112, 2011.

[85] R. Verfürth. *A review of a posteriori error estimation and adaptive mesh-refinement techniques.* John Wiley & Sons and B.G. Teubner, 1996.

[86] B.I. Wohlmuth. *Discretization methods and iterative solvers based on domain decomposition*, volume 17 of *Lecture Notes in Computational Science and Engineering.* Springer-Verlag, Berlin, 2001.

[87] P. Wriggers. *Nichtlineare Finite-Element-Methoden.* Springer-Verlag, 2001.

[88] P. Wriggers. *Computational Contact Mechanics.* Springer, 2nd Auflage, 2006.

[89] P. Wriggers and G. Zavarise. Computational Contact Mechanics. In E. Stein, R. de Borst and T. J. R. Hughes, editors, *Encyclopedia of Computational Mechanics*, volume 2, chapter 6, pages 195–226. John Wiley & Sons, 2004.

[90] B. Yang, T.A. Laursen and X. Meng. Two dimensional mortar contact methods for large deformation frictional sliding. *International Journal for Numerical Methods in Engineering*, 62:1183–1225, 2005.

[91] Z. Yosibash, S. Hartmann, U. Heisserer, A. Düster, E. Rank and M. Szanto. Axisymmetric pressure boundary loading for finite deformation analysis using p-FEM. *Computer Methods in Applied Mechanics and Engineering*, 196:1261–1277, 2007.

[92] G. Zavarise and P. Wriggers. A segment-to-segment contact strategy. *Mathematical and Computer Modeling*, 28:497–515, 1998.

[93] O.C. Zienkiewicz and A. Craig. Adaptive refinement, error estimates, multigrid solution, and hierarchic finite element method concepts. In I. Babuška, O.C. Zienkiewicz, J. Gago and E.R. de A. Olivera, editors, *Accuracy estimates and adaptive refinements in finite element computations*, pages 25–59. John Wiley & Sons, 1986.

[94] O.C. Zienkiewicz and D.V. Phillips. An automatic mesh generation scheme for plane and curved surfaces by isoparametric co-ordinates. *International Journal for Numerical Methods in Engineering*, 3:519–528, 1971.

[95] O.C. Zienkiewicz and R.L. Taylor. *The Finite Element Method – The Basis*, volume 1. Butterworth-Heinemann, 5th Auflage, 2000.

[96] O.C. Zienkiewicz, R.L. Taylor, S.J. Sherwin and J. Peiro. On discontinuous Galerkin methods. *International Journal for Numerical Methods in Engineering*, 58:1119–1148, 2003.